INSTITUTO POTOSINO DE INVESTIGACIÓN CIENTÍFICA Y TECNOLÓGICA, A.C.

POSGRADO EN CIENCIAS AMBIENTALES

Synthesis, purification, photoluminescence mechanisms and energy applications of biomass-derived carbon dots

Tesis que presenta

M. C. Andrea Susana González Vera

Para obtener el grado de

Doctora en Ciencias Ambientales

Codirectores de la Tesis:

Dr. José René Rangel Méndez

Dr. Luis Felipe Cházaro Ruíz

San Luis Potosí, S.L.P., septiembre 2025

Constancia de aprobación de la tesis

La tesis "**Synthesis, purification, photoluminescence mechanisms and energy applications of biomass-derived carbon dots**" presentada para obtener el Grado de Doctor(a) en Ciencias Ambientales fue elaborada por la **M. C. Andrea Susana González Vera** y aprobada el **1° de septiembre de 2025** por los suscritos, designados por el Colegio de Profesores de la División de Ciencias Ambientales del Instituto Potosino de Investigación Científica y Tecnológica, A.C.

_____
Dr. José René Rangel Méndez
Codirector de la tesis

_____
Dr. Juan Matos Lale
Miembro del Comité Tutoral

_____
Dr. Luis Felipe Cházaro Ruiz
Codirector de la tesis

_____
Dr. Carlos Antonio Pineda Arellano
Miembro del Comité Tutoral

_____
Dra. Conchi Ovin Ania
Miembro del Comité Tutoral

_____
Dr. Miguel Ángel Ruíz
Miembro del Comité Tutoral

Créditos Institucionales

Esta tesis fue elaborada en los Laboratorios de Procesos Fisicoquímicos y Análisis Instrumental de la División de Ciencias Ambientales del Instituto Potosino de Investigación Científica y Tecnológica, A.C., bajo la codirección los doctores José René Rangel Méndez y Luis Felipe Cházaro Ruíz.

Durante la realización del trabajo el autor recibió una beca académica del Consejo Nacional de Ciencia y Tecnología (CVU 821870) y del Instituto Potosino de Investigación Científica y Tecnológica, A. C.

Página en Blanco que se va a utilizar para colocar la copia del acta de examen.

Dedicatory

To my extraordinary mother, and my amazing friends and family: I could not be more grateful to have you in my life. All of you are the fuel behind all my actions.

To my father: I still miss you every single day. All my achievements are also yours.

To my beloved husband: Thanks for choosing to share this adventure (and this life) with me, for crossing the world to be together at Christmas, and for always encouraging me to keep working and follow my dreams. I am completely sure that together we can do anything, my love.

Acknowledgments

Thanks to CONAHCYT for the PhD scholarship (CVU 821870). To LAMBAMA, LINAN and IPICYT laboratories for the facilities and the technical support (M. Rocha-Medina, E. Isaacs-Paez, G. Vidriales-Escobar, H. Silva-Pereyra, M. Olvera-Sosa).

Thanks to CONACYT-Fondos Sectoriales-SENER (grant 245467), SEP CONACYT ANUIES and ECOS NORD (grants 315202, M20P01) for the funding to develop this research.

A special acknowledgment to my advisors, Dr. Luis Felipe Cházaro Ruíz and Dr. René Rangel Méndez, for their advice, patience, and guidance, for welcoming me into your research groups, and for always encouraging me to improve. I also thank my advisory committee for their guidance and for sharing their knowledge with me. Special thanks to Dra. Conchi Ania for welcoming me in France with her research group, for her time, enthusiasm, and for making me feel at home from the very first day. Thanks also to Dr. Carlos Pineda for welcoming me in Aguascalientes and for all his kind attentions. Finally, thanks to Dr. Juan Matos and Dr. César Nieto for their always accurate comments.

Contents

List of Figures

List of Tables

Resumen

La generación de puntos de carbono (CDs) a partir de biomasa es una gran oportunidad para aprovechar este tipo de residuos mediante metodologías sencillas y económicas. La estructura química y los mecanismos fotoluminiscentes de este tipo de nanopartículas aún no están completamente definidos y siguen siendo objeto de debate en la comunidad científica. Además, es esencial realizar una caracterización profunda de los CD derivados de la biomasa y sus correspondientes subproductos para tener en cuenta la influencia que los heteroátomos y los subproductos, como las fracciones de cromóforos, pueden tener en sus características ópticas y fisicoquímicas.

En este trabajo, se sintetizaron CDs mediante un proceso hidrotérmico asistido por microondas a partir de la fracción lignocelulósica de cáscara de naranja. Se caracterizó la cáscara de naranja utilizada para conocer su composición, es decir, la cantidad de extractos, lignina, holocelulosa y cenizas. Los CDs se purificaron mediante separación secuencial con membranas en el siguiente orden decreciente de diámetro poroso: 0,22 µm, 0,1 µm, 100, 50 y 5 kDa. El objetivo del proceso de purificación consiste en separar las nanopartículas de CDs de los subproductos carbonosos indefinidos.

Las suspensiones derivadas de cada etapa de purificación se caracterizaron mediante espectroscopia infrarroja (FTIR), desorción programada por temperatura acoplada a espectroscopia de masas (TPD-MS), dispersión dinámica de luz (DLS), espectroscopia UV-Vis y espectroscopia de fotoluminiscencia. La caracterización de las muestras con diferentes niveles de purificación mostró diferencias en sus características, las cuales se relacionaron con los subproductos eliminados durante cada etapa de separación. El estudio demostró que el nivel de purificación influye en el comportamiento coloidal y en la intensidad de emisión de fotoluminiscencia de las suspensiones que contienen CDs.

La fracción más purificada, obtenida de la filtración con la membrana de 5 kDa (después de 5 pasos de purificación secuencial), del material carbonoso se caracterizó también mediante microscopía electrónica de transmisión de alta resolución (HR-TEM), Raman, espectroscopia foto-electrónica de rayos X (XPS), titulación potenciométrica y resonancia magnética nuclear (RMN). Las imágenes HR-TEM mostraron nanopartículas esféricas con un tamaño promedio de 3.42 ± 0.85 nm y planos cristalográficos bien definidos con una distancia d de 0.21 nm. El potencial zeta y el pH de carga cero revelaron la presencia de grupos funcionales superficiales de tipo ácido compuestos principalmente por oxígeno y nitrógeno, lo que se corroboró posteriormente mediante otras técnicas. Además, se analizaron las tendencias de agregación de las partículas en suspensiones acuosas. Se analizó el comportamiento fotoluminiscente de la fracción más purificada para comprender mejor los procesos de transferencia de energía entre las partículas en suspensión,

influenciados por las interacciones entre partículas. Se examinaron cuidadosamente las deconvoluciones de los espectros de fotoluminiscencia en diversas condiciones.

Los CD demostraron su capacidad para sensibilizar celdas solares de tercera generación. Para lograr este objetivo, se construyeron prototipos de celdas solares con fotoánodos sensibilizados mediante recubrimiento por inmersión utilizando CDs derivados de cáscara de naranja en diferentes niveles de purificación y concentraciones. El rendimiento de las celdas solares construidas se evaluó obteniendo curvas I-V. A partir de estas curvas se obtuvo el voltaje de circuito abierto y la corriente de corto circuito. Posterior a ello, se calculó el factor de llenado y la eficiencia de las celdas solares. Los CDs derivados de residuos de biomasa demostraron ser un material fotoluminiscente con capacidad para sensibilizar las celdas solares de tercera generación. El material aumentó la eficiencia de las celdas solares de tercera generación en comparación con las celdas construidas con fotoánodos prístinos de FTO-TiO_2.

Abstract

Generation of biomass-derived Carbon Dots (CDs) is a great opportunity to take advantage of waste materials through easy and cheap methodologies. The chemical structure and photoluminescent mechanisms of this kind of nanoparticles are not completely defined yet and still are under discussion within the scientific community. Also, a deep characterization of biomass-derived CDs and their corresponding by-products is essential to consider the influence of heteroatoms and by-products, like chromophores fractions, may have on their optical and physicochemical characteristics.

In this work, CDs were synthesized by a microwave-assisted hydrothermal process from the lignocellulosic fraction of orange peel. The employed orange peel was characterized to know their composition, for instance, quantity of extractives, lignin, holocellulose and ashes. CDs were purified by sequential separation with membranes in the following decreasing order of porous diameter: 0.22 μm, 0.1 μm, 100, 50, and 5 kDa. The aim of the purification process was to separate the CDs nanoparticles from undefined carbonaceous by-products.

The suspensions derived from each purification step were characterized by FT-Infrared spectroscopy (FTIR), thermo-gravimetric and temperature-programmed desorption coupled to mass spectroscopy (TPD-MS), dynamic light scattering (DLS),

UV-Vis and photoluminescence spectroscopy. The characterization of the samples at different purification levels showed differences in their features, which were related to the by-products removed during each separation step. The study showed that the purification level influences the colloidal behavior and photoluminescence emission intensity of suspensions containing CDs.

The most purified fraction, from 5 kDa membrane (step 5), of carbonaceous material was further characterized by High Resolution-Transmission Electron Microscopy (HR-TEM), Raman, X-ray photoelectron spectroscopy (XPS), potentiometric titration, and nuclear magnetic resonance (NMR). HR-TEM images showed spherical nanoparticles with an average particle size of 3.42 ± 0.85 nm and well-defined crystallographic planes with a d-spacing of 0.21 nm. The zeta potential and pH of zero point charge revealed the presence of acidic surface functional groups mainly composed of oxygen and nitrogen, which was further corroborated by other techniques. Besides, the tendencies of particle aggregation in aqueous suspensions were analyzed. The photoluminescent behavior of the most purified fraction was analyzed to better understand the energy transfer processes among particles in suspension, influenced by interparticle interactions. Deconvolutions of photoluminescence spectra under various conditions were carefully examined.

The CDs were proved as sensitizers of third generation solar cells. To achieve this objective, prototypes of solar cells were constructed with photoanodes sensitized by dip-coating using orange peel-derived CDs at different purification levels and concentrations. The performance of the constructed solar cells was evaluated by

obtaining I–V curves. Open-circuit voltage and short-circuit current were extracted from these curves. The fill factor and efficiency of the solar cells were then calculated. Biomass waste derived CDs demonstrated to be a photoluminescent material with capacity to sensitize third generation solar cells. The material increased the efficiency of the third-generation solar cells in comparison with cells constructed with pristine FTO-TiO_2 photoanodes.

Chapter 1
Introduction

Chapter 1: Introduction

1.1. Environmental crisis

Greenhouse gases (GHG), like carbon dioxide (CO_2), nitrous oxides (NO_X) and methane (CH_4) are associated with the phenomenon of global warming. The increase of their concentration in the atmosphere leads to a rise in the average surface temperature of the Earth, threatening the conservation of vulnerable animal and plant species worldwide.

The development of industrial and transportation technology over time has led to the increased exploitation of fossil fuels, establishing them as the primary energy source throughout the 20^{th} century and continuing into the present day, which has resulted in significant GHG emissions. GHG emissions from human activities have risen dramatically since the Industrial Era, reaching exorbitant levels. In 2022, global CO_2 emissions from energy combustion and industrial processes were estimated to have reached a record of 36.8 Gt (IEA, 2023). Consequently, the temperature of the earth has risen importantly in the last years. According to historical records, the last 10

years have been, by a wide margin, the warmest years since global records began in 1850 (NOAA National Centers for Environmental Information, 2024). This situation, together with phenomena such as overpopulation, extreme consumerism, overexploitation of resources, species extinction, environmental pollution and excessive waste generation are part of the severe environmental crisis that humanity must confront.

1.1.1. Global energy demand

To adapt to the new living conditions that the planet will present, humanity must change its current lifestyle and adopt more environmentally friendly alternatives to meet its needs. This is why governments, and international organizations promote the use of so-called alternative, green or renewable energies. These alternatives can help to mitigate polluting emissions without compromising the economic activities that generate them. However, despite the availability of numerous renewable options to replace the high GHG-emissive conventional sources, only a small fraction of the energy supply of the world currently comes from renewable sources (biofuels, hydropower, wind or solar energies) and most of the energy produced to meet the world global energy demand comes from non-renewable fossil fuel-derived sources such as coal, oil, and natural gas (Figure 1).

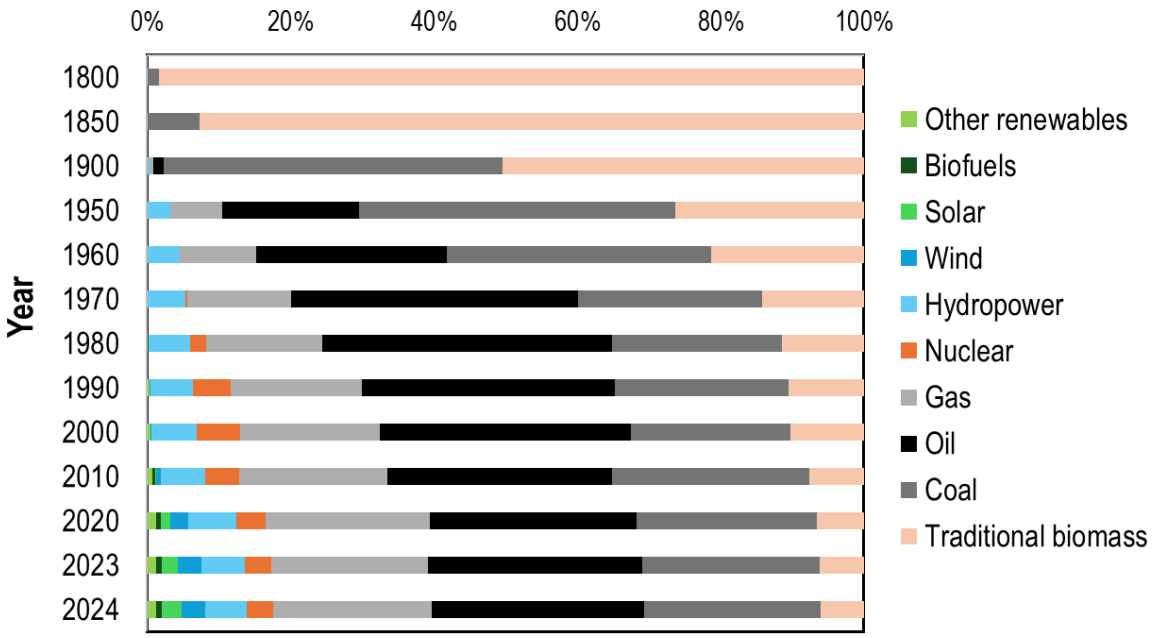

Figure 1. Percentage of the type of energy sources that satisfy the global demand of energy from 1800 to 2024 (Data obtained from (Energy Institute, 2025))

The importance of renewable energy has increased over the last 50 years. However, global energy consumption has also risen, but exponentially. Table 1 presents data on global energy consumption by source from the Industrial Revolution (1800) to 2024. In 1800, the total amount of energy consumed was around 5,653 TWh, primarily from traditional biomass. By 2024, global total energy increased to around 186,383 TWh, with oil as the dominant source (55,292 TWh). These data illustrate the dramatic increase in energy consumption in recent years and the overexploitation of fossil fuels. Renewable energy sources have not been widely adopted, partly because their efficiency and cost levels are still not competitive with those of fossil fuels.

Table 1. Global energy consumption by source expressed in terawatt-hours (Data obtained from (Energy Institute, 2025)

Year	Other renewables	Biofuels	Solar	Wind	Hydro-power	Nuclear	Gas	Oil	Coal	Traditional biomass
1800	0	0	0	0	0	0	0	0	97	5556
1850	0	0	0	0	0	0	0	0	569	7222
1900	0	0	0	0	47	0	64	181	5728	6111
1950	0	0	0	0	925	0	2092	5444	12603	7500
1960	0	0	0	0	1914	0	4472	11097	15442	8889
1970	80	14	0	0	3263	219	9615	26685	17087	9444
1980	155	33	0	0	4810	1978	14237	35569	20878	10000
1990	366	107	1	10	5996	5557	19481	37907	25929	11111
2000	578	133	3	87	7352	7169	23994	43017	27456	12500
2010	1182	679	88	902	8933	7209	31593	48193	42016	11667
2020	2152	1068	2117	3940	10763	6640	38704	49101	42316	11111
2023	2411	1319	4027	5665	10392	6677	40151	54839	45319	11111
2024	2476	1367	5151	6124	10861	6872	41278	55292	45851	11111

1.1.2. Renewable energy options

Currently, various worldwide policies encourage the use of renewable energy. Additionally, there are numerous research projects with the aim to enhance efficiency and minimize the environmental impact of renewable energy technologies (Basem et al., 2025; Nawab et al., 2023). Among the available renewable energy options, solar energy stands out for its versatility, as it can be implemented in almost any location, including remote areas with limited infrastructure (Andrade-Arias et al., 2025). Also, photovoltaic technologies have shown accelerated technological progress, which has significantly decreased their costs (Nawab et al., 2023).

Mexico has outstanding opportunity for the implementation of photovoltaic devices due to its location in the “Solar Belt.” This geographic strip has a high potential for solar energy generation due to its favorable climate, high solar radiation, and predominantly sunny weather. However, photovoltaic technology is still not widely adopted on a large scale in the country due to diverse factors like initial installation and high costs of maintenance, government disinterest, and technical barriers (Andrade-Arias et al., 2025).

1.1.3. Solar cells

The first photovoltaic device was reported in 1954 (Chapin et al., 1954). Since then, solar technology has evolved significantly due to major advancements. The different types of solar cells developed so far can be categorized into three generations. First-generation solar cells are silicon-based and typically have high manufacturing costs but offer good efficiency. Second-generation solar cells are cheaper and more flexible than the first generation but have lower efficiency. These photovoltaic devices, known as thin-film solar cells, can be composed of heavy metals such as copper, indium, gallium, selenide, cadmium telluride (CdTe), amorphous silicon, and microcrystalline silicon. Third-generation solar cells include recent and innovative photovoltaic technologies capable of achieving high efficiencies but are still under development. Examples include organic solar cells, dye-sensitized solar cells, multi-heterojunction solar cells, and quantum dot solar cells (Choubey et al., 2012). Green *et al.* (2024) compiled the highest efficiencies achieved by different solar cell types. Table 2 presents some of the highest values recorded so far along with their corresponding parameters.

Table 2. Best performance of different solar cells (Data obtained from Green et al., 2024)

Classification	Efficiency (%)	Area (cm^2)	V_{oc} (V)	J_{sc} (mA/cm^2)	Fill Factor (%)	References
Silicon Si (crystalline cell)	27.3 ± 0.4	243.1 (DA)	0.7434	42.6	86.2	(Longis, 2024)
III-V cells GaAs (Thin film cell)	29.1 ± 0.6	0.998 (AP)	1.1272	29.78	86.7	(Kayes et al., 2011)
Thin film chalcogenide CIGS (cell) (Cd-free)	23.35 ± 0.5	1043 (DA)	0.734	39.58	80.4	(Nakamura et al., 2019)
Amorphous/ Microcrystalline Si (amorphous cell)	10.2 ± 0.3	1001 (DA)	0.896	16.36	69.8	(Matsui et al., 2015)
Amorphous/ Microcrystalline Si (microcrystalline cell)	11.9 ± 0.3	1044 (DA)	0.55	29.72	75	(Sai et al., 2018)
Perovskite Perovskite (cell)	25.2 ± 0.8	1034 (DA)	1.162	26.39	82	(W. Chen et al., 2022)
Dye sensitized Dye (cell)	11.9 ± 0.4	1.005 (DA)	0.744	22.47	71.2	(Han et. al., 2009; Komiya et al., 2011)
Organic Organic (cell)	15.8 ± 0.3	1.064 (DA)	0.8513	25.11	73.9	(Faisst et al., 2023)

DA: Designated illumination area, AP: Aperture area

After more than 50 years of research, new strategies are still being explored to enhance the efficiency of solar cells while decreasing their cost and environmental

impact. In recent years, one promising approach has been the incorporation of carbon-based materials, such as graphene (C. Zhang et al., 2021), nanotubes (Mohammed et al., 2023), and carbon dots (Baytar et al., 2024; C. Li et al., 2024; X. Wang et al., 2023; Z. Wang et al., 2020; Zdražil et al., 2020) to improve solar cell performance.

1.2. Carbon based materials

Carbon is the element number 12 in the periodic table and possesses an atomic structure capable of adopting different hybridizations. Carbon can form single, double, or triple bonds, creating chain or ring structures with other carbon atoms as well as with atoms of different elements such as nitrogen, oxygen, sulfur, phosphorus, etc. These properties enable carbon to form an infinite number of molecules and structures with diverse configurations. As a result, it gives rise to a wide variety of carbon-based materials with different sizes, shapes and unique characteristics.

The study of carbon-based materials is fundamental in materials science due to the ability of carbon structures to acquire diverse chemical, mechanical, structural, thermal, porosity, and conductive properties. These materials have added value because they can be produced from renewable sources such as biomass or waste materials. Furthermore, their applications extend across various fields, including environmental and energy sectors, such as electrodes in energy devices (batteries, supercapacitors, fuel cells, solar cells), or as materials for catalysis, photocatalysis, and adsorption (Titirici et al., 2015).

Carbon-based materials with one or more dimensions decreased to the nanometric scale, have gained special attention in recent years due to their unique characteristics, which differ significantly from those of non-nanometric or bulk materials. Carbon-based nanomaterials can be classified based on their dimensions confined to the nanoscale range, i.e., less than 100 nm (Pande et al., 2024). The dimension of the material also defines the range of continuous movement of electrons.

0D carbon materials, such as carbon dots, which include carbon quantum dots, graphene quantum dots, and carbon nanodots have all their dimensions at the nanometric scale. Consequently, their electrons are constrained in all the three directions, meaning their movement is completely confined, allowing only discrete electron transitions. In contrast, for 1D, 2D or 3D materials, electron movement can be continuous along one, two or the three axes, respectively (Figure 2). Each type of material has attracted attention in different fields due to their unique and special qualities (Pande et al., 2024).

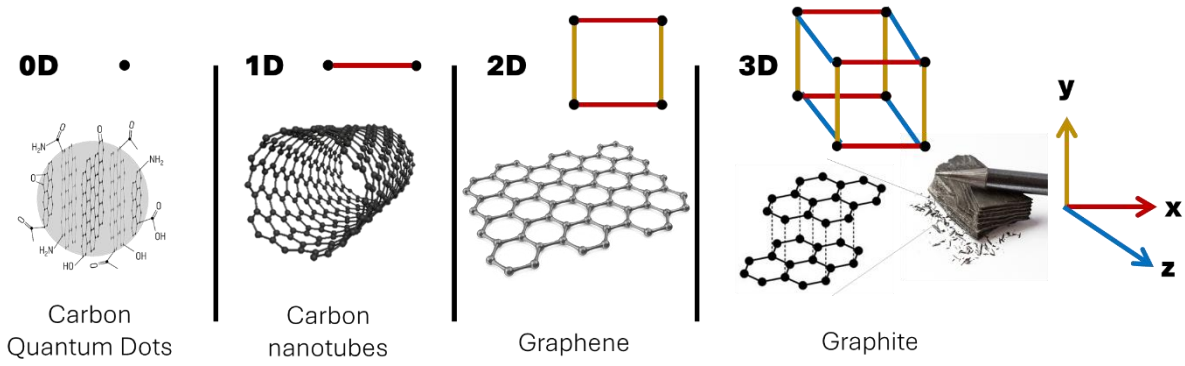

Figure 2. Examples of carbon-based materials with different dimensions of electronic movement

1.3. Classification of Carbon Dots

Carbon dots are the newest members of the carbon-based materials family. They belong to a new class of fluorescent nanomaterials that offer high photostability and low cost compared to conventional luminescent nanoparticles (M. L. Liu et al., 2019). Carbon dots were first discovered serendipitously during the purification of single-walled carbon nanotubes and were reported for the first time in 2004 by Xu *et al.* (X. Xu et al., 2004).

In general, Carbon Dots present oxygenated functional groups on their surface, which provide them with water dispersibility, biocompatibility, and low toxicity. These particles can be classified based on their nature, crystalline structure and quantum confinement effect, as follows (Cayuela Marín, 2016):

a) Carbon Nanodots (CNDs) are defined as quasi-spherical particles formed by a mixture of disordered sp^3 carbons that do not exhibit quantum confinement properties.
b) Graphene Quantum Dots (GQDs) are characterized as single π-conjugated sheets, possess well defined structures, in contrast to other types of carbon dots.
c) Carbon Quantum Dots (CQDs) are crystalline structures with spherical shapes formed by multiple stacked π-conjugated sheets combined with amorphous carbon regions. These particles display quantum confinement properties. The formation of these species depends on both the precursor and the synthesis methods.

Alternatively, other different concepts can be found in the literature to refer to this kind of luminescent carbon-based nanomaterials, for instance “carbon nanoparticles”, “carbon nanodots”, “polymer dots”, and “carbonized polymer dots” (Tao et al., 2019). Carbonized polymer dots are described as quasi-spherical nanoparticles with a core-shell structure. The core consists of a partially carbonized, cross-linked polymer network, while the shell is composed of various functional groups and polymer chains (Tao et al., 2022).

1.3.1. Differences between Semiconductor quantum dots and Carbon dots

The expression “Quantum Dot” or “Semiconductor Quantum Dots (SQDs)” is used to define semiconductor nanoparticles with sizes smaller than their Bohr exciton radius, meaning that their exciton is spatially confined with quantized energy levels

(Cayuela Marín, 2016). Physically, SQDs can be considered at the boundary between molecules and solids (Kambhampati, 2011). Common examples of Semiconductor Quantum Dots (SQDs) are Cadmium Selenide (CdSe), Gallium Arsenide (GaAs), and Lead Sulfide (PbS). These particles can be used in applications like solar cells, lasers, photon sources and light emissive diodes (LEDs) (Kambhampati, 2011)

An exciton is defined as “a quantum of electronic excitation energy traveling in the periodic structure of a crystal” (W. Y. Liang, 1970). It is electrically neutral and therefore transports energy through crystal without carrying charge. The exciton is composed of a bond electron-hole pair. Generally, SQDs behave similarly to bulk semiconductors, as both have a space between the valence band and the conduction band, known as the bandgap, and both require an energy input for exciton formation. The difference between them is that, while bulk semiconductors have a continuous energy spectrum, SQDs exhibit a quantized spectrum with multiple excitonic states, vibronic progressions, and energy bandgaps ranging from 50 to 200 meV (Kambhampati, 2011). As shown in Figure 3, the photoluminescence properties of SQDs are associated with the electronic relaxation process of the exciton. As a consequence, in the case of SQDs, the size of the nanoparticle strongly affects the exhibited photoluminescence emission.

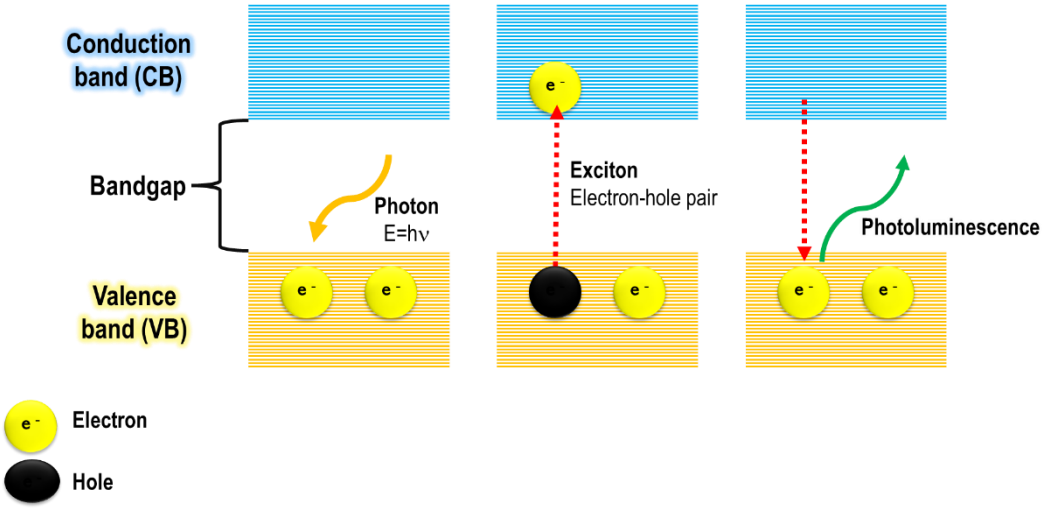

Figure 3. Exciton relaxation dynamics and photoluminescence generation

The photoluminescence properties of SQDs are mainly dominated by the quantum confinement and exhibit emission independent of the wavelength excitation and a narrow emissive full width at half-maximum (FWHM). Their photoluminescence lifetime reaches up to 10−100 ns. In contrast, the origin of the photoluminescence of carbon dots is complex, and several factors, besides quantum confinement and particle size, can influence it, as will be discussed in the following section. Carbon dots typically show excitation wavelength-dependent emission, a broad FWHM, and a lifetime of about 1-10 ns (Tao et al., 2019; S. Zhu et al., 2015).

1.3.2. Photoluminescence of Carbon dots

Carbon dots are nanometric materials that exhibit unique optical properties. Typically, their UV-vis absorption spectra exhibit a high photon harvesting in the UV region due to π-π* transitions associated with the sp^2 domains of the particle.

Additionally, absorption of light around 300–350 nm region, is associated with n-π* transitions (Figure 4) due to the presence of functional groups such as C=N, C=O, and C=S (Rasal *et al*., 2025).

Carbon dots also exhibit photoluminescence properties such as a large Stoke shift and excitation wavelength-dependent emission (Sikiru et al., 2023; Zhu et al., 2019 Vercelli et al., 2021) (Figure 4). Like SQDs, carbon dots can undergo non-radiative energy transfer mechanisms such as Förster Resonance Energy Transfer (FRET) and Dexter Electron Transfer (Rasal et al., 2025).

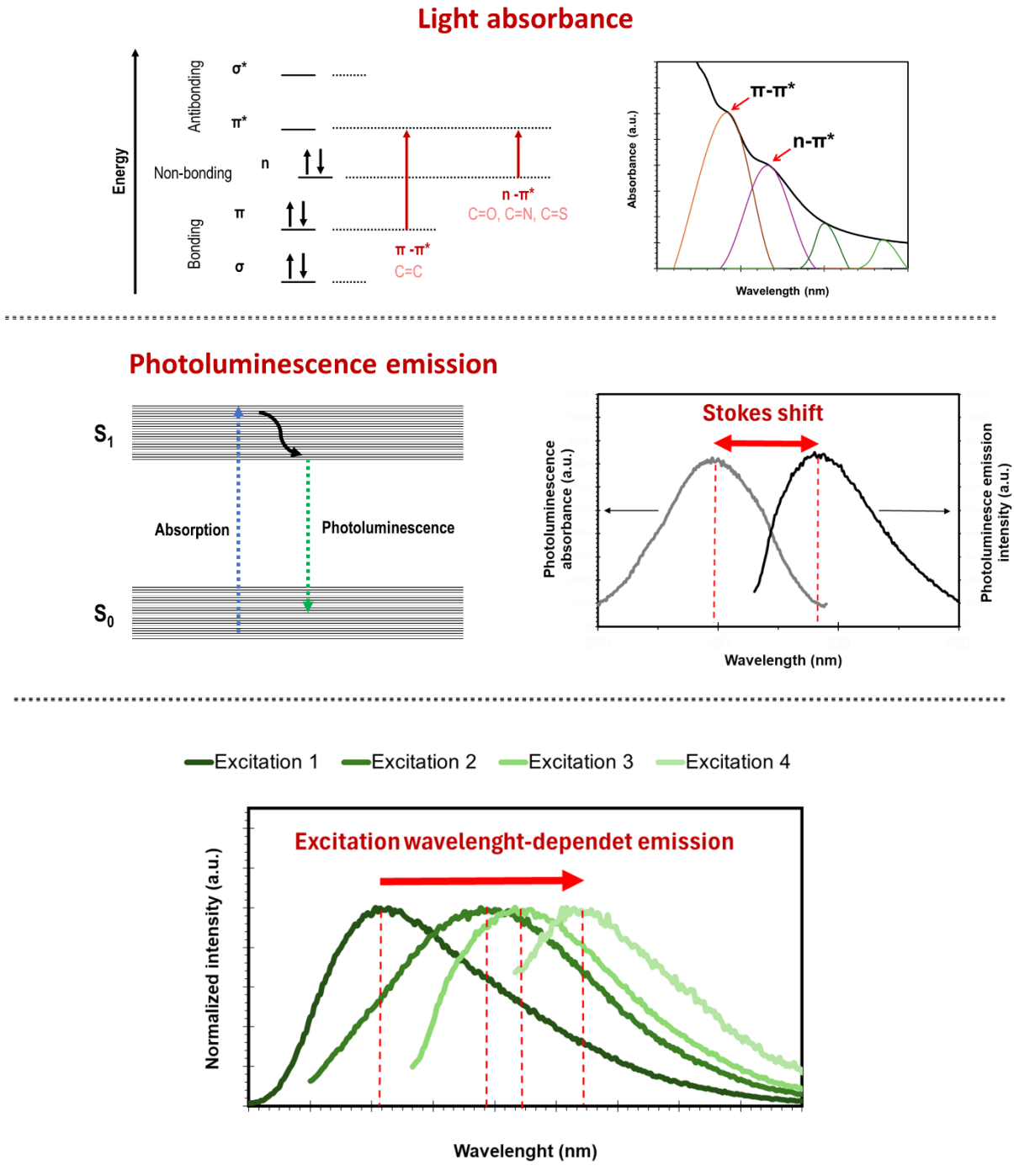

Figure 4. Scheme of the main optical processes exhibited by carbon dots; energy levels illustrating typical transitions, photoluminescence emission processes, stokes shift and excitation wavelength-dependent emission

The molecular structure of the CDs has not been precisely defined due to their complexity and non-uniform nature (Otyepka et al., 2020). Defining the chemical structure of biomass derived carbon dots is even more challenging due to the complex composition of the precursors, and rigorous purification process are required to isolate the particles.

This lack of understanding of carbon dots chemical structure hinders the clear identification of the types and quantities of functional groups or conjugated organic structures, making it difficult to determine the factors responsible for generating and enhancing their photoluminescence. Additionally, numerous factors have been found to influence photoluminescence. As a result, the intrinsic mechanisms underlying photoluminescence remain complex and controversial (Essner et al., 2018), consequently, synthesizing carbon dots with the desired fluorescence properties is still a challenge (Yan et al., 2019).

In recent years, the factors that affect the photoluminescence of carbon dots have been classified as internal and external factors (Ai *et al.*, 2021), as shown in Figure 5. The main internal factors affecting the photoluminescence of carbon dots are the size of the particles or quantum confinement effect as well as their surface states. The size of the particles could be interpreted as an indirect measurement of the sp^2 graphene domain of effective conjugation length and is directly related with the quantum confinement effect. The larger the size of conjugated π-domains, the smaller the bandgap, which determines the emission wavelength of the sample (Yan *et al.*, 2019). In other words, the decreasing of CDs size will lead to an increase of

the energy gap between the electronic states, resulting in a blue shift in the absorption and emission spectra (Rasal et al., 2025).

The surface and edge states of the particles modify the electron density of the particles and affect their optical properties. For example, the presence of electron withdrawing groups (e.g. -COOH) could absorb part of the radiation signal and decrease the photoluminescence intensity. In contrast, electron-donating groups (e.g. -OH) promote photoluminescence. Also, carbon defects like vacancies and irregular rings have been related to radiative recombination of electron-hole pairs in the carbon network and constitute emission sites. Likewise, heteroatoms, like nitrogen, sulfur, and fluorine increase the emission intensity of CDs due to the promotion of high radiative recombination yields. On the other hand, N-doped CDs show blue-shifting of the photoluminescence spectra, and S and Se-doped show red-shifting (Ai et al., 2021).

The external factors that influence the photoluminescence of carbon dots include particle-solvent interactions, suspension temperature, aggregation, particle crosslinking, and the presence of molecular states (Ai et al., 2021). The functional groups from solvents can produce different surface states and introduce new energy levels into the electronic structure of the carbon dots, each function group has different capacity to donate electrons (S=O > -NH2 > -OCO-), causing changes in the emitting color of the particles (Yan et al., 2019).

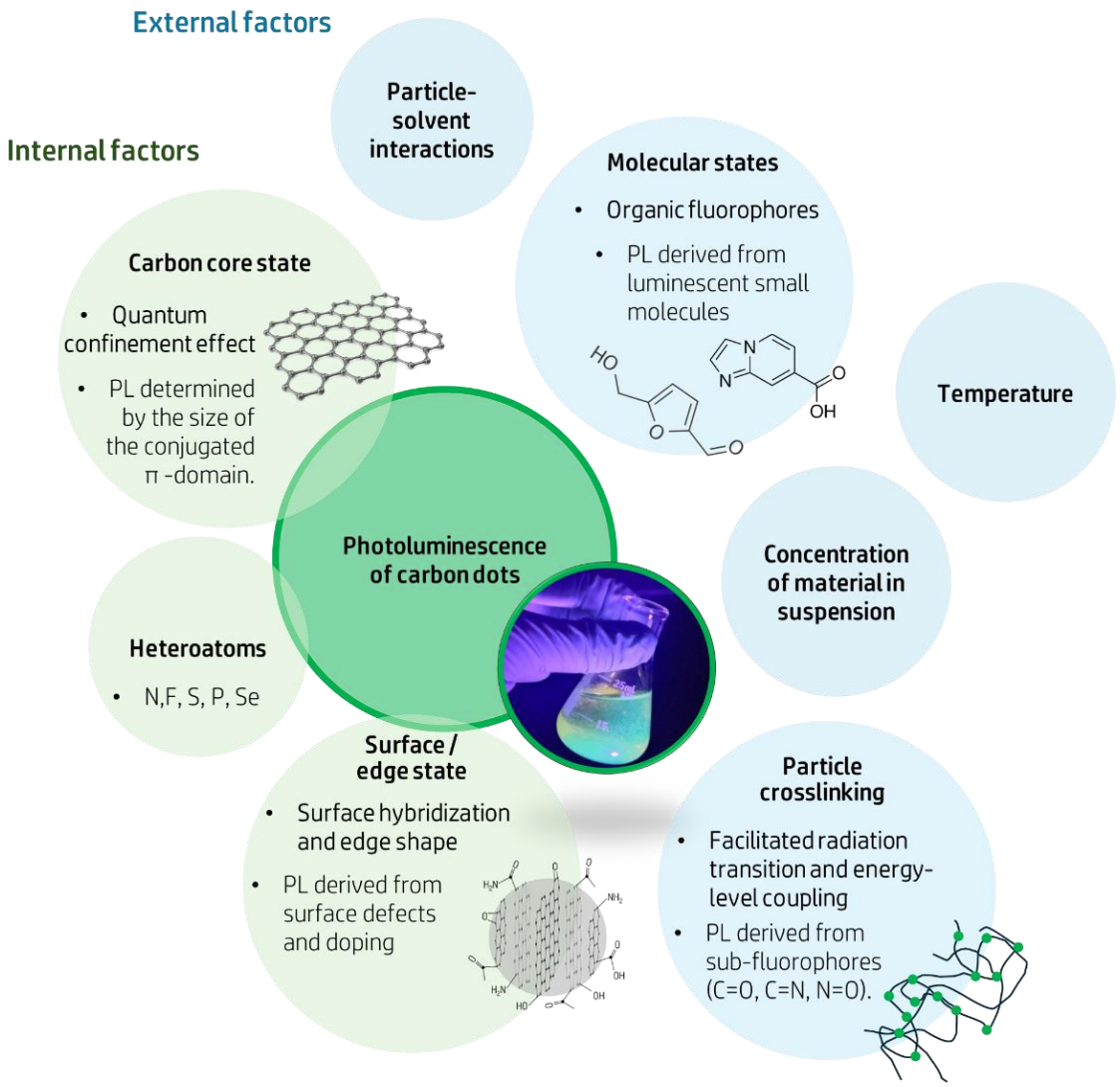

Figure 5. Factors that affect the photoluminescence of carbon dots

Crosslinking occurs due to the presence of covalent or non-covalently bonded particles, which promote supramolecular interactions. The type of bounding determines the rigidity of the aggregation, for example, a strong interaction like covalent interactions decrease vibration and rotation in systems. The decrease of the vibration and rotation modes of the covalent bonds increase the immobilization

of the particles and promote the generation of new energy levels which may change the radiation pathway resulting in an increase of the photoluminescence of the particles (Ai et al., 2021). The crosslinked structure can wrap around a fluorophore to prevent non-radiative transitions (Tao et al., 2019). Bottom-up synthesis approaches, like hydrothermal synthesis, are related with crosslinking polymerization (Ai et al., 2021; Krysmann et al., 2012). Tao *et al.* considered that as CDs formed by bottom-up processes undergo crosslinking polymerization and should be classified as carbonized polymer dots (Tao et al., 2019, 2020).

The concentration of fluorescence material in suspension could promote particle-particle interactions and affect the photoluminescence emission. Chen *et al.* synthetized carbon dots using citric acid and ethanolamine by a hydrothermal method, which shows concentration-dependent behavior. With a decrease in CDs concentration a blue shift of the emission was observed, changing from 585 to 514 nm under the fixed excitation of 420 nm (Y. Chen et al., 2018). Moreover, red shifted emission associated with increasing concentration of CDs in suspensions also have been previously reported (Gude et al., 2016). Red shifting was attributed to the aggregation of chromophore units, which induce energy stabilization of the excited state (Gude et al., 2016).

A molecular fluorophore known as IPCA (5-oxo-1,2,3,5-tetrahydroimidazo-[1,2-α]-pyridine-7-carboxylic acid) is formed during the synthesis of carbon dots from citric acid and ethylenediamine. This fluorophore exists in both anionic and neutral forms depending on the pH of the suspension, and it shows a tendency to self-assemble

into stacked structures, which interact with carbon dots via π-π stacking in water (Otyepka et al., 2020).

Previous works have shown that molecular fluorophores can be readily integrated in the structure of the carbon dots and contribute to their photoluminescent emission (Otyepka et al., 2020). These fluorophore molecules entail the presence of molecular states, which correspond to distinct energy levels that a molecule can occupy depending on the arrangement of its electrons.

The identification of molecule fluorophores as byproducts from the synthesis of carbon dots has provided evidence for the molecular state emission mechanism (Shan et al., 2023). Molecular states of fluorophores may exist independently of the carbon core and can be physiochemically adsorbed on the surface of the carbon dots or in the interior of the carbon backbone and exhibit fluorescence emission directly (Ai et al., 2021; Yan et al., 2019). The presence of molecular states along carbon dots suggests that their photoluminescence emission arises from the contribution of multiple photoluminescence centers (Balanta et al., 2023; Y. Chen et al., 2018; Pan et al., 2023; Sharma et al., 2023). At the same time, photoluminescence centers may result from the presence of molecular fluorophores in their oxidized, dimer, trimer, or tetramer forms (Zhang et al., 2017).

Various fluorescent molecules generated as by-products during the synthesis of carbon dots have been identified (Table 3). For example, Gude *et al.,* used sucrose and H_3PO_4 to generate CDs with orange-red emission (λ_{max} = 590 nm) and through several techniques identified that hydroxymethylfurfural (HMF) was the

chromophore responsible for most of the photoluminescence emission of the material. Additionally, aggregated structures of HMF can be formed through non-covalent interactions such as dipole–dipole, π–π stacking and van der Waals interactions, inducing the stabilization of the particles and provoking fluorescence along with a large Stokes shift (~150 nm). Consequently, they proposed that the aggregated chromophore unit is the fluorescing unit, rather than individual fluorophores (Gude *et al.*, 2016).

Table 3. Fluorescent molecules produced during the synthesis of fluorescent carbon dots and identified as molecular states.

Reactant	Fluorescent molecule	Ref.
CA + ethylenediamine	Imidazo[1,2-a]pyridine-7-carboxylic acid, 1,2,3,5-tetrahydro-5-oxo-, IPCA	Song *et al., 2015*
CA + cysteamine	5-oxo-2,3-dihydro-5H-[1,3]thiazolo-[3,2-a]pyridine-7-carboxylic acid	Kasprzyk *et al.*, 2015
Sucrose and H_3PO_4	hydroxymethylfurfural (HMF) derivatives	Gude *et al.*, 2016
CA + L-cysteine	5-oxo-3,5-dihydro-2H-thiazolo [3,2-a] pyridine-3,7-dicarboxylic acid (TPDCA)	Shi *et al.,* 2016
CA + cysteamine	5-oxo-3,5-dihydro-2H-thiazolo [3,2-a] pyridine-7-carboxylic acid (TPCA)	
CA + diethylenetriamine	1-(2-aminoethyl)-5-oxo-1,2,3,5-tetrahydroimidazo[1,2-a]-pyridine-7-carboxylic acid (AEIOP)	Liu *et al.,* 2017
CA + ethanolamine	2-pyridone derivatives	Das *et al.*, 2017
CA + ethylenediamine	2-pyridone derivatives	Ehrat *et al.*, 2017
CA + urea	4-hydroxy-1H-pyrrolo[3,4-c]pyridine-1,3,6(2H,5H)-trione (HPPT)	Kasprzyk *et al.*, 2018
CA + acetic acid	Methylenesuccinic acid	Khan *et al.*, 2018
o-phenylenediamine	Quinoxalino[2,3-b]phenazine-2,3- diamine (QXPDA)	Soni *et al.*, 2021
Catechol + amide	5,14-dihydroquinoxalino[2,3-b] phenazine (DHQP)	Li *et al.*, 2022

CA: Citric acid

1.4. Carbon Quantum Dots

Carbon Dots (CDs) are zero-dimensional carbon-based materials that have attracted significant research interest over the past 20 years due to their unique properties, which are listed in Figure 6. CQDs are defined as highly functionalized, quasi-

spherical nanoparticles with a diameter of less than 10 nm and a carbon core with varying degrees of crystallinity, primarily composed of sp^2 and sp^3 hybridized carbon atoms. Typically, these nanoparticles exhibit lattice spacings of 0.21 nm and 0.34 nm, which correspond to the (100) and (002) planes of the graphite lattice, respectively (Rasal et al., 2025; Sikiru et al., 2023).

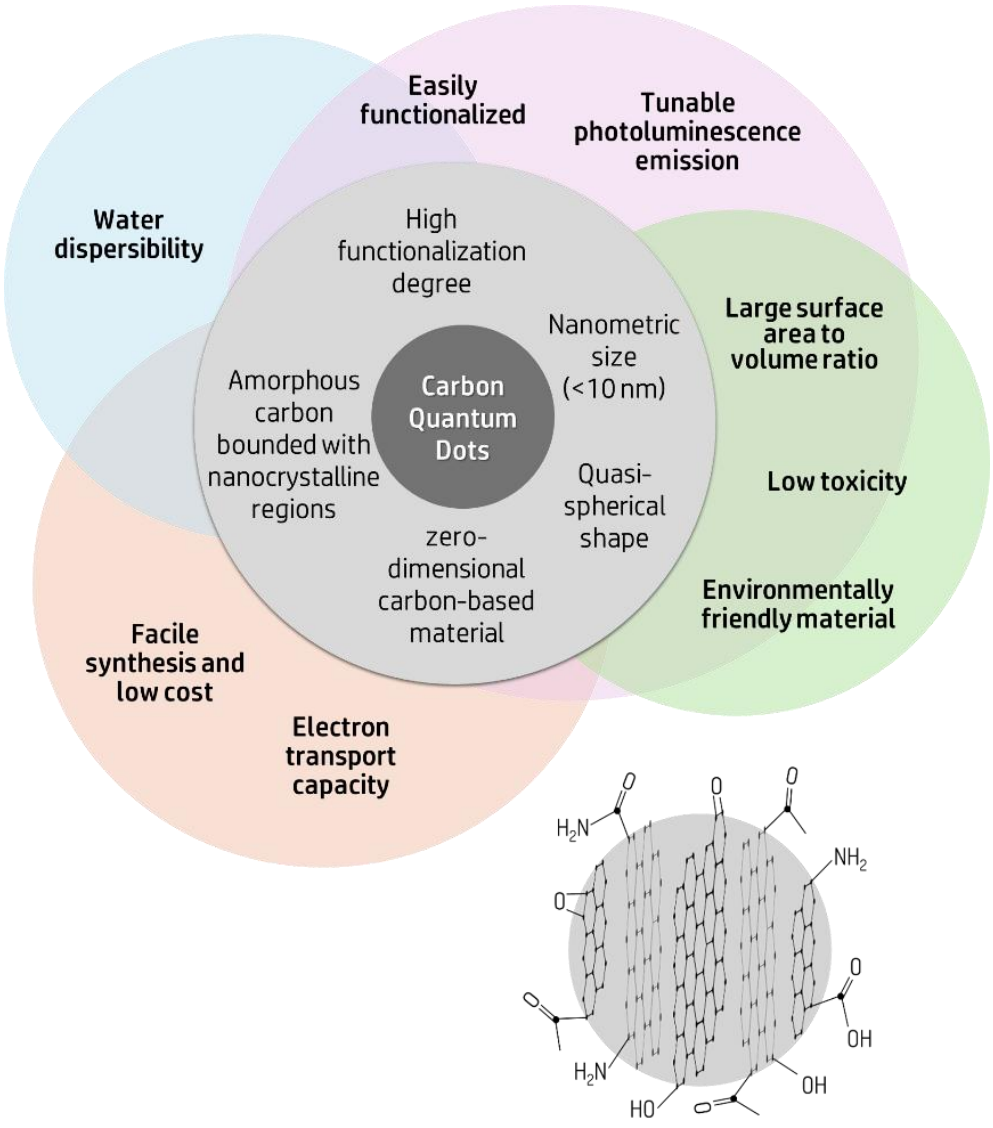

Figure 6. Molecular structure and characteristics of CDs

The nanometric size of CQDs and the presence of conjugated sp^2 domains in their molecular structure, cause optical properties associated with the quantum confinement effect and semiconductor behavior of the nanoparticles. Additionally, it has been reported that CQDs may exhibit photon up-conversion, defined as “the successive absorption of two or more low-energy photons, resulting in the emission of high-energy luminescence” (Rasal et al., 2025).

The highly functionalized structure of CQDs, which can incorporate heteroatoms like oxygenated groups (-OH, -CO, and -COOH) and nitrogen, grants them water dispersibility and makes them easy to modify chemically. The capacity to modify the chemical structure of CQDs also facilitates the tuning of their optical properties.

The composition, size, and structure of CQDs can be easily modified by adjusting specific synthesis parameters, as will be discussed in detail in the following section. These structural modifications can lead to changes in their light absorption and emission ranges. Although SQDs exhibit higher light absorption capacity and quantum yield than CQDs, they are more expensive to produce and could be toxic materials. Additionally, CQDs are remarkable photoluminescent nanoparticles due to their biocompatibility, chemical inertness, and photostability (Rasal et al., 2025).

The properties of CQDs make them highly promising materials for various applications, particularly in biomedicine and environmental fields. Many research groups have explored the use of CDs in bioimaging, drug delivery, wound healing, cancer therapy, bio-detection, environmental remediation, photocatalytic degradation, membrane desalination, adsorptive removal processes, and

fluorescent sensors (Rasal et al., 2025). However, despite the extensive research conducted to date, the application of CQDs has not yet met the expectations. This is due to several remaining challenges, such as the reproducibility of synthesis and scalability.

1.5. Synthesis of Carbon Dots

CDs nanoparticles have been obtained from different carbon sources and by different synthesis methods. The bottom-up methods utilize small organic molecules as carbon precursors. These molecules undergo harsh conditions to facilitate the formation of the nanoparticles. Alternatively, the top-down methods utilize large carbon structures such as graphene, graphite, carbon soot and carbon nanotubes, which are decreased to nanometer-sized particles (Gao et al., 2020; Mintz et al., 2019). In general, the bottom-up treatments (e.g. chemical oxidation, thermal decomposition, ultrasonic treatment, and hydrothermal synthesis) imply easier and cheaper methodologies in comparison to the top-down approaches (e.g. electrochemical oxidation, acid refluxing, plasma treatment, and laser ablation). The specific characteristics of CDs strongly depend on various synthetic parameters such as the carbon precursor, synthesis conditions, and purification processes (Y. Liu et al., 2020; Y. Lu et al., 2014).

Bottom-up approaches to produce CDs, like hydrothermal synthesis, involve submitting a carbon source to high pressure and temperature conditions. Typically, when this happens, most of the carbon source remains as a solid carbonized material, and the recovered supernatant contains just a few milligrams of CDs along

with by-products capable of being in suspension too. The generation of a considerable number of by-products after the hydrothermal process could be corroborated by the low yields of synthesis, typically lower than 10 % (Jing et al., 2019). Ill-defined carbon by-products derived from the synthesis may have uncontrolled fluorescent properties and interact with the highly functionalized CDS, generating biases on the characterization and hindering the purification process of the material.

1.6. Purification of Carbon Dots

To achieve the isolation of CDs nanoparticles, rigorous purification protocols are necessary. An inadequate purification process could impact the application performance of the material (Beiraghi & Najibi-Gehraz, 2020; Essner et al., 2018; Mishra et al., 2022; J. Zhu et al., 2021). Chromatography (Mishra et al., 2022) and liquid-liquid extraction (J. Zhu et al., 2021) have been employed for the CDs purification, however, these techniques can be time-consuming and methodologically complex due to the similarities in the physicochemical properties of the components of the mixture, and the diversity in size, defects, and surface functional groups of the CDs (Y. Liu et al., 2020). On the contrary, membrane separation processes may be a suitable option to achieve the purification of CDs with higher yields than other techniques. Membrane separation is facilitated by the stability of CDs in aqueous suspensions, enabling their separation through a size exclusion mechanism. The selection of the retention rating of the membranes is crucial for the implementation of a purification method (X. Wang et al., 2024). The

molecular weight cutoff (MWCO) is the retention rating parameter used for the ultrafiltration membrane separation processes. Its measurements are in Daltons, which are also known as atomic mass units (Crittenden et al., 2012).

In the case of CDs, it is not easy to know their exact molecular weight to choose the ideal membrane for their purification, but it is possible to calculate it indirectly by estimating their theoretical molecular structure. Sk *et al.*, performed computational studies on carbon dots nanostructures that associate particle sizes between 0.5 and 5.5 nm with molecular weights between 0.1 and 10.8 kDa (Sk et al., 2014) by counting the carbon atoms in the molecular models.

1.7. Biomass derived Carbon Dots

Bottom-up approaches could be applied for a wide variety of carbon sources, for example plants (Malavika et al., 2021; Sunitha et al., 2021; T. Xu et al., 2021; Q. Yang et al., 2018), fruits (Surendran et al., 2021), and different kinds of biomass (Boruah et al., 2020; Paul & Kurian, 2021; Perumal et al., 2021). The synthesis of CDs using biomass as carbon precursor is a promising method to exploit agro-industrial waste to obtain valuable nanomaterials.

Biomass is usually composed of a significant proportion of lignin, cellulose, organic molecules, and some inorganic elements. The conversion of lignin and cellulose into nanostructured materials has been widely studied due to their aromatic chemicals, such as phenolic moieties, which can be used as building blocks (Titirici et al., 2015), consequently, an adequate biomass to produce CDs should contain lignin, cellulose

and an adequate proportion of inorganic elements according to the desired characteristics.

The choice of biomass is an important parameter to consider during the synthesis of CDs because it will determine their structural parameters, hydrophobicity, reactivity, photoluminescent properties and other physicochemical features derived from heteroatoms presence (Q. Hu et al., 2014; Vercelli et al., 2021). Additionally, in the case of biomass derived CDs, the purification processes applied must be particularly rigorous due to the heterogeneity of the composition of the precursor, which could detonate the formation of amorphous carbon and graphitic nanostructures different than CDs, like nano-onions (Olmos-Moya et al., 2022). Methods like chromatography and liquid-liquid extraction can be particularly challenging to isolate biomass derived CDs (Thangaraj et al., 2021).

1.7.1. Orange peel derived Carbon Dots

Orange peel is mainly composed of cellulose, hemicellulose, citric acid, glucose, fructose, phenols, flavonoids, carotenoids, and minerals (Chatzimitakos et al., 2017; Miranda et al., 2009; Olmos-Moya et al., 2022) (Figure 7), which make it a good carbon source to produce CDs. The rich chemical composition of the orange peel contributes to the doping of CDs with heteroatoms like nitrogen, silicon, sulfur, phosphorus and boron, and also to the co-functionalization of the graphitic core with carboxyl and amino groups. It has been found that the disposition of groups like ketone, aldehydes, esters, and amides on the orange peel affects the first stages of condensation during the synthesis. Additionally, the formation of CDs during the self-

polymerization and carbonization stages of synthesis, which leads to the formation of nanocrystalline domains, is facilitated by the presence of minerals like phosphorus, boron, aluminum, silicon, and sulfur (Olmos-Moya et al., 2022).

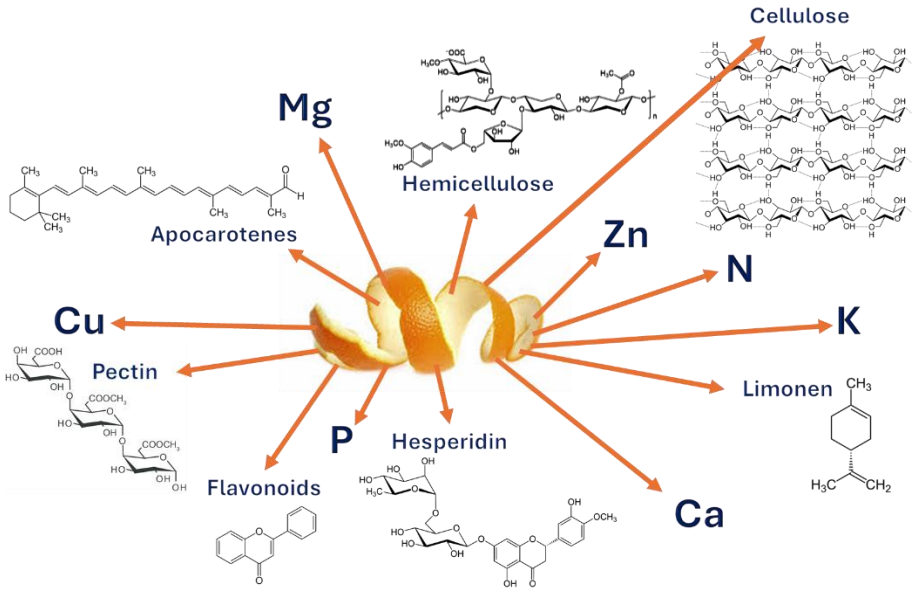

Figure 7. Orange peel composition

Wang *et al.*, (2020) reported the preparation of CDs from 14 varieties of orange peel. The resulting materials presented high quantum yields and abundant surface functionalization. Besides, it was observed that the number of volatile oils in the peel influenced the optical quantum yield of the prepared CDs (C. Wang et al., 2020).

The synthesis of orange peel derived CDs through bottom-up methods have been proposed to produce materials for fluorescence-based applications, such as, detection of Fe^{3+}, and tartrazine (Chatzimitakos et al., 2017), Cr(VI) and ascorbic acid (M. Wang et al., 2020a), Losartan-Potassium (M. Abdoon & M. Atawy, 2021), and Escherichia coli (X. Hu et al., 2021). Furthermore, CDs have been implemented

as sensitizers in solar cells (Olmos-Moya et al., 2022), and in many other applications (Acharya et al., 2024). However, the heterogeneity and natural fluctuation of the biomass composition is an obstacle for the synthesis of CDs with reproducible properties.

1.8. Carbon Dots as sensitizer of solar cells

The TiO_2 used in sensitized solar cells is characterized by its low cost, strong oxidizing ability, nontoxicity, chemical and photochemical stability, photoactivity under ultraviolet light (J. Zhang et al., 2021). Nevertheless, TiO_2 is also characterized by its wide bandgap (3.0–3.2 eV) and fast charge recombination, which difficult its energy harvesting and photocatalytic efficiency (Nguyen-Le et al., 2022). On the other hand, studies have shown that CDs can exchange electrons after photoexcitation (Langer et al., 2023), leading to electron transfer and photoluminescence emission. In this context, CDs have been used as sensitizers of semiconductor materials like titanium dioxide (TiO_2). The wide bandgap of the TiO_2 acts as a scaffold for light harvesters materials like CDs and facilitates electron collection into a current collector (Concina & Vomiero, 2015).

The addition of CDs to TiO_2 materials has shown improvements in its photocatalytic performance due to the increased visible light absorption, accelerated charge carrier transfer and decreased recombination of photogenerated electron–hole pairs (J. Zhang et al., 2021).

Moreover, CDs have been proposed as eco-friendly alternatives as light harvesters or sensitizers to increase the solar-to-electric conversion efficiencies in dye sensitized solar cells (DSSC), to replace organometal-complex dyes or rare metals which are potentially contaminants and expensive to manufacture (Gao et al., 2020; Jo et al., 2021; Olmos-Moya et al., 2022; Rangel-Mendez et al., 2018; Riaz & Park, 2022a, 2022b; Shejale et al., 2021; Y. Q. Zhang et al., 2013; Zhao et al., 2018).

The operation of a CDs sensitized solar cell is like the functioning of an electrochemical cell (Figure 8). Typically, the anode of the cell is composed of an Indium Tin Oxide (ITO) conductor glass with a layer of a semiconductor material, like TiO_2, ZnO, SnO dopped with a sensitizer material (Concina & Vomiero, 2015). The cathode is also composed of ITO covered by a thin layer of platinum. The electrolyte is composed of a redox couple capable of regenerating the electronic configuration of the sensitizer material, such as the I_3^-/I^- pair.

The generation of electric energy on a sensitized solar cell starts with the photoexcitation of the sensitizer material, in this case, CDs. The photoexcitation promotes the formation of an exciton and the corresponding transfer of an electron from the valence band to the conduction band of the CDs. A good alignment of the energy levels of the sensitizer and the semiconductor material of the photoanode will cause a transfer of electrons to the current collector. These electrons will travel to the cathode, where they will cause the reduction of the electrolytic couple. Eventually, the reduced species of the redox pair will regenerate the electronic configuration of the CDs.

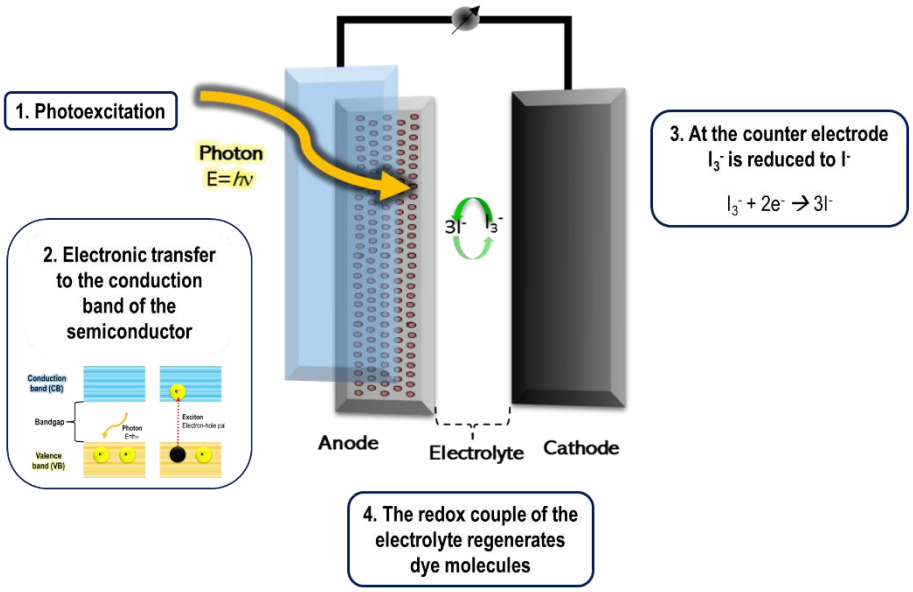

Figure 8. Schematic diagram of the operation of a CDs sensitized solar cell

The first attempt to dope solar cells with CDs was carried out using CDs synthesized via a hydrothermal method from CCl_4 and $NaNH_2$ as precursors. The CDs were evaluated on ITO electrodes with deposits of TiO_2/CD composites prepared through hydrothermal synthesis, showing efficiencies of 0.03% and 0.13% for CDs and nitrogen-doped CDs, respectively (Zhang et al., 2013). Since then, several devices have shown successful sensitization of solar cells with CDs. Until now, the highest efficiency value reported for solar cells sensitized with carbon materials is 1.01%. This efficiency was achieved by incorporating carbon nitrate nanotubes with CDs into the ITO/TiO_2 photoanode. The CDs employed were synthesized via a hydrothermal method using citric acid and ethylenediamine. In this case, the solar cell sensitized just with CDs reached an efficiency of 0.62% (Riaz & Park, 2022a). Table 4 shows the efficiency values achieved by CDs sensitized solar cells, doped

with CDs derived from different carbon sources. Even though the efficiency values of CDs-sensitized solar cells are very low compared to other types of photovoltaic devices (Table 2), it is worth continuing research on these devices as they represent a promising alternative energy source. Moreover, it has been shown that when used as co-sensitizers together with sensitizers like N719, CDs significantly increase the efficiency of solar cells (Shejale et al., 2021; Zhao et al., 2018).

Table 4. Efficiency values achieved by CDs sensitized solar cells produced from different carbon sources

Carbon source	Efficiency (%)	Reference
CCl_4	0.03	(Y. Q. Zhang et al., 2013)
Strawberry powder and ammonia	0.04	(Zhao et al., 2018)
Citric acid and urea	0.07	(Shejale et al., 2021)
Orange peel	0.18	(Olmos-Moya et al., 2022)
Citric acid and ethylenediamine	0.62	(Riaz & Park, 2022a)

1.9. Motivation for this research

Orange peel is an agro-industrial residue that is produced in large quantities all over the world. Mexico is currently the fifth-largest orange producer in the world, with an average annual production of 4.6 million tons, this means that Mexico contributes with 6% of the global orange harvest. In the other hand, the state of San Luis Potosí is the third largest orange producer in Mexico. The government of San Luis Potosí reports a total production of 368,135.54 tons in a harvested area of 31,283.07

hectares. The production is concentrated in the middle zone of the state, in the townships of Lagunillas, Rioverde and Ciudad Fernandez (Secretaría de Desarrollo Agropecuario y Recursos Hidráulicos, 2022). Due to the large volumes of waste generated, it is very attractive to use orange peel as a raw material to generate nanomaterials such as CDs. Besides, CDs could be applied as materials to increase the efficiency of CDs sensitized solar cells. The improvement of the efficiency of third generation solar cells could be useful to promote the use of renewable energy, with the aim of reducing the consumption of fossil fuels and the production of the corresponding GHG emissions.

Over the past decade, there has been an exponential increase in publications related to the synthesis and applications of biomass waste derived CDs, nevertheless, the explanation of the origin of their optical properties, physicochemical features and chemical structure are yet unclear (Essner et al., 2018; Mishra et al., 2022). Additionally, the purification process employed to isolate these kinds of particles are not yet standardized and have not been previously studied in depth.

1.10. Hypothesis

The chemical and optical properties of carbon dots will be influenced by the chemical environment in which the nanoparticles are found. Consequently, in the case of orange peel derived carbon dots, the presence of synthesis by-products will modify the optical response of CDs, affecting their performance.

1.11. General objective

To generate and characterize Carbon Dots from orange peel to gain deeper insights into the chemical structure of the nanoparticles and the origin of their optical properties.

1.11.1. Specific objectives

1. Characterize the orange peel to be used as carbon source by chemical analysis to estimate its composition.
2. Synthesize Carbon Dots from orange peels and characterize them by different techniques (FTIR, TGA, TPD-MS, UV-Vis, Photoluminescence spectroscopy, TEM, XRD, potentiometric titrations, NMR and XPS).
3. To study the influence of the presence of byproducts from synthesis on the suspensions obtained from every filtration step
4. Identify the molecules present in orange peel that contribute to the formation of CDs.
5. To estimate the photoluminescence mechanism that may occur in biomass derived CDs
6. To evaluate the effect of the presence of CDs on the performance of solar cells when CDs are used as photoanode sensitizers in Grätzel-type solar cells.

Chapter 2

Synthesis of orange peel derived Carbon Dots and sequential purification

Adapted from: Gonzalez-Vera, A. S., Pineda-Arellano, C. A., Ramírez-Monroy, A., Matos, J., Chazaro-Ruiz, L. F., Rangel-Mendez, J. R., & Ania, C. O. (2025). Influence of the sequential purification of biomass-derived carbon dots on their colloidal and optical properties. Carbon Trends, 19, 100460.

https://doi.org/10.1016/j.cartre.2025.100460

Chapter 2: Synthesis of orange peel derived Carbon Dots and sequential purification

2.1. Introduction

In this chapter, it is explored the influence of the precursor composition and the purification of CDs from orange peel wastes, a residue that is produced in large quantities in Mexico. A sequential membrane separation process is proposed to gradually remove aggregated impurities and large oligomeric or polymeric byproducts which are formed during the CDs synthesis. The suspension obtained from the microwave-assisted hydrothermal process of orange peels was passed through membranes of different pore diameters, in the following order of retention rates: 0.22, 0.1 μm, 100, 50, and 5 kDa. The las fraction with CDs was the most purified. This process of separation was proposed because it is reported that the orange peel-derived CDs have presented high quantum yields and have been used in different applications (Chatzimitakos et al., 2017; Gudimella et al., 2021; X. Hu et al., 2021; Olmos-Moya et al., 2022; Prasannan & Imae, 2013; Tiong et al., 2015; M.

Wang et al., 2020b). However, their molecular structure and the origin of their photoluminescence emission has been studied little. That´s why the suspensions obtained at each step of the purification were analyzed to obtain information of the chemical structure of the biomass-derived CDs and the contribution of the remaining biomass by-products in suspension. In particular, the influence of the byproducts on the agglomeration tendencies and photoluminescence emission of CDs were studied.

2.2. Materials and methods

2.2.1. Orange peel obtention and characterization

Oranges (*citrus sinensis)* were collected from a local market in the city of San Luis Potosi, Mexico. To avoid modifications in the composition, origin of the fruit or maturation stage, only oranges from one lot of Citrus sinensis species were considered for this study. The peel was carefully removed from the fruit, cut into small pieces, sun dried, and pulverized. The as-obtained orange powders were suspended in 1 M HCl solution and stirred for 24 hours. After this time, the liquid was filtered out and the powder was rinsed with deionized water until constant pH (ca. 4), and then dried.

The orange peel was characterized before and after the acid wash by Inductively Coupled Plasma-Optical Emission Spectroscopy (ICP-EOS) with a 738 Varian analyzer, by elemental analyses in a COSTECH analyzer, and through the analytical procedure NREL-TP-510-42618 for the determination of carbohydrates and lignin

(Hames et al., 2008; Sluiter et al., 2008). Fourier Transformed-Infrared Spectroscopy (FTIR) spectra were obtained with an ISASA-FTIR spectrometer at Attenuated total reflectance (ATR) mode.

2.2.2. Synthesis of Carbon Dots

The CDs were synthesized through a microwave-assisted hydrothermal method, which was previous optimized by our research group (Olmos-Moya et al., 2022). 100 mg of the acid-washed orange peel powder were suspended in 15 mL of deionized water and placed in a microwave oven (Nanowave 400 Anton Paar GmbH, maximum power 700 W) at 220 °C for 30 minutes, under stirring at 1000 rpm. After the heat treatment, the supernatant generated is recovered by decantation, and the remaining carbonized orange peel is discarded.

2.2.3. Purification: Sequential membrane separation

The aqueous suspension recovered from the microwave digestion of the biomass precursor was sequentially separated using membranes of different cut-offs. Details of the membranes and the sequential order in the filtration are as follows: (step 1) mixed-cellulose esters membrane with a pore size of 0.22 μm; (step 2) PVDF Durapore membrane with a pore size of 0.1 μm; (step 3) Spectrum MicroKros TC Hollow Fiber Filters with modified poly(ether-sulfone) membranes with a molecular weight cut-off of 100 kDa, (step 4) 50 KDa and (step 5) 5 kDa. The employed membranes were continuously washed to avoid the blocking of the pores.

The obtained filtrates were freeze-dried to obtain the final CDs-containing powder. The solids were labeled according to the last membrane used in the sequential filtration (e.g., 1:0.22 μm for step 1; 2:0.1 μm for steps 1+ 2; 3:100 kDa for steps 1+2+3; 4:50 kDa for steps 1+2+3+4 and 5:5 kDa for steps 1+2+3+4+5). As an example, samples 4:50 kDa was obtained after 4 sequential filtration steps with membranes of 0.22.

The recovered solids after lyophilization were re-dispersed in deionized water for further characterization.

2.2.4. Structural and composition characterization

The Fourier Transformed-Infrared Spectroscopy (FTIR) spectra were obtained with an ISASA-FTIR spectrometer, for this analysis the materials were dried and measured at Attenuated total reflectance (ATR) mode. The Raman spectrum of the CDs from the most purified suspensions deposited in a glass and were recorded in ambient conditions using an InVia Microraman Renishaw Spectrometer with a wavelength laser of 532 nm. The spectra were collected under a optical microscope with a x20 long working distance objective. Each spectrum was recorded with an integration time of 10 s; data presented represents the average of three measurements.

Thermogravimetric analyses of the samples were carried out in a thermobalance (Netzsch-STA 409 CD) coupled to a mass spectrometer. Briefly, ca. 10 mg of the sample was heated under an argon atmosphere up to 1000 ºC (heating rate of 10

ºC min^{-1}) and the composition of the evolved gases was analyzed in the mass spectrometer.

The average hydrodynamic diameter size of the materials was determined by electrophoresis by a NANOTRAC WAVE II equipment at room temperature. Aqueous suspensions of the materials at different pH values were measured. The pH was adjusted with 0.1 M NaOH solution.

Hydrodynamic radius of the material at different conditions were obtained by the Stokes−Einstein relation using the equation:

$$R_H = \frac{K_B T}{6\pi\eta D}$$

Where, K_B is the Boltzmann constant, T is the absolute temperature of the sample, D is the diffusion coefficient, and η the viscosity of the solvent.

Potentiometric titrations were performed with a Mettler Toledo-Titration Excellence T70, in nitrogen atmosphere using 0.05 mg of the carbonaceous powder suspended in 20 mL of 0.1 M NaCl solution and stirred overnight. Then, the suspension was adjusted to pH 10 with 0.1 M NaOH solution and titrated with 0.1 M HCl solution at a pH range from 10 to 4. The corresponding proton binding curves and pKa distribution plot were calculated by using the software SAEIUS-pK-Dist (Bandosz et al., 1993; Jagiellot, 1994). The high-resolution transmission electron microscopy (HR-TEM) analyses were performed with a JEOL- 200 CX microscope at 80 KV. Nuclear magnetic resonance (NMR) spectra of the aqueous suspension were

measured on a Bruker Avance III 500 MHz equipment for ^{1}H (500 MHz) and ^{13}C (125 MHz) nuclei in deuterium oxide (D_2O, 99.8%).

2.2.5. Optical Characterization of the CDs aqueous suspensions

The aqueous suspensions obtained after each filtration step were characterized by UV-Vis spectroscopy in an Aquamate Thermo Spectronic spectrophotometer. Also, Photoluminescence emission spectra of the aqueous suspensions were measured in a Horiba Jobin Yvon IHR320MST2 spectrometer, using 375 nm as excitation wavelength. This characterization was easily obtained due to the capacity of the particles to be stable in aqueous suspension. This affinity to water is related to the high functionalization degree of the CDs with polar groups.

2.3. Results and discussion

2.3.1. Orange peel characterization

The characterization of the composition of the carbon source of biomass derived CDs is very important to understand the chemical structure of the CDs. Figure 9 shows the processes of collecting, drying, and milling the orange peels that was used as carbon source to generate CDs. Before the synthesis, the peel was washed with 1 M HCl solution with the aim of remove soluble organic molecules, decrease the ashes in the base material, and conserve only the structural compounds like lignin and cellulose. All this to decrease the complexity of the synthesis processes.

Figure 9. Process of collecting orange, dry, milled and acid wash of the orange peel

The results of the characterization of the structural components of the orange peel before and after acid washing are plotted in Figure 10. The analysis demonstrated that the acid wash removed extractive compounds from the sample, which originally were 45±2 % of the peel, additionally, the percentage of ash in the sample decreased from 7.56±0.05 to 0.66±0.04 %. The components not considered in this analysis and the percentage of soluble acid lignin remained practically unchanged before and after washing.

The decrease of the amount of ashes and extractives caused that the percentage of holocellulose and insoluble acid lignin increase around three times in the orange peel after washing, going from 20±2 to 59.9±0.05 % for holocellulose and from 4.95±0.06 to 14.8±0.2 %, for insoluble acid lignin, as also can be seen in Table 5.

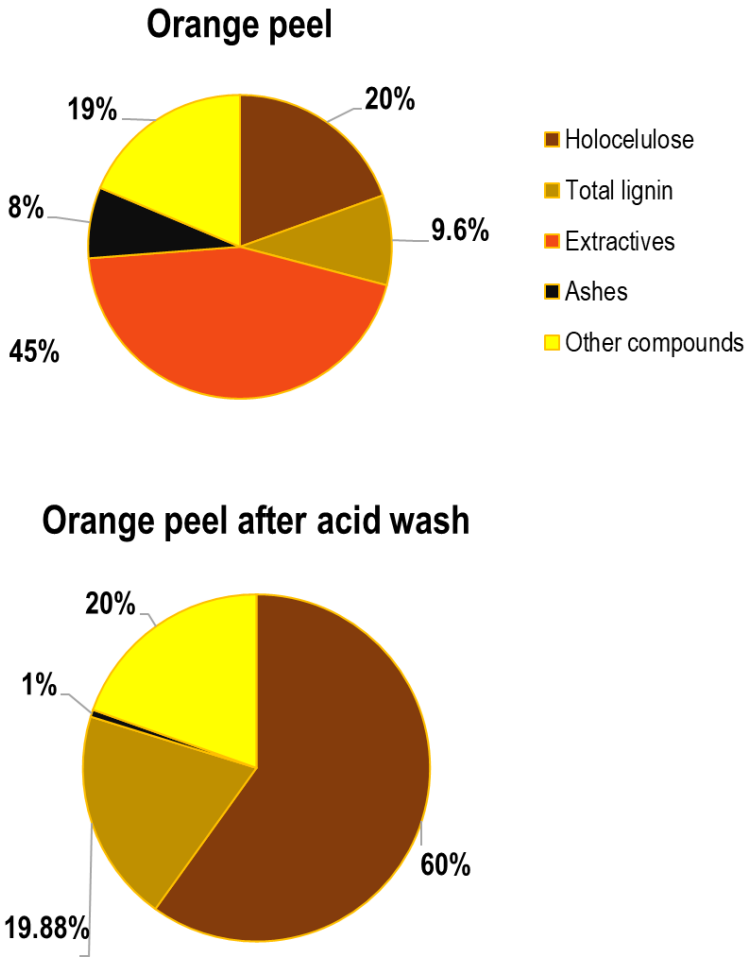

Figure 10. Structural composition of orange peel before and after acid wash

Table 5. Composition of the orange peel used as precursor for the synthesis of CDs, before and after the acid wash

		Orange peel	**Orange peel after acid wash**
Structural carbohydrates and lignin (%)	Holocellulose	20 ± 2	59.90 ± 0.05
	Total lignin	9.6 ± 0.4	19.9 ± 0.1
	Extractives	45 ± 2	ND
	Ashes	7.56 ± 0.05	0.66 ± 0.04
Elemental composition (%)	C	36 ± 7	38 ± 10
	H	5 ± 4	12 ± 1
	N	1.3 ± 0.7	2 ± 1
	O*	57 ± 5	49 ± 11
Inorganic elements (mg/g of peel)	Ca	67 ± 23	17± 7
	K	56 ± 16	2 ± 1
	Mg	9 ± 6	2 ± 2
	Na	4 ± 5	6 ± 5
	P	2 ± 1	2.0 ± 0.4
	S	10.1 ± 0.2	4.5 ± 0.2

The change in the composition of the orange peel was also demonstrated through analysis by FTIR spectroscopy. These analyses resulted in spectra with important differences, as is shown in the Figure 11. The orange peel spectrum shows a strong

broad band around 3300 cm^{-1}, which indicates the presence of alcohol and phenol functional groups which are reported as the main components of the orange peel elsewhere (Miranda et al., 2009). The small and broad band around 2910 cm^{-1} indicated the C-H stretching of CH, CH_2 or CH_3 groups, as well, the band at 1360 cm^{-1} was related to the symmetric angular deformation of C-H bonds. The bands at 1600 and 1730 cm^{-1} denote the presence of carbonyl groups. The small bands at 1730, 1270 and 1440 cm^{-1} could be related to the presence of carboxylic acids. The strong band centered at 1010 cm^{-1} could be an overlapping of vibrations of C-O and C-O-C of polysaccharide chains and vibrations related to the presence of sulfoxides. The presence of sulfur in the orange peel was corroborated through ICP-EOS, as shown in the Table 5. The band centered at 1315 together with the band at 1010 cm^{-1} could be associated with the symmetric and antisymmetric stretching of ester groups. The FTIR spectrum of the orange peel after the acid wash shows a flat line. As it can be seen in Figure 9, the orange peel after the acid wash turned darker than the orange peel without treatment, which may exceed the limits of the technique. In addition, it is expected that the acid treatment decreases the number of molecules with functional groups detectable by FTIR, like ester, hydroxyl, and carbonyl groups. Consequently, it is congruent not to obtain strong or revealing signals from the orange peel after acid wash.

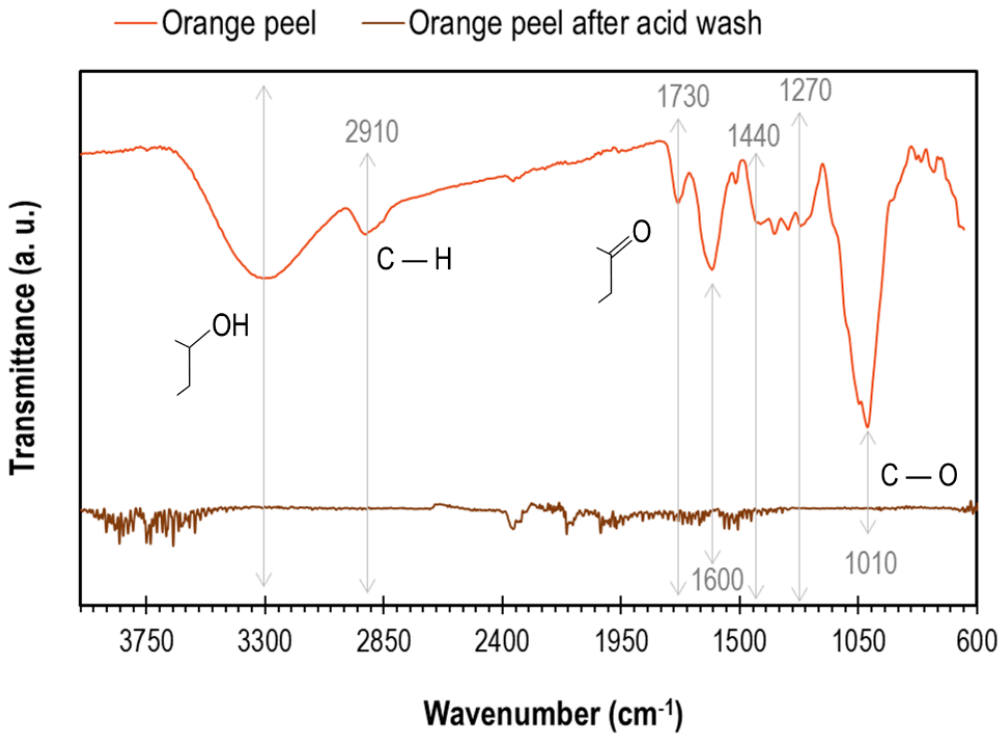

Figure 11. Fourier Transformed-Infrared spectra of the orange peel before and after the acid wash

Based on the characterization of the orange peel and previous studies (Olmos-Moya et al., 2022), an acid treatment of the biomass waste precursor was carried out to decrease the large inorganic fraction (ashes) in the pristine biomass (Ca, K, Mg, Na, P, and S; see Table 5), that otherwise would be solubilized during the microwave digestion and accumulated in the solid fraction containing the CDs after the freeze-drying, thus constituting a large fraction of inorganic impurities.

The elemental composition of the orange peel before and after the acid wash was obtained by ICP-EOS and listed in Table 5. The main inorganic elements present in

the peel, listed in order of abundance, are Calcium (Ca), Potassium (K), Magnesium (Mg), Sodium (Na), Phosphorus (P), and Sulfur (S). The change in the quantity of the detected elements per gram of orange peel notably decreased after acid washing. The decreasing of inorganic elements in the composition of the peel is also supported by the decrease in the estimated percentage of ashes before and after washing. After the acidic wash the order of abundance of the elements was Ca, Na, S, Mg, K and P. Ca concentration decreased from 67±23 to 17±7 milligrams per gram of peel, and K, from 56±16 to 2±1 milligrams per gram. Only in the case of P, the same quantity of milligrams of element per gram or orange peel remains after washing.

Acid washing also slightly increases the proportion of carbon, hydrogen, and nitrogen in the peel, while decreasing the proportion of oxygen. This is consistent with the FTIR analysis, in which the bands associated with oxygenated functional groups disappeared after treatment with HCl solution.

The presence and concentration of inorganic elements could influence the optical properties of the orange peel derived CDs, for instance, Ding *et al.* (2014) reported an increase in the quantum yield of carbon dots dopped simultaneously with sulfur and nitrogen in comparison with sulfur and nitrogen doped carbon dots, due to a synergistic effect (Ding et al., 2014). The synergistic effect between S and N is supported by previous computational simulations of a graphene networks dopped by N, S and S and N simultaneously incorporated, the calculations were performed by density functional theory and showed a redistribution of the spin and charge density

related with the presence of the N and S doping, which also generated an increase of the number of carbon atom active sites (J. Liang et al., 2012).

Furthermore, it has been shown that the doping of CDs with phosphorus decreases the interplanar distance in P-CDs, which modifies the band gap levels and generates numerous new emissive sites, increasing the quantum yield and the electrochemiluminescence intensity of the CDs (Venkateswara Raju et al., 2020). In addition, the doping of N-Ca-CDs with phosphorus has shown an enhancing of the photoluminescence intensity. The increasing intensity was associated with the generation of defect states (Sharma et al., 2023).

2.3.2. Choice of Membranes

The orange peel after acid wash is suspended in deionized water and subjected to a microwave assisted hydrothermal treatment. Following a bottom-up approach, the effect of temperature and pressure initiates the decomposition of the compounds of the peel into simpler molecules. This process subsequently triggers the formation of CDs. The suspension that results from the synthesis is filtered to avoid the presence of any by-products that might have formed during the synthesis process.

The aqueous suspensions recovered from the synthesis were sequentially separated as described in the methodology section. The membranes with cut-offs between 0.22 µm and 5 kDa, covering microfiltration and ultrafiltration, were used to separate the carbon structures of nanometric dimensions from the suspensions. As seen in Figure 1, the first two membranes with a cut-off of 0.22 and 0.1 µm

(microfiltration) allowed to reject suspended aggregates between 220 and 100 nm, like big particles of carbonized orange peel, pigments and fragments from the decomposition of cellulose. These membranes are a popular choice in the purification of CDs (Chatzimitakos et al., 2017; Das et al., 2022; Devi et al., 2023; Ganesan et al., 2022; G. Yang et al., 2016), despite this cover a fairly large range of dimensions, out of the nanometric dimensions searched for carbon dot materials.

Further sequential separation was carried out with ultrafiltration membranes of 100, 50 and 5 kDa cut-offs, which were selected according to the size range of CDs (Essner et al., 2018; Q. Hu et al., 2014; Sk et al., 2014; Spectrum Labs, 2012). A literature review was conducted to estimate the relationship between the size of the CDs (nm) and the membrane cut-offs (kDa). In Figure 12, the size range of multiple CDs synthesis reports is represented. A maximum theoretical particle size of 10 nm would correspond to molecular weights below 100 kDa, in addition, Essner *et al.* reported a correlation between the molecular weight and the size of colloidal fluorescent carbon dots, estimating that particles with 3-8 nm diameter size would correspond to a molecular weight between 15 and 40 kDa. On the other hand, Hu *et al.* reported particles of 1.4 ± 0.2 and 3.3 ± 0.5 nm associated with molecular weights of 2.4 and 7.7 kDa, respectively. Also, computational studies on carbon dots nanostructures have associated particle sizes between 0.5 and 5.5 nm with molecular weights between 0.1 and 10.8 kDa, corresponding to CxHy structures with x between 8-862 and y between 6-480 atoms (Sk et al., 2014).

The sequential separation carried out in this work with 100 kDa (step 3), 50 kDa (step 4) and 5 kDa (step 5) membranes would not only ensure the removal of large carbonaceous aggregates, but also of many aromatic compounds that could be formed during the decomposition of the biomass precursor such as lignin, cellulose/hemicellulose derivatives, polysaccharides, polyphenols, carbohydrates, etc. (Harding et al., 1991; Kraemer, 1938; Miranda et al., 2009; Sawalha et al., 2009; Spectrum Labs, 2012; Wypych, 2023; Xie et al., 2023; Zioga et al., 2022). Additionally, the removal of compounds such as lignin, flavonoids and bio-oil from the precursor during the acid wash of the orange peel will ensure that these compounds or their by-products will not be present together with the CDs in the suspension resulting from the synthesis.

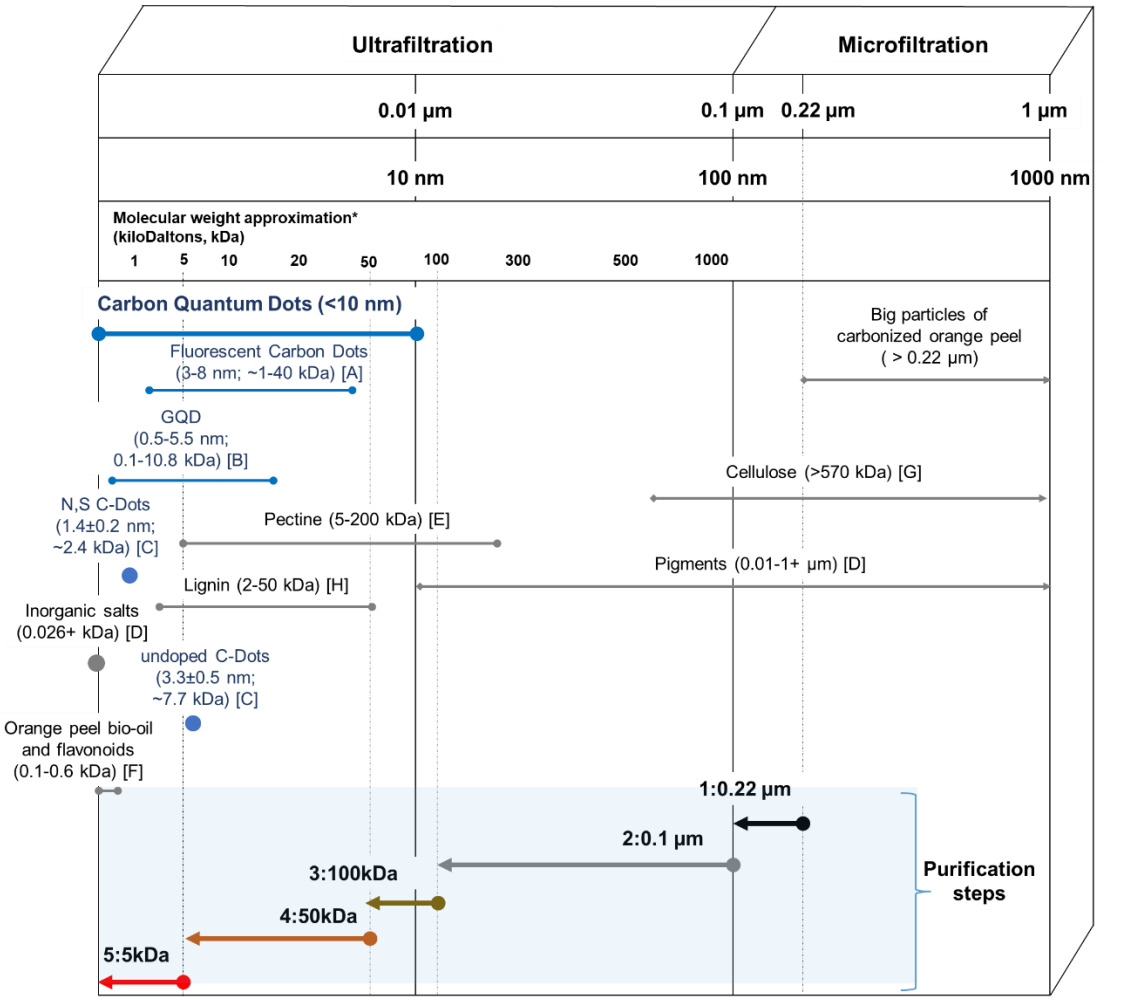

*There is not a direct correlation between a 2-dimensional metric length (nm) and a 3-dimensional molecular size (kDa)

[A] Essner *et al.*, 2018 [B] Sk *et al.,* 2014 [C] Hu *et al.,* 2014 [D] Spectrum Labs, 2012 [E] Zioga et al., 2022; Harding et al., 1991 [F] Miranda *et al.,* 2009; Sawalha *et al.*, 2009; Xie *et al.*, 2023 [G] Kraemer, 1938 [H] Wypych A., 2023

Figure 12. Estimative correlation between the average particle size of carbon dots and the cut-off of different membranes used in the sequential separation: 0.1 and 0.22 µm, 100, 50 and 5 kDa. Molecular weights of relevant compounds formed in the degradation of biomass precursors are also included for comparison.

2.3.3. Synthesis yield

The yield of the synthesized material after the different filtration steps was calculated based on the estimated concentration of total solids in the aqueous suspension obtained upon the microwave digestion of the orange peels. The estimation was carried out from the measurements of absorbance in re-suspended dispersion and the linear correlations of the experimental points. It is interesting to observe that the total solid yield obtained from the carbon precursor subjected to the acid treatment (60 ± 36 %), was larger than that of the untreated biomass (16 ± 6 %). This suggests that the lignocellulosic fraction of the orange peel was the main source of carbon for the synthesis of CDs, which was consistent with the amount of these components in the biomass before (~29.2%) and after the acidic treatment (~79.7%). On the other hand, the yield of solids in suspension at each purification step did not change significantly with the number of membranes employed, which indicates that the synthesis method does not favor the formation of particles bigger than 10 nm that could be removed upon the first two steps of the sequential separation. Although the accuracy of the estimated solids yields through absorbance measurements was not high, the thermogravimetric analysis, which will be further discussed, rendered slight differences between the samples.

Previous works reporting the purification of CDs with membranes have shown synthesis yields of up to 66.7%, employing as carbon source Sodium lignosulphonate (L. Li et al., 2017). Nevertheless, in that case the precursor is a purified commercial reactive, and the purification protocol, consisting of filtration

using Millipore 0.1 mm filter paper and a dialysis membrane with a molecular cut-off of 1000 Da for 3 days in order to remove salts and low molecular weight products, may not be rigorous enough, as we will see in the following discussion.

Table 6 shows that the obtained suspended solids in aqueous solution from the orange peel without acid washing presented a high conductivity compared to the powder from the acid washed orange peel. The changes observed are attributed to the removal of the inorganic impurities during the acid wash. In the case of the suspensions of of fractions from the different purification steps, the pH remained around 3.5 but the values of the ionic conductivity slightly decreased as the purification steps increased. This could be related to the loss of inorganic salts during the purification process

Table 6. The amount of recovered solid, pH and ionic conductivity of the aqueous suspensions obtained from each sequential filtration step.

Pretreatment of the orange peel	**Purification step**	**Average estimated amount of recovered material [%] ***	**pH**	**Ionic conductivity [µS cm^{-1}]**
without acid washing	1: 0.22 µm	16 ± 6	3.5	661
Acid washing	1: 0.22 µm	60 ± 36	3.3	301
	2: 0.1 µm	25 ± 8	3.4	301
	3: 100 kDa	16 ± 6	3.4	298
	4: 50 kDa	48 ± 12	3.5	276
	5: 5 kDa	36 ± 24	3.9	275

* Estimated from absorbance measurements

2.3.4. Characterization of fractions from the sequential filtration

The carbonaceous material obtained at each step of the subsequential purification of the CDs was recovered by lyophilization, and characterized by FTIR spectroscopy, thermo-gravimetric and temperature programmed desorption coupled to mass spectrometry, dynamic light scattering, UV-vis and photoluminescence spectrophotometry. Through these analyses it was possible to observe differences between each fraction.

2.3.4.1. FT-Infrared spectroscopy

There is a relation between the nature of the functional groups on the surface of the CDs and the starting materials (Kumar et al., 2022). Consequently, in accordance with the composition of the peel employed as initial biomass, the functional groups on the particle surface may include oxygen, sulfur, or amino-based functionalities.

Figure 13 shows the FTIR spectra of the powders obtained from each sequential separation step at the range of 4000-500 cm^{-1}. All the samples displayed a broad band centered at 3300 cm^{-1} attributed to humidity of the environment and overlapped O-H stretching vibrations, along with two small and broad bands centered at 2930, and 2880 cm^{-1} related with stretching vibrations of sp^2 and sp^3 C-H. In the range from 2000 to 1490 cm^{-1} (Figure 13), which is associated to vibrations of the carbonyl group and aromatic compounds, many overlapped small bands are found which indicates the presence of different functional groups in the particles. The band at 1725 cm^{-1} is associated with carboxylic acids, and the one around 1650 cm^{-1} could be related to

stretching of N-H bonds, N-CO in amides and/or carbonyl groups from aldehydes or ketones. This is consistent with the presence of a small amount of nitrogen in the precursor. The band around 1160 cm^{-1}, which was more notorious for samples 3:100 kDa and 4:50 kDa, is assigned to the symmetrical and asymmetrical stretching of the C-O bonds. The band at 1020 cm^{-1} suggests the presence of primary alcohols and also could be associated with the presence of sulfoxides, due to the presence of a small amount of sulfur in the bio-precursor (4.5 ± 0.2 mg g^{-1} of peel). The band centered around 1513 cm^{-1} is associated with aromatic carbon structures. Gradual spectral smoothing can be observed as purification progresses.

FTIR spectra revealed the presence of oxygen-containing functional groups as the most abundant moieties, which agrees with the high amount of oxygen in the precursor (ca. 38 ± 10 wt.%). The presence of carbonyl groups and aromatic compounds is more perceptible in the spectrum of the material at purification step 1 in comparison with the subsequent samples, which may indicate a decrease in the heterogeneity of the chemical surface composition of the carbonaceous material. A deeper discussion of the most purified material will be supported by other techniques in further sections.

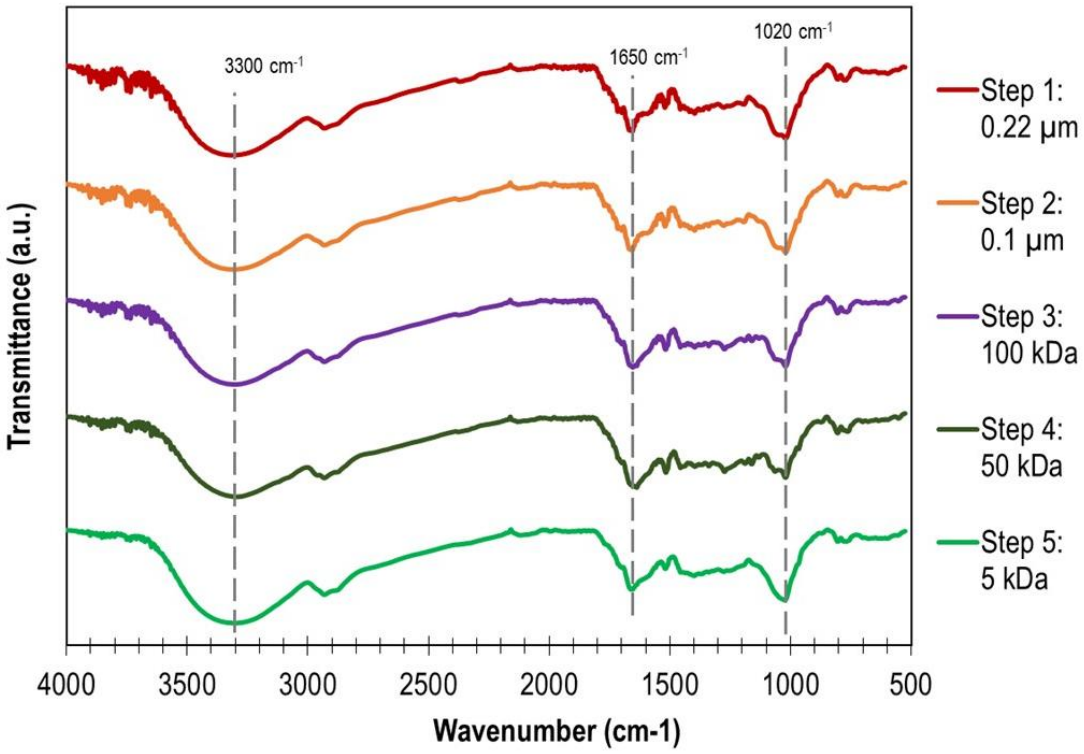

Figure 13. FTIR spectra of the lyophilized powders of the carbonaceous samples obtained after each separation step.

2.3.4.2. Thermo-gravimetric and Temperature Programmed Desorption coupled to Mass Spectrometry analyses

The thermal stability of samples of CDs with different purification degrees was inferred from the thermogravimetric profiles of the samples obtained under inert atmosphere (Figure 14). Four main regions of mass loss were identified. A first region between 25 and 150 °C is attributed to the moisture of the samples; the region between 150 and 300 °C corresponds to the decomposition of the carbonaceous matrix of the CDs, mainly oxygenated groups. At this range a difference is observed between the samples submitted to microfiltration and the samples submitted to

ultrafiltration, showing a higher loss mass in the case of the samples submitted to ultrafiltration, which indicates that these samples contained a higher proportion of oxygenated functional groups. This agrees with the expected removal of big carbon structures (graphitic or amorphous). In the range between 300 and 600 °C, the profiles were rather similar for all the samples with mass losses ranging from 27 to 28 wt.%, with just a slightly lower value for the most purified sample (5:5 kDa, 25 wt.%). The thermogravimetric profiles in the range 600-1000 °C were rather stable, with a low and similar mass loss for all the samples accounting for 3-6 wt.%.

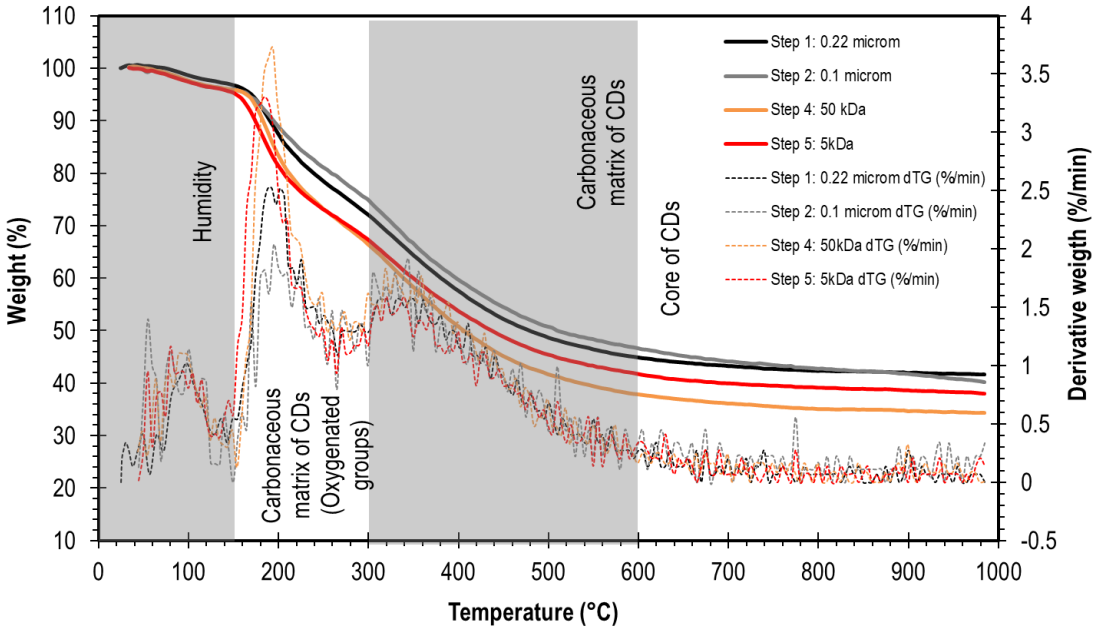

Figure 14. Thermogravimetric profiles under inert atmosphere for the lyophilized CDs solids after sequential purification steps

The total mass loss after the heating up to 1000 °C varied in a range of 58 and 66 wt.%, following a subtle decreasing trend as the number of separation steps was increased (Table 7).

Table 7. Mass losses (wt.%) from the thermogravimetric profiles obtained under inert atmosphere for different thermal ranges.

	Total Mass loss 25-1000°C [wt.%]	**Mass loss 25-150 °C [wt.%]**	**Mass loss 150-300 °C [wt.%]**	**Mass loss 300-600 °C [wt.%]**	**Mass loss 600-1000 °C [wt.%]**
Step 1: 0.22 µm	58.3	3.5	24.6	27.2	3.1
Step 2: 0.1 µm	59.8	4.2	25.8	27.7	6.2
Step 4: 50 kDa	65.7	4.2	34.2	28.0	3.4
Step 5: 5kDa	62.0	5.1	33.3	25.1	3.6

During the thermogravimetric analysis, the mixture of CDs particles and byproducts will decompose due to the increase in temperature. Certain quantity of gases will be liberated during the decomposition, most of them are typically CO and CO_2. The gases evolved from thermogravimetric analyses were characterized by mass spectrometry.

Mass Spectrometry is a technique used to identify unknown compounds, quantify known compounds, and elucidate the structure and chemical properties of molecules. During this kind of analysis, the sample could be destroyed by electron

impact or thermically methods. During the fragmentation, different ions are generated and analyzed according to their charge/mass ratio (m/z). Mass spectra consist of a series of competitive and consecutive unimolecular fragmentations in conjunction with thermal decomposition which provide additional data about the sample. To interpret the results of this technique, it is very important to understand the chemical processes and mechanism of the fragmentation of the particles.

The amounts of CO and CO_2 were quantified across the scan temperature range (Figure 15). These gases are related to the nature of oxygen containing groups in the carbonaceous materials (Rocha et al., 2023). The CO_2 profiles showed a wide band between 150 and 550 ºC for all the samples with small differences in the intensities, along with a shoulder at 150-300 ºC. These bands are attributed to the decomposition of carboxylic acids of different acidic strength (Araújo et al., 2017). The samples submitted to microfiltration with the 0.22 membrane showed CO and CO_2 evolution profiles with slight variations compared to the samples processed through filtration with the 0.1 µm membrane and ultrafiltration steps. The intensity of the bands was more pronounced for the samples with a higher number of purification steps (Table 8), indicating the higher proportion of carboxylic acids in these samples. A small band above 600 ºC was observed for sample 2:0.1 µm in the CO_2 profiles, which is attributed to the decomposition of lactones in this sample (Rocha et al., 2023).

The CO profiles also showed a multimodal pattern with a first wide peak at temperatures between 200 and 600 ºC again displaying a shoulder at 200-300 ºC,

and a second peak at temperatures above 800 ºC. The low temperature CO peaks are typically associated to the decomposition of carboxylic acids and anhydrides, while the evolution of CO at 400-700 ºC is associated with phenolic groups, and that above 750 °C is associated with the presence of ether, carbonyl and quinone groups (Rocha et al., 2023). The shoulder around 150-250 ºC in the CO profile may be ascribed to carboxylic acids, since it appears at the same temperatures in the CO_2 profiles; a similar assignment has been suggested in the literature, although the origin of this peak is not fully understood (Araújo et al., 2017). In addition, the low temperature peak in the CO profile (featuring around 200 ºC) has also been assigned to the decomposition of hydroxyl groups in oxidized graphene-derivatives (Araújo et al., 2017).

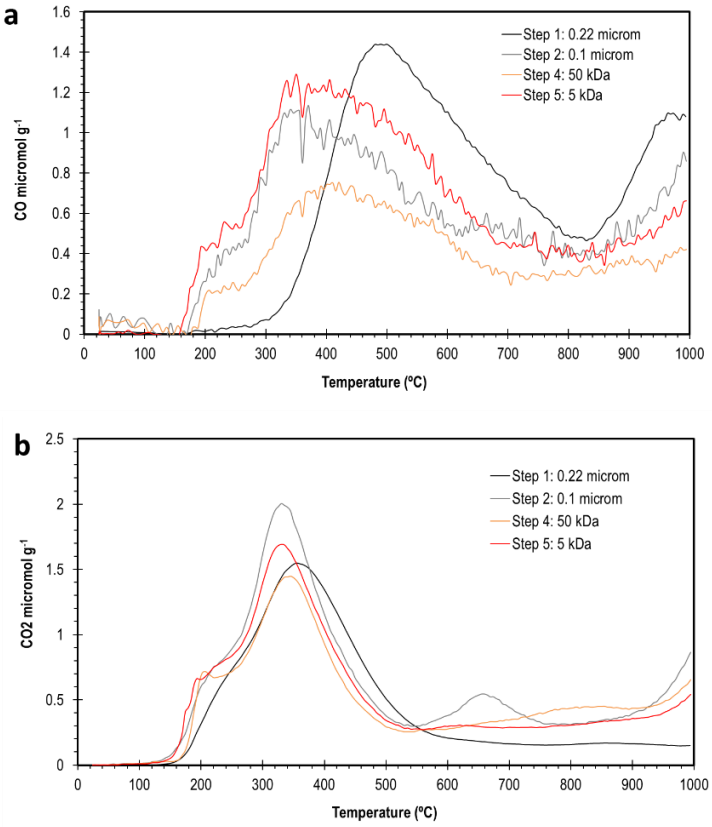

Figure 15. CO (a) and CO_2 (b) evolution profiles under inert atmosphere for the lyophilized CDs solids after sequential purification steps.

Table 8. Total amounts of CO_2 and CO released by TPD –MS and total amount of oxygen obtained from TPD data (assuming that all the surface oxygen is released as CO and/or CO_2).

	CO (µmol g^{-1})	**CO_2** (µmol g^{-1})	**Oxygen** (%)
1: 0.22 µm	587	410	32.6
2: 0.1 µm	522	559	33.5
4: 50 kDa	352	463	33.8
5: 5 kDa	580	481	33.0

For selected samples (i.e., 1: 0.22 μm, 4: 50 kDa and 5: 5 kDa) the thermal decomposition profiles were recorded at m/z values ranging from 50 to 300 with the aim to identify biomass decomposition by-products that could be present in the samples. The range of m/z values from 50 to 300 would cover molecules typically found during the decomposition of biomass precursors (Harding et al., 1991; Sawalha et al., 2009; Wypych, 2023; Xie et al., 2023; Zioga et al., 2022), that would not be removed by the sequential separation with membranes (Figure 1). It should be mentioned that m/z values are between 50 and 300 were obtained, and the only signals corresponding to m/z 51-58, 65-68, 77-79, 81, 82, 91, 92, 95, 96, 105, 109, and 110 values were detected for the samples, indicating that subproducts with a molecular weight higher than 110 and lower than 300 are not formed.

The m/z values of 53, 95 and 96 showed a bimodal shape, with a sharp peak between 150 and 200 ºC and a broad band extending between 250 and 400 ºC, in accordance with the thermogravimetric profiles (Figure 17). The intensity of the sharp peak observed at low temperature was more pronounced for the least filtrated samples. On the contrary, the intensity of the broad band was rather constant for all the samples.

At m/z values of 54-57, only the band between 250 and 400 ºC was observed with constant intensities in the samples, while at m/z of 58 the intensity of the band decreased with the purification step. These m/z values are associated with fragments of furfural, furanone and phenolic derivatives observed in the

decomposition of biomass precursors (Le Brech et al., 2016), and could correspond to compounds like acetone, propenal or propenol.

The mechanism of fragmentation of aromatic phenols is characterized by the analysis of intense peaks for the molecular ion, and by little indication of dehydration from phenol groups unless there is an adjacent functional group. For the profiles corresponding to m/z values of 109 and 110, a sharp peak featuring between 150 and 250 ºC, and to m/z values of 81 and 82, a broad peak between 250 and 450 ºC were observed in all the samples (Figure 17). These fragments can be related to phenolic 1,2-bencenediol, anisole, cresols, or methyl-phenols derivatives, common subproducts detected in the degradation of biomass (Castilla et al., 2021; Christensen et al., 2017; Fahmey et al., 2001; P. Li et al., 2022). In the case of 2-hydroxyphenol or 1,2-bencenediol (m/z = 110) mass spectrum, the appearance of [M-H_2O] fragment ion (m/z = 92), with its subsequent loss of CHO and CO forming [M-H2O-CHO]$^+$ (m/z = 63) and [M-H2O-CO]$^+$ (m/z = 64) ions are due to the “ortho effect'” of the two adjacent OH groups (Fahmey et al., 2001). Also, the spectrum of 2-hydroxyphenol molecular ion shows fragmentation characteristics of the presence of OH groups in aromatic ring, i.e. CHO and CO loss forming [M-CHO]$^+$ (m/z = 81) and [M-CO]$^+$ (m/z = 82). Subsequent loss of CHO of these ions leads to the formation of masses of m/z = 52, 53 and 54 (Fahmey et al., 2001) (Figure 16).

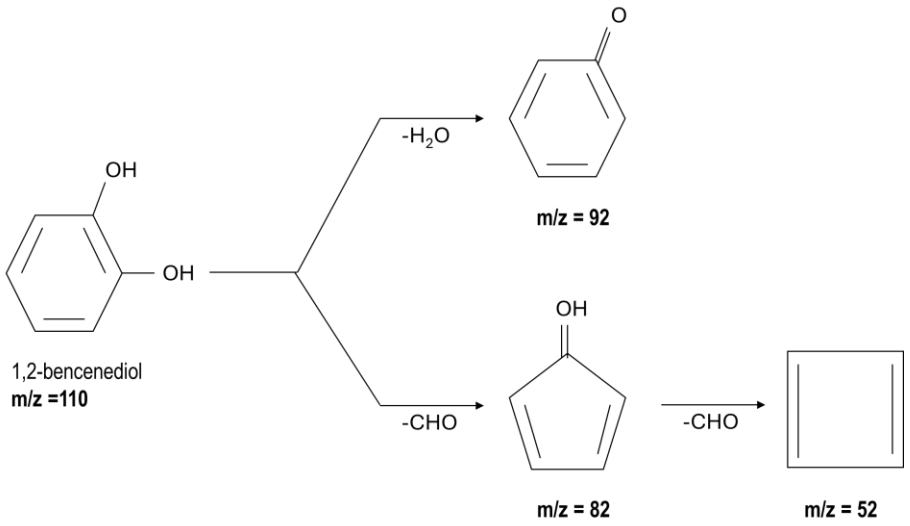

Figure 16.Fragmentation patterns associated with the decomposition of CDs

The intensity of the peak was rather similar for the samples after the first (0.22 μm) and fourth (50 kDa) separation steps but decreased substantially in comparison to the sample filtered at the fifth step (5 kDa), indicating the improvement in the purification of the sequential separation with the 5 kDa membrane. These results also point out that the mass loss observed in region 150-300 °C in the thermogravimetric profiles corresponds to the decomposition of the matrix of the CDs.

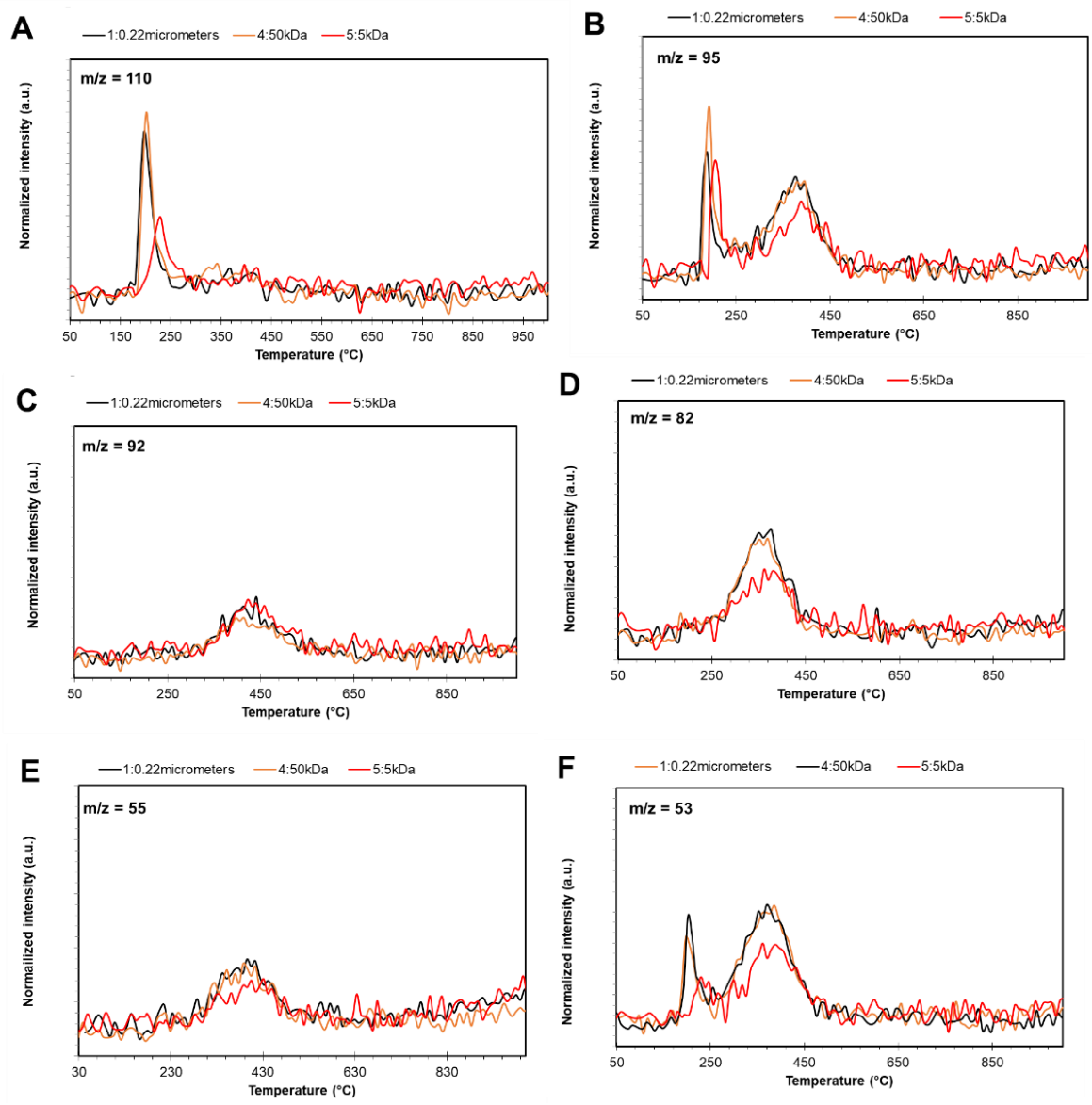

Figure 17. Selected thermal decomposition profiles of the m/z signals from the range 50-300 detected in the studies solids.

2.3.4.3. pH and Stability of Suspensions (Dynamic light scattering)

The nanoparticles in suspension are subjected to electrostatic and steric interactions that cause repulsion between the particles, and to Van del Waals and magnetic

interactions that promote attraction between them (Lim et al., 2013). Changes in the agglomeration tendencies of the particles at different purification degrees may be related to the influence of the surface chemistry of the material in the interparticle interactions (Pons et al., 2006). Additionally, hydrodynamic diameter upward trends in DLS are associated with the decrease of the diffusion coefficient values. As the concentration increases, the interactions between the particles are stronger, and the particles have a higher tendency to aggregate to form large particle clusters (Hassanzadeh et al., 2015; Lim et al., 2013).

Agglomeration of the particles is an important aspect to consider since this may cause self-quenching and turn off the fluorescence intensity of the material as a consequence of the proximity between the particles, which may disrupt the fluorescence transitions to non-radiative pathways (Tiong et al., 2015). The agglomeration and average size of the CDs in suspension was investigated by Dynamic Light Scattering for each fraction of the purification. The hydrodynamic diameter of the particles suspended in water with a solid loading of 0.25 mg mL-1 and pH adjusted to 6 was evaluated (Figure 19). The solids loading and the pH were selected after optimization experiments to obtain a suspension stable enough to execute particle size measurements for all the samples, otherwise, a poor reproducibility of the determination was obtained. For example, in highly concentrated dispersions a tendency of aggregation of the particles into large clusters are typically observed due to the favored interactions among the particles (Hassanzadeh et al., 2015; Lim et al., 2013).

The effect of pH was observable to the naked eye in the material suspensions, since, as shown in the figure, when the pH of the suspension was modified, the color of the suspension was modified. This effect is observed with greater intensity in the samples with a lower degree of purification.

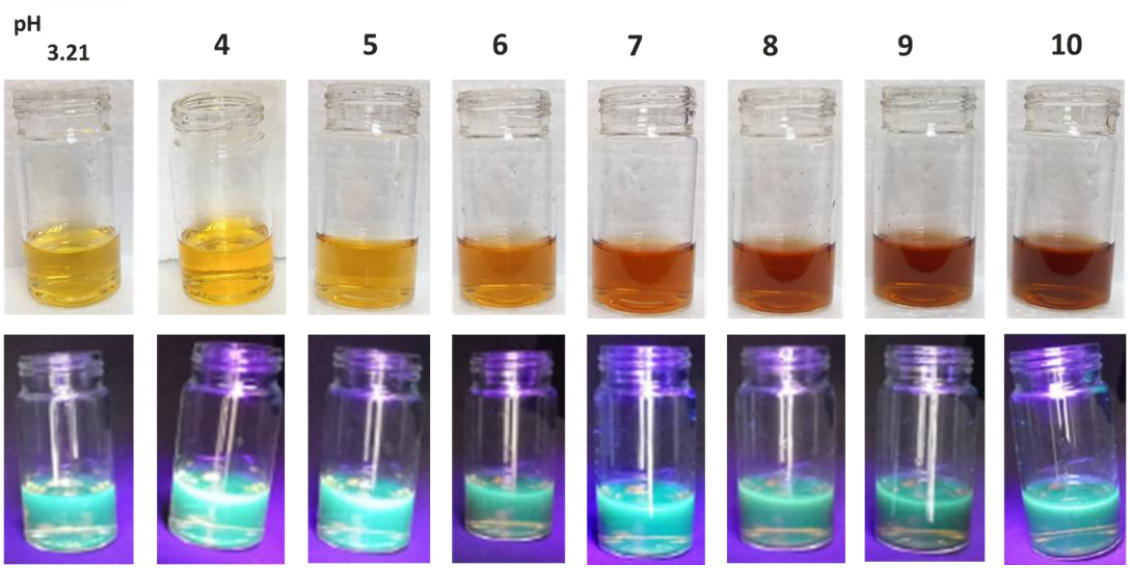

Figure 18. Difference in suspension color with respect to pH in a suspension of sample 1:0.22µm of CDs, at the concentration obtained from the MWA synthesis. The pH was adjusted with NaOH and HCl standardized solutions.

The samples prepared upon one and two separation steps showed a wide distribution of particle sizes, compared to the rest of the series (ca. 500 nm for sample 1:0.22 µm and 800 nm for sample 2:0.1 µm). The average particle size of these dispersions was more than one order of magnitude higher than those of the most purified samples (ca. below 10 nm). This points out the outstanding impact of the purification method in the eventual formation of large particle aggregates for a given composition. The distribution of particle size obtained from the DLS analyses

of the suspensions in the first two filtration steps agree with previous reports where it was observed that measurements executed to graphene oxide quantum dots derived through microwave-assisted hydrothermal degradation of cellulose at higher concentrations than 0.05 mg/mL, presented hydrodynamic diameter values higher than 100 nm (Hassanzadeh et al., 2015). The difference between the samples is mainly attributed to the presence of oligomeric fragments in the suspension, that would favor interparticle interactions and interaction with the solvent of the suspension. Note that in this work only one experimental protocol has been used for the synthesis of CDs, and that the difference among the studied samples was the sequential separation with different membrane pore sizes and the number of separation steps on the same dispersion.

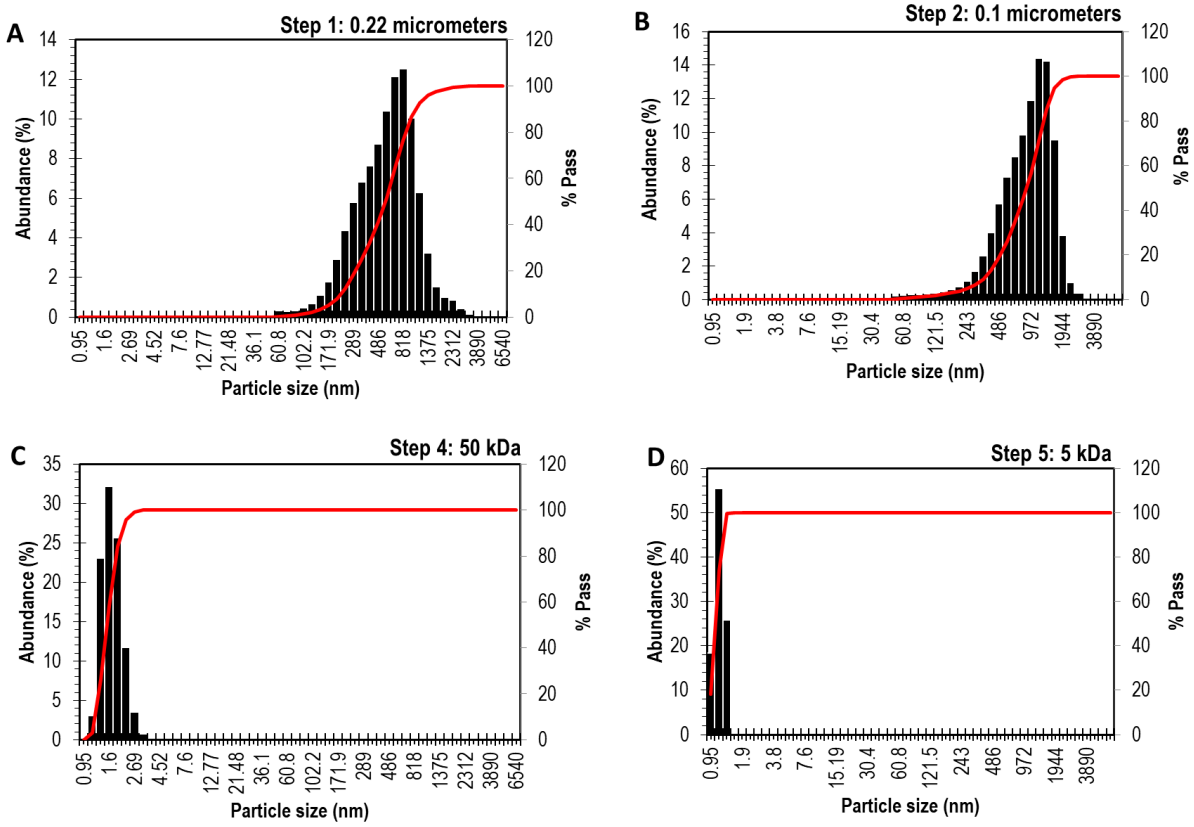

Figure 19. Histogram of particle size of a suspension of the material at the purification (A) step 1 (B), 2 (C), 4 (D) and 5 at pH around 6.5

2.3.4.4. Optical characterization

As a fast way to infer the presence of CDs in suspension, a qualitative analysis was performed. The yellow suspensions obtained from each purification step were irradiated with 395 nm light and showed photoluminescence emission. Nevertheless, this qualitative parameter is not useful as an indicator of the changes generated by the filtration process due to the samples from the first and last purification steps exhibit similar photoluminescence emission. In contrast, UV-vis and photoluminescence spectroscopy measurements that will be further discussed

indicate that there are differences between the optical characteristics of the samples and assessed the impact of the purification process on the optical properties of the materials.

UV-vis absorption spectra give information about the amount of light absorbed, regardless is stabilization to the ground state through radiative or non-radiative transitions, whereas the photoluminescence spectroscopy provides information about the amount of light absorbed that follows a radiative transition (i.e., photoluminescence emission) to return to the fundamental state.

Aqueous suspensions of the materials were prepared at different solid loading values, and the 0.25 mg mL^{-1} suspensions were selected because this concentration shows absorption values lower than 2 arbitrary units in the range from 220 to 600 nm and allows a proper comparison of the optical properties of the samples.

Figure 20a shows the UV-vis absorption spectra of aqueous suspensions at a loading of 0.25 mg mL^{-1}. As seen, all the suspensions presented rather similar profiles, characterized by a broad absorption band in the UV region and a long tail extending to the visible region. The absorption band is characterized by a main peak located at 280 nm, and shoulders of less intense peaks at 220 and 340 nm. The peaks at 280 and 220 nm can be attributed to π-π* transitions of sp^2 carbon atoms (i.e., a graphitic carbon core), and the bands between 300-400 nm are attributed to n-π* transitions in C=O bonds (i.e., functionalized carbon atoms) (W. Liu et al., 2017).

The samples presented differences in the intensity of the absorbance even when all the dispersions were prepared with the same concentration. The absorbance of sample 2:0.1 µm was the highest among the series, suggesting the presence of a larger number of absorbing groups in the suspension. The intensity of the bands was somewhat decreasing with the number of separation steps, although differences are subtle. This suggests that only a small fraction of light absorbing species were removed during the purification steps, pointing out that the CDs matrix and the small molecules (<5 kDa) are the main responsible for the observed optical features (with a less contribution from the impurities removed during microfiltration). These observations coincide with those made by Essner *et al.*, who proposed a nanofiltration membrane separation process for the purification of citric acid derived CDs. Essner *et al.* identified two different populations of fluorophores which were species smaller than 1 kDa, responsible for most of the fluorescence of the samples, and species smaller than 50 kDa, which were low quantum yield emitters [9].

The impact of the separation steps was more clearly seen in the emission features of the samples. The shape of the photoluminescence spectra was similar for all the samples, characterized by a broad emission with a maximum at ca. 450 nm and a pronounced shoulder at around 550 nm. The multimodal character of the photoluminescence emission of the samples will be deeply discussed in the third chapter of this document. The photoluminescence emission of the samples was compared to that of pure water to confirm that the observed emissions originated entirely from the material (Figure 20b). The intensity of the emission at the maximum

position did not show a clear correlation with the different filtration steps, following the trend: 2:0.1 μm >> 3:100 kDa >> 4:50 kDa ~ 1:0.22 μm > 5:5 kDa. The largest emission intensities were obtained for the sample after 2 steps of purification (membrane 0.1 μm), and the lowest one was measured for the most purified sample (membrane 5 kDa). Although this suggests a partial removal of some emitting species in the suspensions upon the filtration, it also confirms that the most purified sample still displays a notorious emission. The removed emitting groups may be related to the particles causing the liberation of 1,2-benzenediol from the thermal decomposition of the material, whose concentration is also decreasing along the purification process.

The absolute quantum yields of the dispersions at 0.25 mg mL^{-1} obtained upon excitation at 375 nm ranged between 3.4 % for the least purified sample and 5.2 % for the most purified one. Although these values are not among the highest reported for carbon dots, they are comparable to those reported for non-metal doped carbon dots, between 1 and 9.6% (Nguyen et al., 2022). Despite samples 1:0.22 μm and 3:100 kDa displayed rather similar absorbance features (Figure 20a), the emission of sample 3:100 kDa was more pronounced than that of sample 1:0.22 μm (Figure 20b). These differences may be related to quenching effects promoted by light-absorbing compounds involving non-radiative transitions in the least purified sample (1:0.22 μm). The optical properties of CDs will be further discussed in the third chapter of this document.

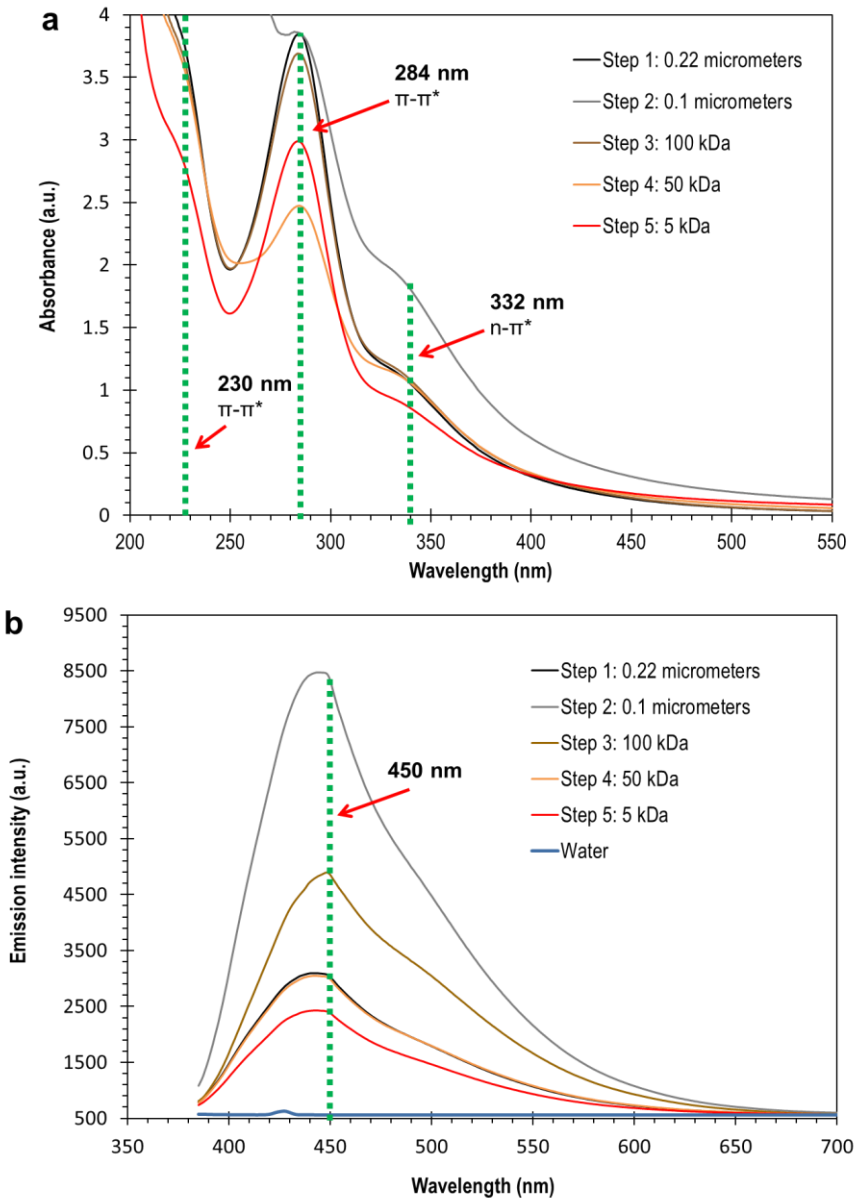

Figure 20. (a) UV-vis and (b) photoluminescence spectra upon excitation at 375 nm of aqueous suspensions at 0.25 mg mL^{-1} after each separation step. Green dotted lines highlight the main peaks of spectra

2.3.5. Characterization of purified CDs

2.3.5.1. FT-Infrared spectroscopy

The FTIR spectrum of the powder obtained from the full sequential separation, i.e. 0.22 and 0.1 micrometers, 100, 50 and 5 kDa membranes (Figure 21) shows the broad band centered at 3300 cm^{-1} related to O-H stretching vibrations, the bands around 2930 and 2880 cm^{-1} which correspond with the stretching vibrations of sp^2 and sp^3 C-H. The shoulder at 1700 cm^{-1} overlapped with the broad band centered around 1650 cm^{-1} could be associated with the stretching of the carbonyl group of a carboxylic acid, which is corroborated with the presence of the weak bands centered at 1270 and 1395 cm^{-1} which are associated with the torsion of the carbonyl group. The band related to the presence of primary amines (-NH_2) and to the presence of carbonyl groups from aldehydes or ketones appears around 1650 cm^{-1}. The band at 1020 cm^{-1} related to primary alcohols or sulfoxides is also present, as well as the band around 1513 cm^{-1} associated with secondary amines (-NH-).

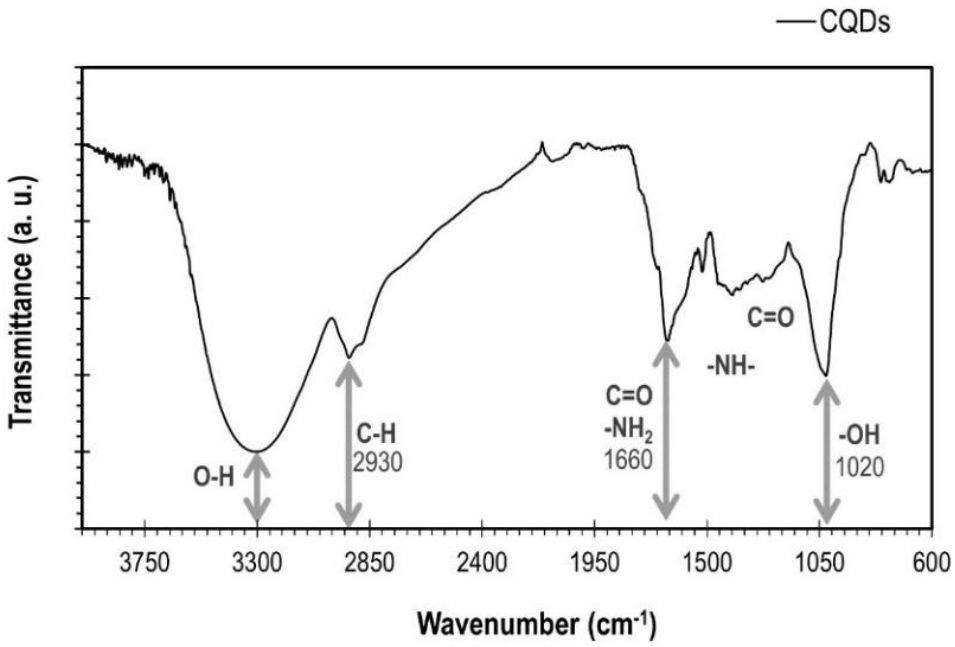

Figure 21. FTIR spectrum of purified biomass derived CDs

2.3.5.2. Raman Spectroscopy

Raman spectrum of the CDs-5kDa sample was deconvoluted to identify the contributions of the D and G bands, which are associated with amorphous and graphitic carbon, respectively (Ania et al., 2020; Sadezky et al., 2005). Deconvoluted Raman spectrum showed the characteristic D and G bands at 1340 and 1588 cm^{-1} (Figure 22). The corresponding I_D/I_G ratio of the intensity of these bands was 0.94, indicating a significant contribution from graphitic domains relative to sp^3 hybridized carbon. However, as shown in Figure 22, the area under the D band is more prominent, suggesting that structural disorder still plays a major role in the composition of the material.

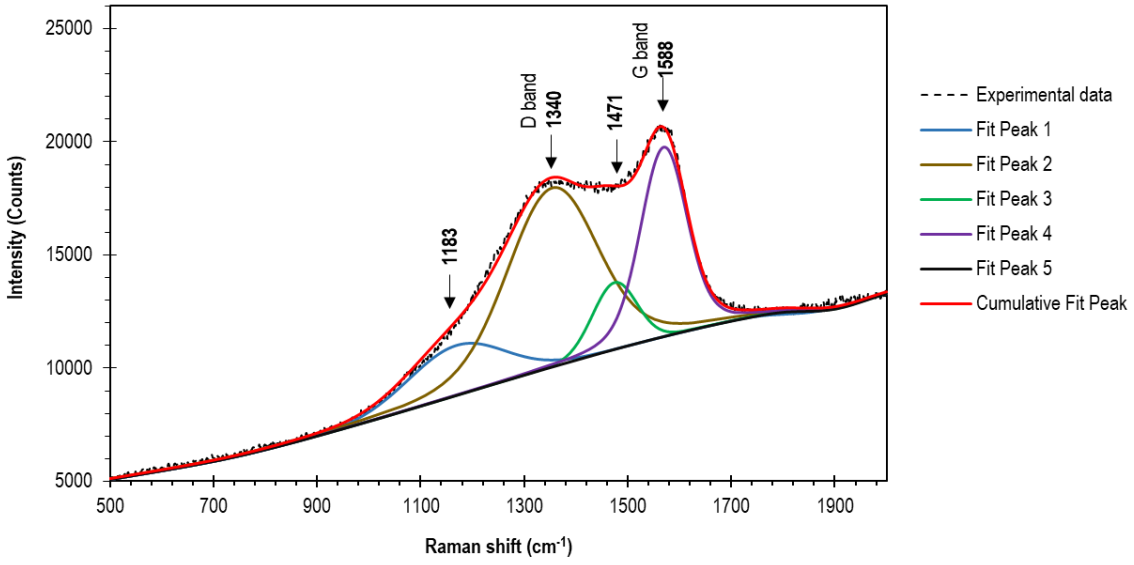

Figure 22. Raman spectrum of purified biomass derived CDs

2.3.5.3. X-ray Photoelectron Spectroscopy

X-ray photoelectron spectroscopy (XPS) provided information about the surface functionalization and elemental composition of the biomass derived CDs. Figure 23 show the high-resolution spectra of the C_{1s} core energy level. The binding energy profile spectrum was deconvoluted to various contributions (Table 9). In agreement with FTIR analyses, the XPS spectrum deconvolution showed carbon to carbon bonds in sp^2 (~284.5 eV), sp^3 configurations (~285.1 eV); C-O single bond (~286.1 eV) associated to phenolic, alkoxy, epoxides and ether configurations; C-N bond (~286.9 eV) attributed to carbon in nitrogen groups, like amines or amides; C=O

bond (~287.7eV) assigned to carbonyl groups of ketone, O-C=O bonds associated with carboxylic and ester groups (~289 eV), two small contributions of π-π* transitions of aromatic carbons (~290.7 eV) and the satellite of C=O component (~292.3 eV).

The C-C sp^2 contribution supports the presence of graphitic carbon structures, as was suggested by FTIR and Raman. The major contribution to the C_{1s} spectrum corresponds to the C-O single bond assigned to phenolic, alkoxy, epoxides and ether configurations. These observations agree with the FTIR spectroscopy results. The combined atomic percentages of C-O, C=O, and O-C=O contributions (34.8%) closely align with the measured oxygen content in the sample (32.9%). Similarly, the minor contribution of C-N (1.6%) corresponds with the low nitrogen content in the sample (2.6%). Table 9 lists the relative abundance (%) of each element and functional group in the sample.

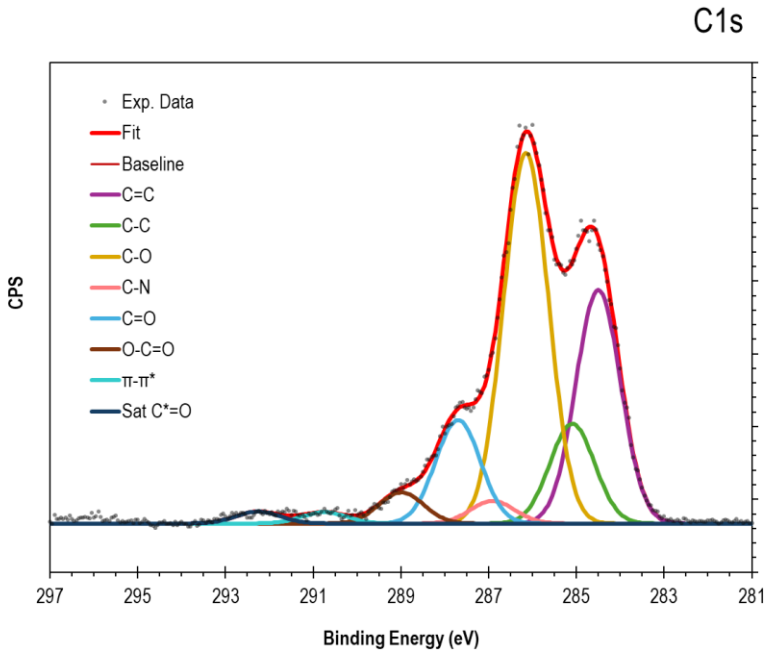

Figure 23. High resolution XPS spectra of the C_{1s} peak of biomass derived CDs.

Figure 24 shows the O_{1s} core level signal of the sample, decomposed in three peaks associated to C=O in ketone groups (~531.1 eV), C-O (~532.5 eV), and C-O-C bonds from ether groups (~534.3 eV). In agreement with the trends observed in the C_{1s} core level, the highest atomic percentage is attributed to the C-O single bond (26.6%), followed by the presence of oxygen from ketone groups (2.5%) (Table 9). The binding energy profile of N_{1s} indicates de presence of pyrrolic and pyridine type bonds (~399.8 eV) and a small proportion of oxidized nitrogen (~402.1 eV). The presence of graphitic, pyridinic, pyrrolic, and amino centers in CDs is important because it has shown effects in the optical and electrochemical responses of the CDs (Vercelli et al., 2021).

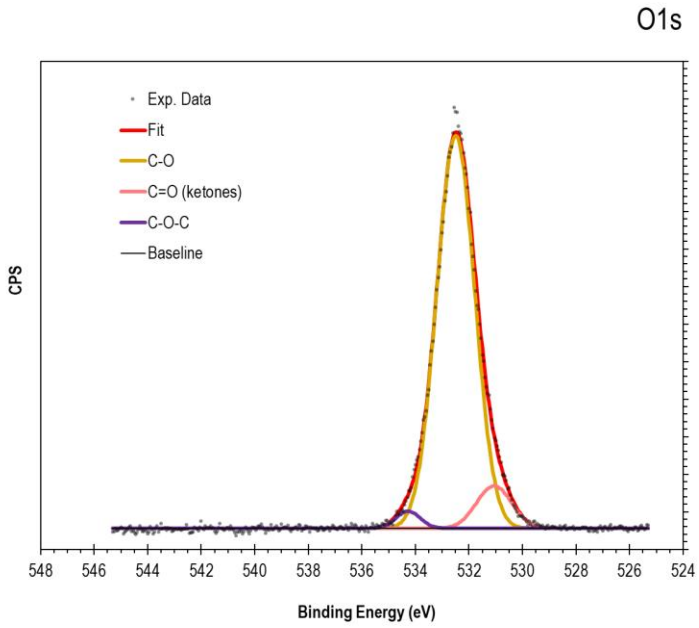

Figure 24. High resolution XPS spectra of the O_{1s} peak of biomass derived CDs.

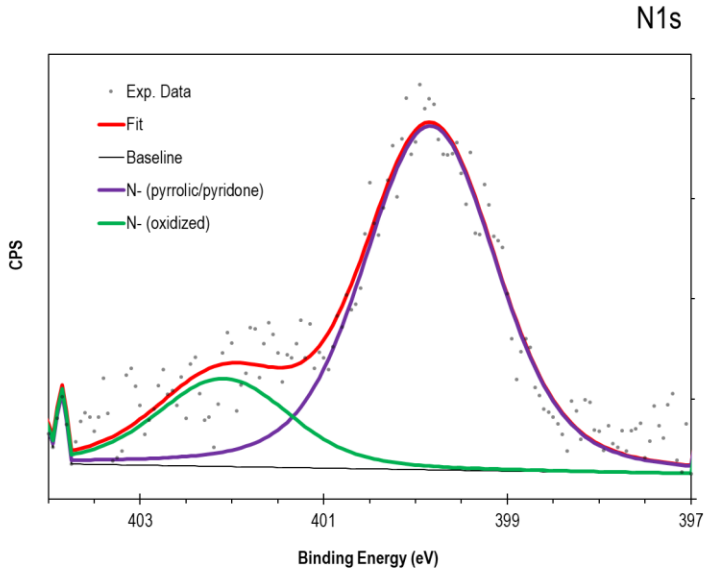

Figure 25. High resolution XPS spectra of the N_{1s} peak of biomass derived CDs.

Table 9. Concentration of elements (atomic %) and relative abundance (%) of the different peaks assigned from the deconvolution of the C_{1s}, O_{1s}, and N_{1s} core energy levels of biomass-derived CDs

CDs	C_{1s}	N_{1s}	O_{1s}	Si_{2p}	Na_{1s}
Atomic %	60.9	2.6	32.9	0.9	2.6

	C1s							
	C=C	**C-C**	**C-O**	**C=O**	**O-C=O**	**C-N**	**π-π***	**sat. C=O**
Relative abundance (%)	26.4	11.3	41.9	11.7	3.5	2.5	1.3	1.3
Atomic %	16.1	6.9	25.5	7.1	2.1	1.6	0.8	0.8

	O1s		
	C-O	**C=O (ketones)**	**C-O-C**
Relative abundance (%)	88.7	8.9	2.5
Atomic %	29.2	2.9	0.8

	N1s	
	N- (pyrrolic/pyridone)	**N- (oxidized)**
Relative abundance (%)	79.6	20.4
Atomic %	2.1	0.5

2.3.5.4. Potentiometric titration

The point of zero charge (pH_{PZC}) is defined by the crossover point of the proton binding curves with the pH axis. The pH_{PZC} of the purified CDs is 4.5 (Figure 26A), which means that at pH higher than 4.5, the particles in suspension will present negatively charged functional groups, for example, deprotonated carboxylic acids (Nxele & Nyokong, 2022).

Figure 26B shows the pKa distribution obtained from the analysis of the proton binding curve according to the method proposed by Jagiello *et al.* (Bandosz *et al.*, 1993; Jagiellot, 1994). The pKa distribution showed peaks at 4.7, 6.2, 7.7, and 9.7, which suggests the presence of different proton exchange sites. Table 10 shows the area and relative percentage of each peak.

The pKa value between 4.7 and 6.2 could be associated to carboxylic groups, at 7.7 with lactones, and at 9.4 with phenolic groups (C-OH bonds) (Boehm, 1994; D. Leon y Leon & Radovic, 1993; Leon et al., 1992). These results corroborate the inferred heterogeneous chemical surface with acidic functionalities that contribute to the hydrophilicity and stability of the carbonaceous particles in aqueous suspension.

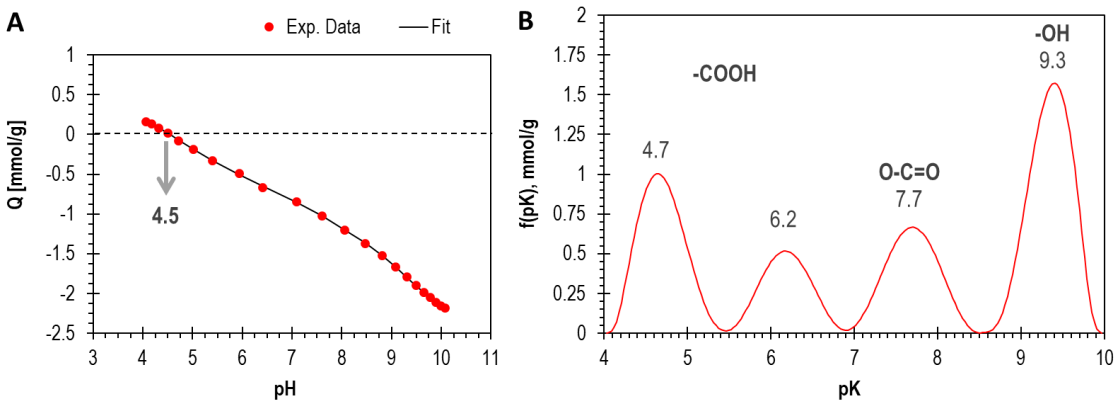

Figure 26. (A) Potentiometric titration and (B) pKa binding curve (0.2 mg/mL suspension of biomass derived CDs)

Table 10. Areas and percentage of the pKa binding curve (0.2 mg/mL suspension of biomass derived CDs).

Peak center	**4.7**	**6.2**	**7.7**	**9.3**
Area [mmol/g]	0.7	0.4	0.5	1.0
[%]	26.4	14.5	20.1	39.1

Table 11 shows the comparison between the concentration of C-O and C=O groups determined by potentiometric titration and XPS. Carbonyls from lactones, esters, ketone, and carboxyl acids detected by potentiometric titration was much higher than percentage of C=O groups detected by XPS. These discrepancies can be attributed to the inherent differences in their analytical approaches. XPS is a semi-quantitative technique that evaluates the surface composition of a specific point of the material,

whereas potentiometric titration assesses the functional groups of the entire exposed area of the material.

Table 11. Comparison between the atomic percentage of the C-O and C=O bonds from the C_{1s} and O_{1s} deconvolutions and the corresponding results of the potentiometric titration.

		XPS [Atomic %]		Potentiometric titration [%]
		C1s	O1s	
C-O	Bridging oxygen, hydroxyl, alkoxy, epoxides	25.5	29.2	39.1
C=O	Lactones, esters, and ketones	9.2	2.9	20.1
C=O	Carboxyl acids	2.1	Not detected	40.9

2.3.5.5. Nuclear Magnetic Resonance

Purified orange peel derived CDs were qualitatively analyzed by ^{1}H and ^{13}C Nuclear Magnetic Resonance (NMR) to expand our knowledge regarding their surface chemistry. In this sense, the ^{1}H-NMR spectrum (Figure 27A) shows the presence of proton atoms attached to sp^3 hybridized carbon in the region from 0.5 to 6 ppm. The sp^3 carbon atoms were identified by their association with alkane protons and linked to ether, epoxy, carbonyl, amino, and amide functional groups. On the other hand, protons associated with carbon atoms with sp^2 hybridization were found in the region

between 6 and 9 ppm and they were related to aromatic or aldehyde protons. With the aim of decreasing the water signal, the acquisition of the NMR spectrum was also obtained with water suppression (Figure 27B). Despite the study conditions related to this technique are not sensitive enough to obtain detailed data, it is possible to infer that carbon atoms with sp^3 hybridization shows higher abundance compared to atoms with sp^2 hybridization. This information was corroborated by ^{13}C-NMR analysis.

According to literature reports (De & Karak, 2013; Jia et al., 2012; Kansay et al., 2023; Mintz et al., 2021; Nallayagari et al., 2022), in the ^{13}C-NMR spectrum a first zone between 10-105 ppm was also associated with sp^3 hybridized carbon atoms, corresponding to alkyl substituents (10 to 50 ppm), C-O and C-N single bonds in hydroxyl, amine, and amide groups (50-80 ppm) and carbons linked to ether, epoxide, and terminal C=C bonds (80-105 ppm). The region between 100-120 ppm was associated with sp^2 hybridized carbon atoms, and the signals between 150-190 ppm can be related to the presence of C=O bonds in amides, carboxylic acids, or aldehydes.

In addition, a ^{13}C Attached Proton Test experiment (APT) was conducted with the aim of providing information regarding the number of hydrogen atoms bonded to a carbon atom. The APT spectra) revealed the signals attributed to the resonance of quaternary carbons and methylene groups (featuring as negative signals), while carbons bonded to an odd number of protons (e.g., methine, methyl groups) appear in the positive axis. Qualitative NMR analyzes corroborate in the carbon-based

material the presence of sp^2 and sp^3 hybridized carbon atoms at the nanoscopic level corresponding to various functional groups, which have also been described with the thermal decomposition profiles and the FTIR spectroscopy.

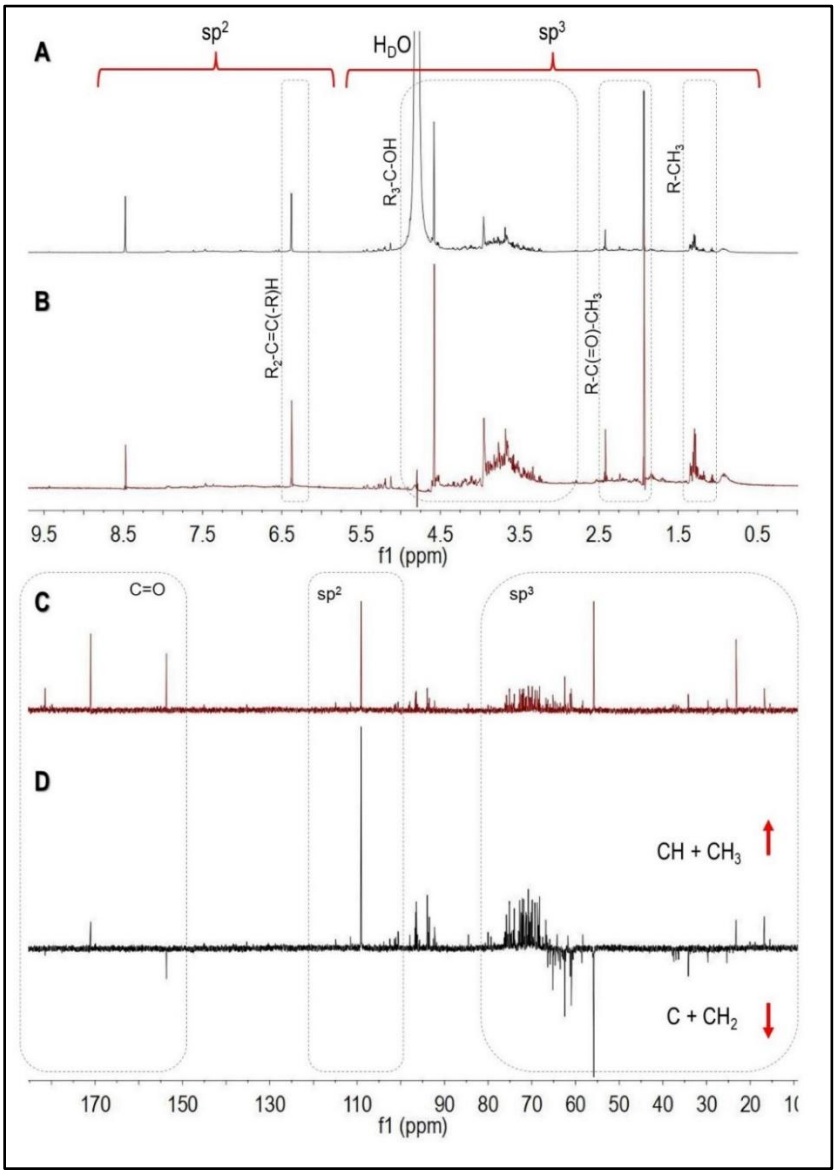

Figure 27. ^{1}H-NMR spectrum of CDs from separation step 5:5 kDa in D_2O at 500 MHz (A) and with water suppression at 0.05 mg/mL (B) in D_2O at 500 MHz. $^{13}C^{1}$H-NMR spectrum of CDs obtained from separation step 5:5 kDa (C) and $^{13}C^{1}$H-APT NMR spectrum (D) in D_2O at 125 MHz.

2.3.5.6. Hydrodynamic diameter and Z Potential

To evaluate the surface charge of the material avoiding interparticle interactions, a 0.05 mg/mL suspension of the purified material was analyzed at different pH conditions. The analysis showed that pH variations cause differences in the particle size distributions detected. In order to perform the measurements, it was ensured to have a zeta potential higher than 30, since zeta potential values below 30, suggest a low stability in the suspension. Typically, high positive or negative zeta potential values are indicative of better stability for particles in suspension (Nxele & Nyokong, 2022).

At a pH of 6.8, the suspension yielded a zeta potential of -34.8 and hydrodynamic diameters around 3.5 nm (Figure 28). These observations agree with reports in the literature on graphene oxide quantum dots synthetized through microwave-assisted hydrothermal degradation of cellulose that showed properly dispersed nanometric suspensions at concentrations around 0.05 and 0.07 mg mL^{-1} [42]. This suspension was dropped multiple times on the carbon-coated cooper grid which was further employed to conduct transmission electron microscopy observations.

Figure 28 shows the zeta potential of the diluted suspension of CDs at pH conditions between 4 and 5.2. In this range, a clear trend in the zeta potential values is observed; at pH values below 4.5, positive z-potential values are observed, but above 4.5, the values of zeta potential are negative, in consequence, 4.5 is defined

as the isoelectric point of the sample. This value coincides with the point of zero charge reported in this document.

The isoelectric point provides information regarding the surface charge of the particles in suspension. An isoelectric point of 4.5 coincides with the presence of acidic groups on the particle surface, corroborating the previously discussed characterization results, which suggested the abundance of oxygenated groups.

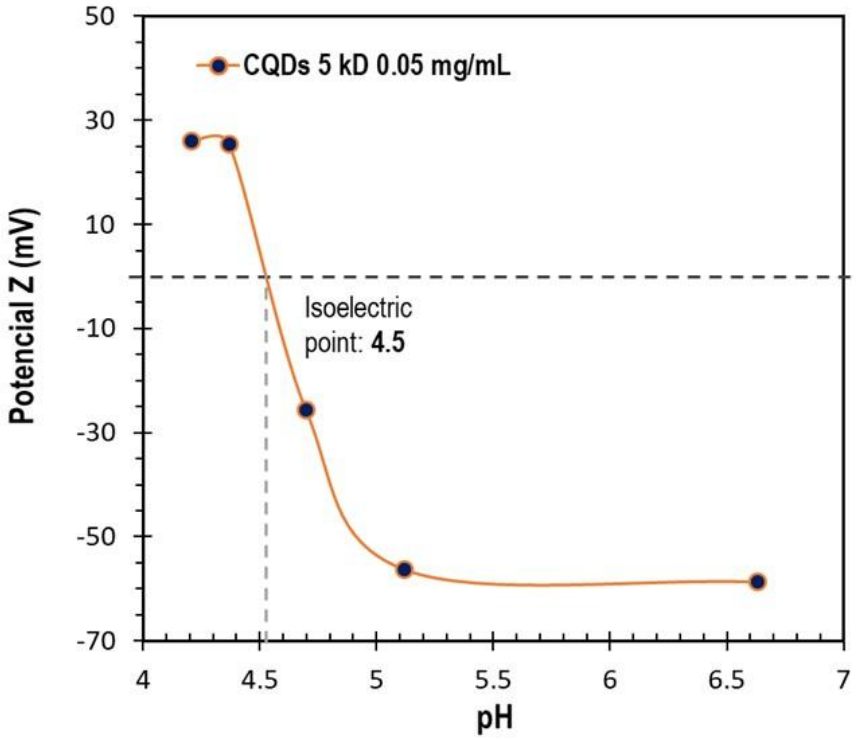

Figure 28. Isoelectric point of orange peel derived Carbon Dots

2.3.5.7. Transmission electron microscopy

Figure 29 shows micrographs obtained by transmission electron microscopy (TEM). To perform the analyses, a 0.05 mg/mL suspension of purified CDs with a pH of 6.8 was dropped on a carbon-coated cooper grid. In agreement with the DLS results, a homogeneous dispersion of spherical nanoparticles with an average particle size of 3.4 ± 0.9 nm was observed.

The particles presented well-defined crystallographic planes with a d-spacing of 0.21 nm, that correspond to the (100) plane of graphitic carbon with sp^2 hybridization, as referenced in the crystallographic chart JCPDS 26-1076. Similar d-spacing values have been widely reported in the literature for CDs obtained from various citrus or lignocellulosic precursors, such as grapefruit peel (W. Lu et al., 2012), citrus peel (Gudimella et al., 2021), microcrystalline cellulose (Wu et al., 2017), and lignin (J. Xu et al., 2021).

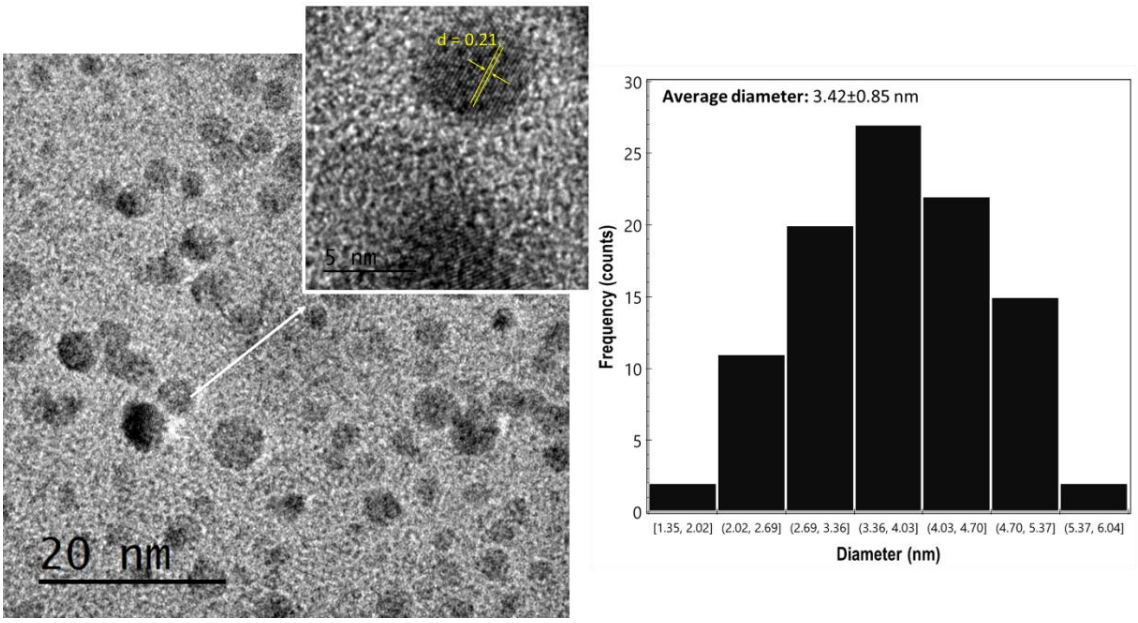

Figure 29. HR-TEM micrographs of CDs-5:5kDa at 0.05 mg/mL and interlayer distance of the particles

2.4. Summary

- Orange peel employed to generate CDs showed a huge diversity of functional groups before the acid wash, which indicates a high chemical complexity of the agro-industrial waste. Orange peel after acid wash conducted the removal of components with ester, hydroxyl, and carbonyl groups. This approach successfully reduced the complexity of the precursor.
- The purification of orange peel derived Carbon Dots (CDs) with microfiltration and ultrafiltration membranes though a sequential filtration process showed good effectiveness and higher yields compared to other methods like chromatography. The membranes used were carefully selected based on their retention rates and considering the expected products from the biomass decomposition.
- The agglomeration tendencies of the nanoparticles in suspension, analyzed by Dynamic Light Scattering showed notorious changes between the samples, which indicates that even though techniques like FTIR or TGA does not show important differences between the samples, the purification degree of the samples affect their properties. Additionally, the absolute quantum yields of the suspensions ranged between 3.4% and 5.2% for the least purified sample and the most purified one, respectively. The physicochemical properties of the materials obtained from each stage of the sequential separation were analyzed to evaluate the effect of synthesis by-products present alongside the CDs.

— The material sequentially filtered until the 5 kDa membrane showed spherical particles with diameters of 3.42 ± 0.85 nm, as well as sp^3 and sp^2 hybridized carbon domains functionalized with oxygenated groups. In general, the characterization results indicate that CDs have a heterogeneous chemical surface with the presence of hydroxyl, ketone, carboxylic acids, ether, pyrrolic, pyridine and oxidized nitrogen functional groups. These groups attached to the carbon core of the material contribute to the hydrophilicity and stability of the carbonaceous particles in aqueous suspension and may be related with the photoluminescence center of the samples.

Chapter 3

Photoluminescence of Carbon Dots

Adapted from: Gonzalez-Vera, A.S., Perrin, G., Botsoa, J., Ntsoenzok, E., Chazaro-Ruiz L.F., Rangel-Mendez, & R., Ania, C. (2025) *Analyzing photoluminescence emission quenching effects in colloidal suspensions of carbon dots*. Colloids and Surfaces A: Physicochemical and Engineering Aspects. **Submitted**.

Chapter 3: Photoluminescence of Carbon Dots

3.1. Introduction

In this chapter, an evaluation of the photoluminescence properties of biomass-derived CDs suspensions is presented. Surprisingly, the photoluminescence emission showed important variations just as effect of the solid loading of material in suspension. The emission spectra were deconvoluted following mathematical and chemical criteria established from prior experimental and theoretical investigations. The deconvoluted spectral data were correlated with the physicochemical properties of the CDs, determined through dynamic light scattering, potentiometric titration, FTIR, Raman, and X-ray photoelectron spectroscopy, as detailed in the previous chapter. The characterization enabled the identification of different functional groups and carbon structures that may constitute the photoluminescence centers responsible for the photoluminescence emission of the suspensions containing CDs. The photoluminescence emission of CD suspensions under different excitation wavelengths, together with the analysis of their excitation spectra, were used to

propose a model describing the behavior of the nanoparticles in suspension and their influence on the observed photoluminescence.

3.2. Materials and methods

3.2.1. Synthesis and purification of CDs

Orange peel was collected from a local market in San Luis Potosi, Mexico, dried, and pulverized. The orange peel powder was washed with 1 M HCl solution for 24 hours and rinsed with deionized water until reaching a pH of four and left to dry at 90 °C to obtain a powder. 100 mg of this powder was suspended in 15 mL of deionized water and placed in a microwave oven (Nanowave 400 Anton Paar GmbH) at 220 °C for 30 minutes for a microwave-assisted hydrothermal synthesis. The as-obtained suspension was sequentially filtrated with a Sterile Millex filter of 0.22 µm, a Durapore membrane of 0.1 µm, and with Spectrum MicroKros TC Hollow Fiber Filters with molecular weight cut-offs of 100, 50, and 5 kDa to remove synthesis by-products. The obtained suspension was adjusted at a pH of seven with 0.1 M NaOH solution and freeze-dried to get the material in powder.

3.2.2. Characterization of CDs suspensions

CDs powder was resuspended in deionized water to prepare suspension at different concentrations to be analyzed. Hydrodynamic diameter size and zeta potential were determined by electrophoresis by a NANOTRAC WAVE II equipment at room temperature and various pH values. UV-vis spectra were obtained in an Aquamate Thermo Spectronic spectrophotometer. Photoluminescence spectra were recorded

on a Horiba Jobin Yvon IHR320MST2 spectrometer, driven by Syner JY software. All the experiments were carried out under the same experimental conditions. The wavelength of the exciting laser source was 375 nm in most of the experiments. To identify different emission centers, the spectra of suspensions with varying solid loadings were deconvoluted using Gaussian functions with similar FWHM in the software Fityk.

3.3. Results and discussions

3.3.1. Agglomeration tendencies of CDs

The concentration of the most purified-carbonaceous material from step 5: 5kDa, in an aqueous suspension affected the colloidal distribution of the suspended particles. Figure 30 shows the distributions of hydrodynamic diameter size of the CDs suspensions with concentrations of 4, 0.4 and 0.04 mg/mL at pH 7.

The 4 mg/mL suspension showed the presence of particles with a range of size between 20 and 500 nm. As the concentration of CDs suspensions decreased, the hydrodynamic diameter value detected also decreased. In the 0.04 mg/mL suspension it was possible to measure hydrodynamic diameters between 0.95 and 15 nm, which coincides with the diameter of isolated CDs nanoparticles observed by HR-TEM.

The presence of particles with diameters between 20 and 500 nm in concentrated suspensions could be attributed to agglomeration processes. The increase of the solid loading in suspensions enhanced the physical proximity between CDs and the

organic molecules that form molecular states (Gude et al., 2016; Hassanzadeh et al., 2015; Lim et al., 2013; Roy et al., 2018), thereby promoting the formation of clusters. Other factors that can contribute to the formation of aggregated structures are the presence of oxygenated functional groups at the surface of the CDs, dipole–dipole, π–π stacking and van der Waals interactions.

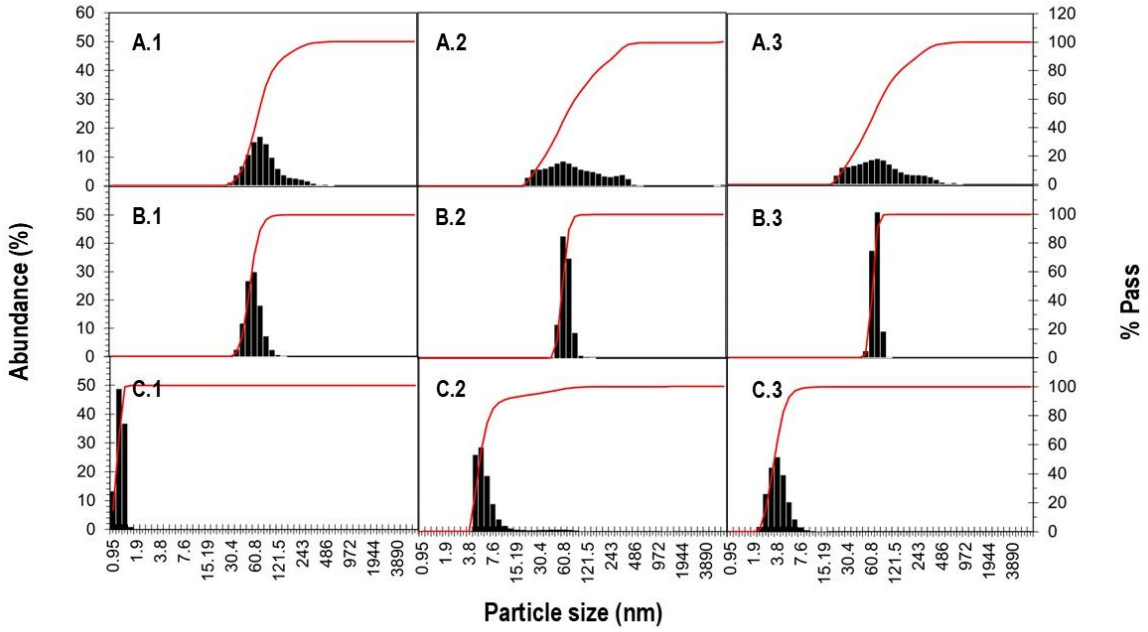

Figure 30. Particle size distribution of suspensions at concentrations of (A) 4 (B) 0.4 and (C) 0.04 mg/mL. %Pass indicates the percentage of particles in the sample with diameters less than or equal to the specified value

3.3.2. Optical characterization

Figure 31A shows the UV-vis spectra of the suspensions at different material solid loading levels. The UV-vis spectra presented high absorbance in the UV region, with a long extending into the visible and NIR regions. The spectra exhibited peaks at around 210, 284 and 325 nm, which could be attributed to π-π* transition of the C=C

bond, and n→π* transition of the C=O bond, respectively. In concentrated suspensions, the absorbance in the visible range notably increased. Also, it is possible to observe how the absorption of the sample gradually decreased along with the concentration of the material in suspension, following Lambert-Beer's law. At 500 nm wavelength, the suspensions presented a good linear correlation between absorbances and material solid loading, with an R^2 value of 0.9998 (Figure 31B).

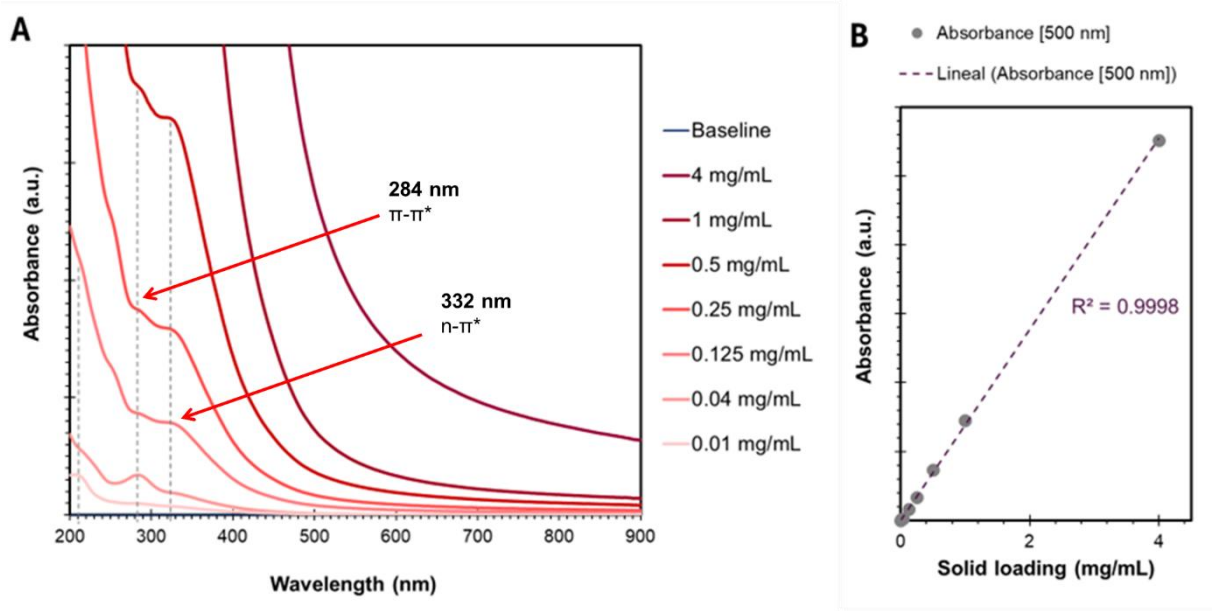

Figure 31. (A) UV-vis spectra of CDs suspensions at different concentrations. Dotted grey lines indicate the absorbance peaks observed for the material. (B) Absorbance with respect to the concentration at 500 nm.

Figure 32 shows emission photoluminescence spectra of suspensions of CDs with solid loading of 4, 1, 0.5, 0.04, and 0.018 mg/mL, which were excited with a 375 nm light. The spectra exhibited variations in both the position of the maximum intensity and the overall intensity of the photoluminescence responses as the concentration changes. Interestingly, the most concentrated suspension (4 mg/mL) showed lower

photoluminescence intensity than suspensions with lower solid loading (1, 0.5, 0.04 and 0.18 mg/mL). Additionally, the spectra of diluted suspensions presented the maximum photoluminescence intensity around 440 nm, whereas the 4 mg/mL suspension presented a red shifting of the maximum intensity to approximately 520 nm.

A study about carbon dots obtained from Microcrystalline Cellulose showed the deconvolution of a photoluminescence emission spectrum as an attempt to identify the morphological characteristics of CDs nanoparticles using photoluminescence measurements. The deconvolution showed three electronic transitions which were attributed to the recombination of carriers and trap states created at the surface of the particles, especially by protonated oxygen groups (Balanta et al., 2023). In this work, spectra of suspensions with different solid loadings were deconvoluted into four components, each with a FWHM of 58.1 nm, centered around 445, 500, 540, and 600 nm, and a minor curve representing the Raman signal of water, with a FWHM of 7.5 nm. Table 12 summarizes the relative area percentages of each emission component, derived from the deconvolution of the photoluminescence spectra.

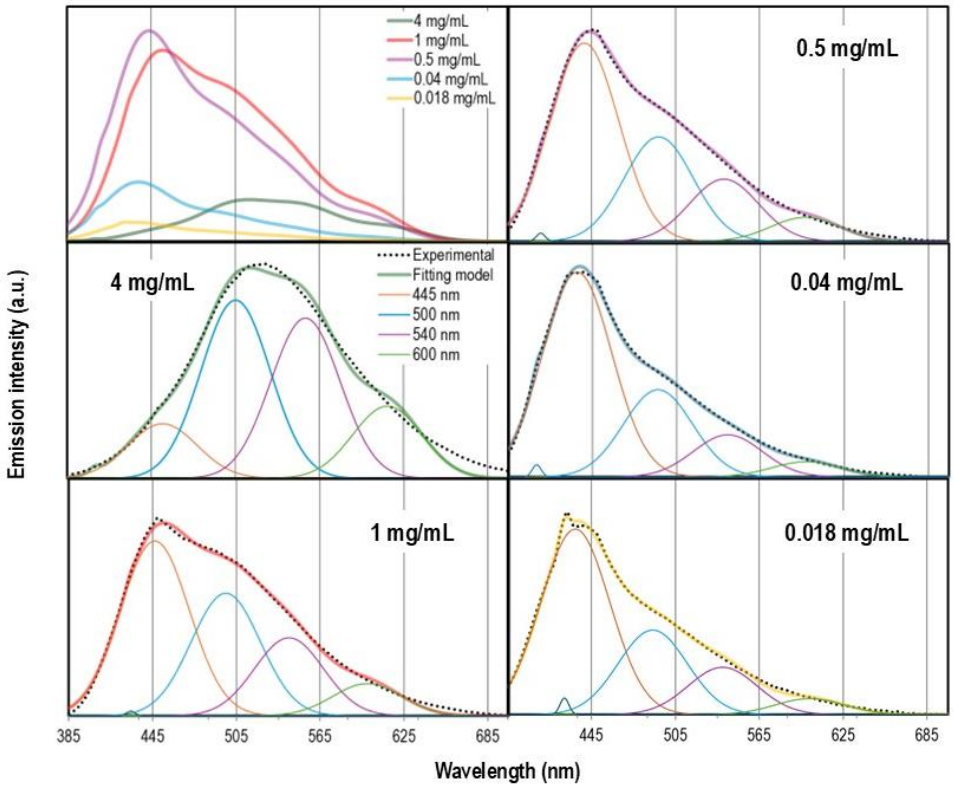

Figure 32. Deconvoluted photoluminescence emission spectra of a CDs suspension of 4, 1, 0.5, 0.04 and 0.18 mg/mL. λ_{exc}=375 nm, laser intensity=50 mW.

Table 12. Percentage of contributions of the area under the curves from the deconvolution of the photoluminescence spectra at different concentrations

	0.018 mg/mL	**0.04 mg/mL**	**0.5 mg/mL**	**1 mg/mL**	**4 mg/mL**
$\lambda_{emission}$=445 nm	55	58	51	43	12
$\lambda_{emission}$=500 nm	25	25	27	30	38
$\lambda_{emission}$=540 nm	14	12	16	19	34
$\lambda_{emission}$=600 nm	5	4	6	8	16
Water	1	0	0	0	0

Figure 33 shows the relation between the areas of the different photoluminescence contribution curves. As shown in Figure 33A, the ratio of emissions relative to the emission at 445 nm increases with the concentration of the solid loading in suspension, conversely, the ratios involving only the emissions at 500, 540, and 600 nm, excluding those that include the 445 nm emission (Figure 33B, C and D), exhibit only slight variations across the entire range of solid loading. These observations indicate that only the emission around 445 nm is notably sensitive to the concentration of the material in suspension. In contrast, the relationship between the emission contributions at 600 and 540 nm varied linearly with respect to concentration.

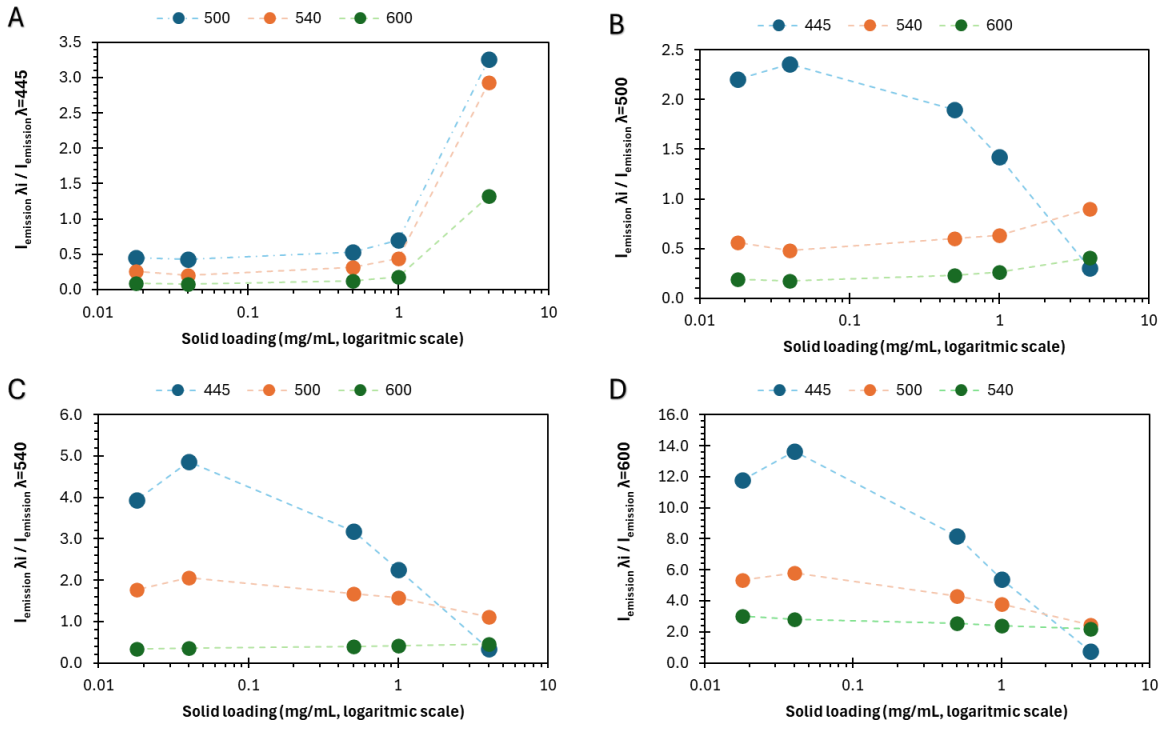

Figure 33. Indices of the ratio between the area of the different contribution emissions in relation to the contribution at (A) 445 nm, (B) 500 nm, (C) 540 nm, and (D) 600 nm with respect to the solid loading of material in suspension

The 0.5 mg/mL suspension exhibited the highest photoluminescence intensity among the evaluated samples. Therefore, this suspension was selected for further evaluation under different excitation wavelengths. Figure 34 shows the photoluminescence emission of the 0.5 mg/mL suspensions under different excitation wavelengths (300, 325, 340, 350, 375, 400, 425, 450, 470, 475, and 500 nm). As it can be seen, excitation wavelengths below 375 nm generated broad emission spectra with maximum intensity at 450 nm. The intensity of these spectra decreased as the excitation wavelength decreased. The spectrum generated with an excitation wavelength of 400 nm generated a red-shifted spectrum centered around 500 nm. Excitation wavelengths of 425 and 450 nm generate an emission around 520 nm with the highest intensity in comparison with all the spectra. The intensity of the emissions with excitation wavelengths up to 450 nm decrease as increase the excitation wavelength. Excitation wavelengths above 550 nm generate very low emission intensities. A bathochromic shift is commonly observed in carbon dots and has been associated with the presence of carbon dots with similar carbon cores but different functional groups at the surface (Gong et al., 2016; Yan et al., 2019).

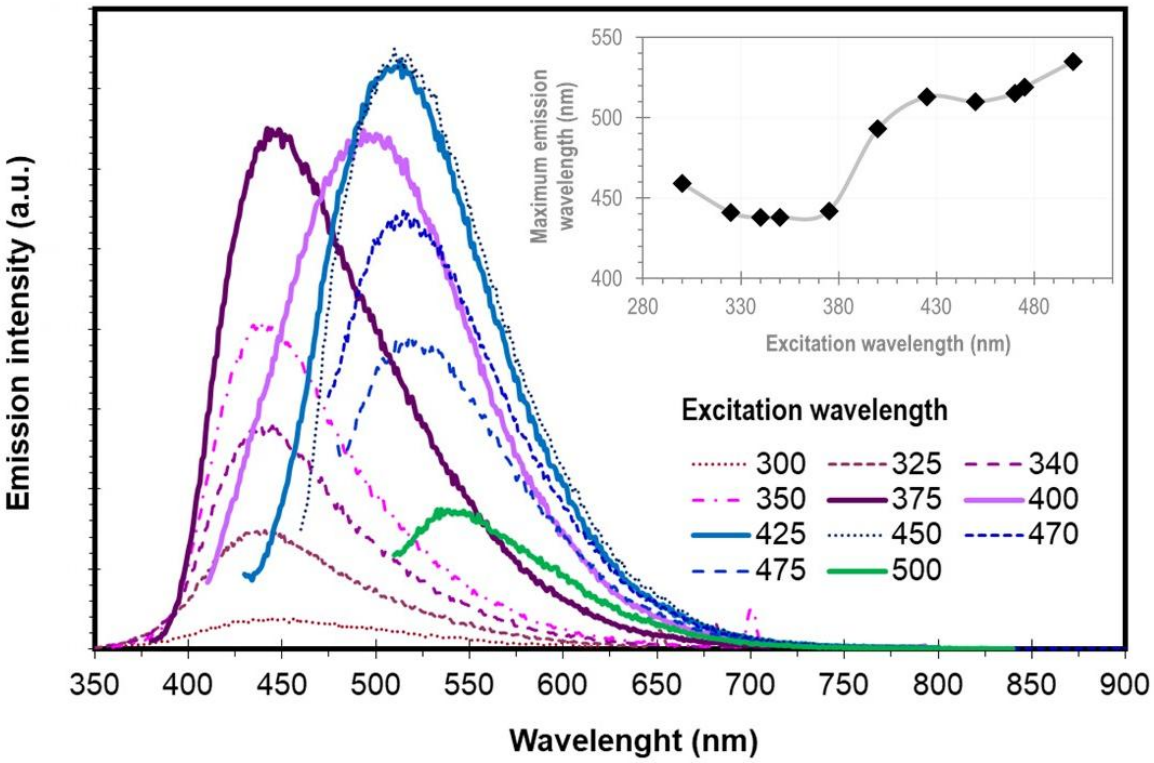

Figure 34. Photoluminescence emission spectra of a 0.5 mg/mL CD suspension recorded under various excitation wavelengths. The inset shows the relationship between the excitation wavelength and the corresponding emission maximum.

Figure 35 shows the deconvoluted photoluminescence emission spectra of the 0.5 mg/mL CDs suspension under different excitation wavelengths (375, 400, 450 and 500 nm). The deconvolution was performed using the same parameters discussed in the Figure 32. Each contribution curve possesses an FWHM of 58.1 nm.

In the spectra obtained under excitation wavelengths of 375 and 400 nm it was necessary to add an additional curve centered around 400 nm to represent the Rayleigh scattering, which is related to the water of the sample. The Raman curve was fitted with an FWHM of 7.5 in order to represent accurately the experimental

Raman curve. In the spectra obtained under excitation wavelengths of 450 and 500 nm it was not necessary to add any other curve because the Raman curve was out of the wavelength range measured.

When comparing the spectra obtained under excitation wavelengths of 375 and 400 nm is evident that the excitation wavelength of 375 nm, primarily promotes emission around 445 nm, but also generates emissions with minor intensity at 500, 540 and 600 nm. The 500 nm/445 nm ratio for the spectra under excitation wavelength of 375 nm was 0.5. In contrast, the excitation wavelength of 400 nm predominantly promotes emission around 500 nm, with a secondary emission peak around 540 nm and a slightly less intense peak at 445 nm. In this case the 500nm/445nm ratio is 1.7. It is worth noting that these experiments were executed in the same suspension, with the same pH and concentration.

When the sample is excited with 450 and 500 nm light, only the emissions at 500, 540 and 600 nm are observed. These three contributions reach their maximum photoluminescence emissions intensity when the sample is irradiated with a 450 nm light. Excitation at 500 nm resulted in a marked decrease in emission intensities.

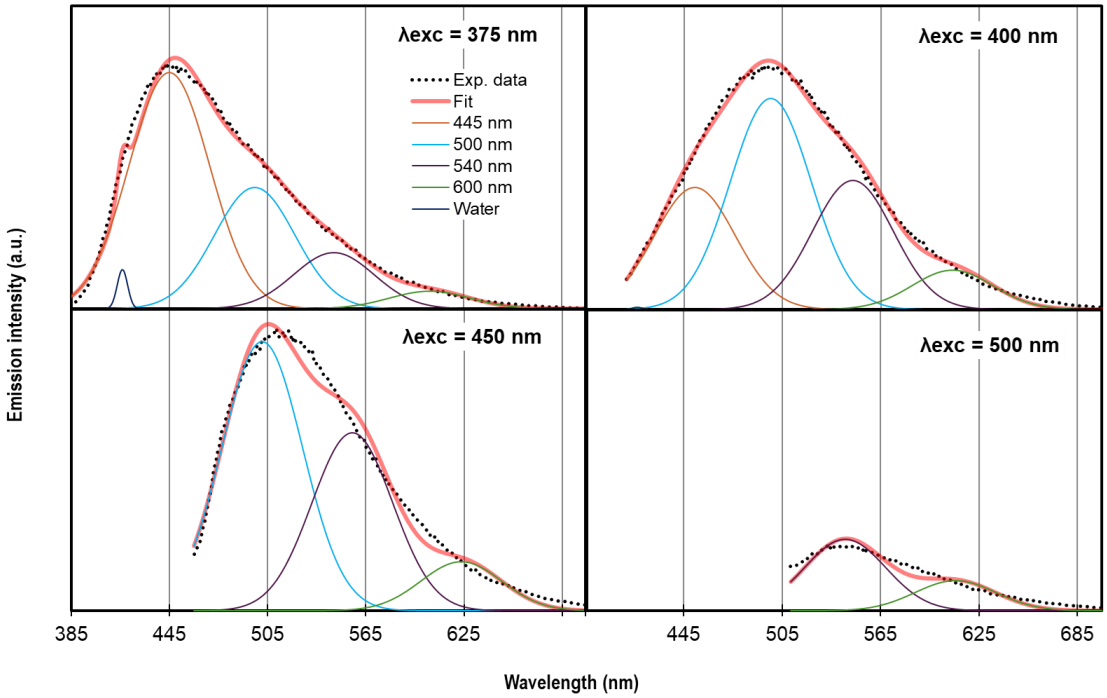

Figure 35. Deconvoluted photoluminescence emission spectra of 0.5mg/mL CDs suspension at excitation wavelengths of 375, 400, 450, and 500 nm

Table 13. Percentage (%) of contributions of the area under the curves from the deconvolution of the photoluminescence spectra collected at different emission wavelengths of the 0.5 mg/mL CDs suspension.

	λ_{exc}=375 nm	λ_{exc}=400 nm	λ_{exc}=450 nm	λ_{exc}=500 nm
$\lambda_{emission}$=445 nm	55	24		
$\lambda_{emission}$=500 nm	28	42	54	
$\lambda_{emission}$=540 nm	13	26	36	71
$\lambda_{emission}$=600 nm	4	8	10	29

To gain deeper insight into the relationship between photoluminescence emission and excitation wavelength, photoluminescence excitation spectra were examined at different emission wavelengths (Figure 36). The spectra for the 0.5 mg/mL CDs suspension shows two spectral groups. For emission wavelengths below 500 nm, the spectra showed a maximum centered around 370 nm and for emission wavelengths above 500 nm, the maximum are centered around 420-430 nm. This behavior indicates the presence of different emission centers in the material.

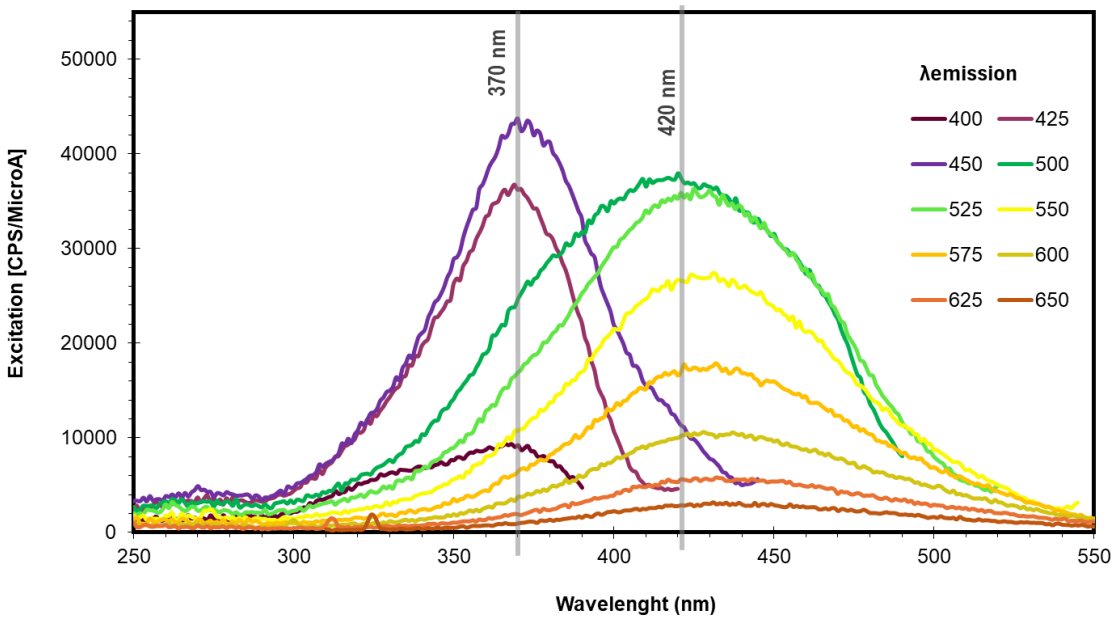

Figure 36. Photoluminescence excitation at different emission wavelengths of the 0.5 mg/mL CDs suspension.

Figure 37 shows the excitation spectra at wavelengths of 450, 500, 550, and 600 nm together with the deconvoluted photoluminescence emission spectra obtained with 375 and 450 nm excitation light, respectively. The emission spectrum obtained under

an excitation wavelength of 375 nm shows a broad peak with the maximum emission centered around 450 nm. Complementarily, the excitation spectrum collected at the wavelength emission of 450 nm shows the maximum absorption around 375 nm (Figure 37A). It is worth noting that when considering shape and intensity, the emission curve at 445 nm obtained from the deconvolution of the emission spectra satisfies the mirror-image rule with the spectrum at the wavelength emission of 450 nm better than the experimental spectra. The mirror image is a consequence of emission to higher vibrational ground states. Electronic excitation does not alter nuclear geometry, so the spacing of the vibrational energy levels of the excited states is like that of the ground state. Consequently, absorption and emission spectra are similar. The deviation from the mirror-image rule is often associated with ionization phenomena and excited state reactions different than proton dissociation, as a result, the emission spectrum is the emission derived from a formed charge-transfer complex (Lakowicz, 2010). Considering this, it could be concluded that the fundamental emission of the photoluminescence process is the one centered around 445 nm, and the emissions at 500, 540, and 600 nm are associated with other phenomena, as light re-absorption processes occurring in the suspension. These phenomena also explain the behavior of the photoluminescence emission of CDs suspensions at different solid loading, showed at Figure 32.

Likewise, Figure 37D shows the emission spectrum obtained with an excitation wavelength of 450 nm, which shows a broad peak centered around 520 nm. The emission intensities observed in the deconvolución corresponds with the intensities observed in the excitation spectra at 450 nm (Figure 37C). The deconvolution of the

emission spectrum shows that it is composed mainly of emission contributions at 500 and 540 and 600 nm.

The stokes shift is defined as the difference between excitation and emission wavelength. In the spectra showed at Figure 37, the corresponding spectra show an stoke shift of 70 nm.

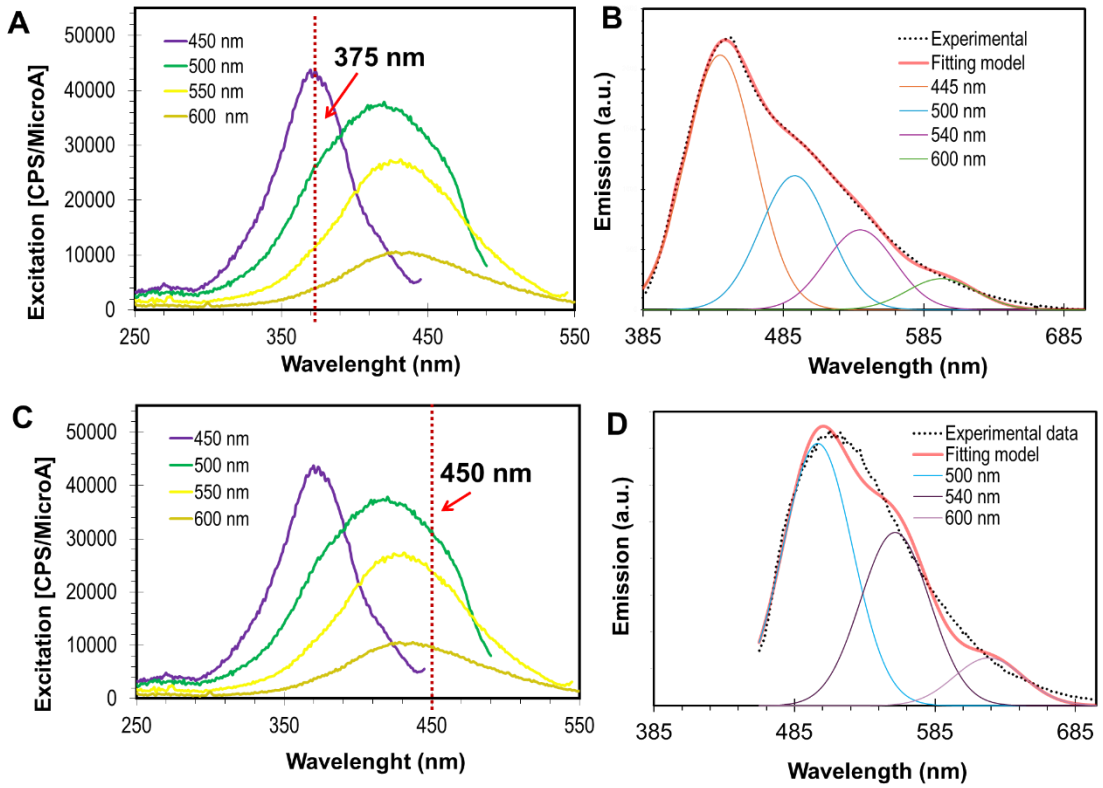

Figure 37. (A and C) Excitation spectra collected at emission wavelengths of 450, 500, 550 and 600 nm and (B and D) deconvoluted photoluminescence emission spectrum collected at excitation wavelengths of (A) 375 and (B) 450 nm, slit = 2 nm

3.3.3. Relationship between photoluminescence and agglomeration of the particles

DLS measurements indicate that diluted suspensions of CDs primarily contained particles smaller than 10 nm. However, suspensions with higher solid loading exhibited larger particles. For instance, the suspension with a concentration of 4 mg/L showed a hydrodynamic diameter distribution ranging from 20 to 500 nm (Figure 30). Particle agglomeration tendencies in suspension are associated with purification degree of the material, presence of surface states, surface chemistry of CDs, non-covalent interactions, and solid loading of the suspension. Increasing the solid loading of particles in suspension promotes proximity between them. Concentrated suspension could exhibit particle agglomeration, collisions and non-covalent interactions. As a result, the exposure of the nanoparticles to light is limited and the photoluminescent emission of concentrated suspensions is significantly lower, and phenomena of re-absorption light are promoted in comparison with more diluted suspensions. The re-absorption of light between different photoluminescence centers has been previously studied. Langer *et al.* (2023) analyzed the effect of interaction and binding modes between different functionalized polyaromatic hydrocarbons, used as a model for carbon dots, and the prototypical molecular fluorophore IPCA (5-oxo-1,2,3,5-tetrahydroimidazo-[1,2-α]-pyridine-7-carboxylic acid) under different interaction modes on deactivation pathways, electronic transitions and communication between photoluminescence centers. They found that deactivation pathways typically involve multiple charge and energy transfer events that can promote the formation of charge separated states and lead to the activation of other PL centers in carbon dots. According to the study, carbon dots

and their attached functional groups can act as electron donors or acceptors, in function on the arrangement, the doping pattern and surface functionalization.

To explain the origin of the photoluminescence of carbon dots, Langer *et al*., relate the emission with three sources: core states due to carbon sp^2 domains, surface states stemming from surface chemical groups, and molecular states due to the presence of fluorophores. Also, they found that fluorophores typically exhibit photoluminescent emission around 430-450 nm, while core or surface oxo-functionalized polyaromatic hydrocarbons exhibit emission around 500-550 nm (Langer et al., 2023). Interestingly, the deconvoluted photoluminescence emission spectra presented in this work, with contributions at 445, 500, 540 and 600 nm, are consistent with the theoretical study by Langer *et al*. Furthermore, the characterization of the CDs presented in Chapter 2, along with previous experimental studies on the photoluminescence emission of various organic molecules, aligns with the observations reported by Langer *et al*., and supports the association of specific emission contributions with the presence of distinct functional groups, as illustrated in Figure 38.

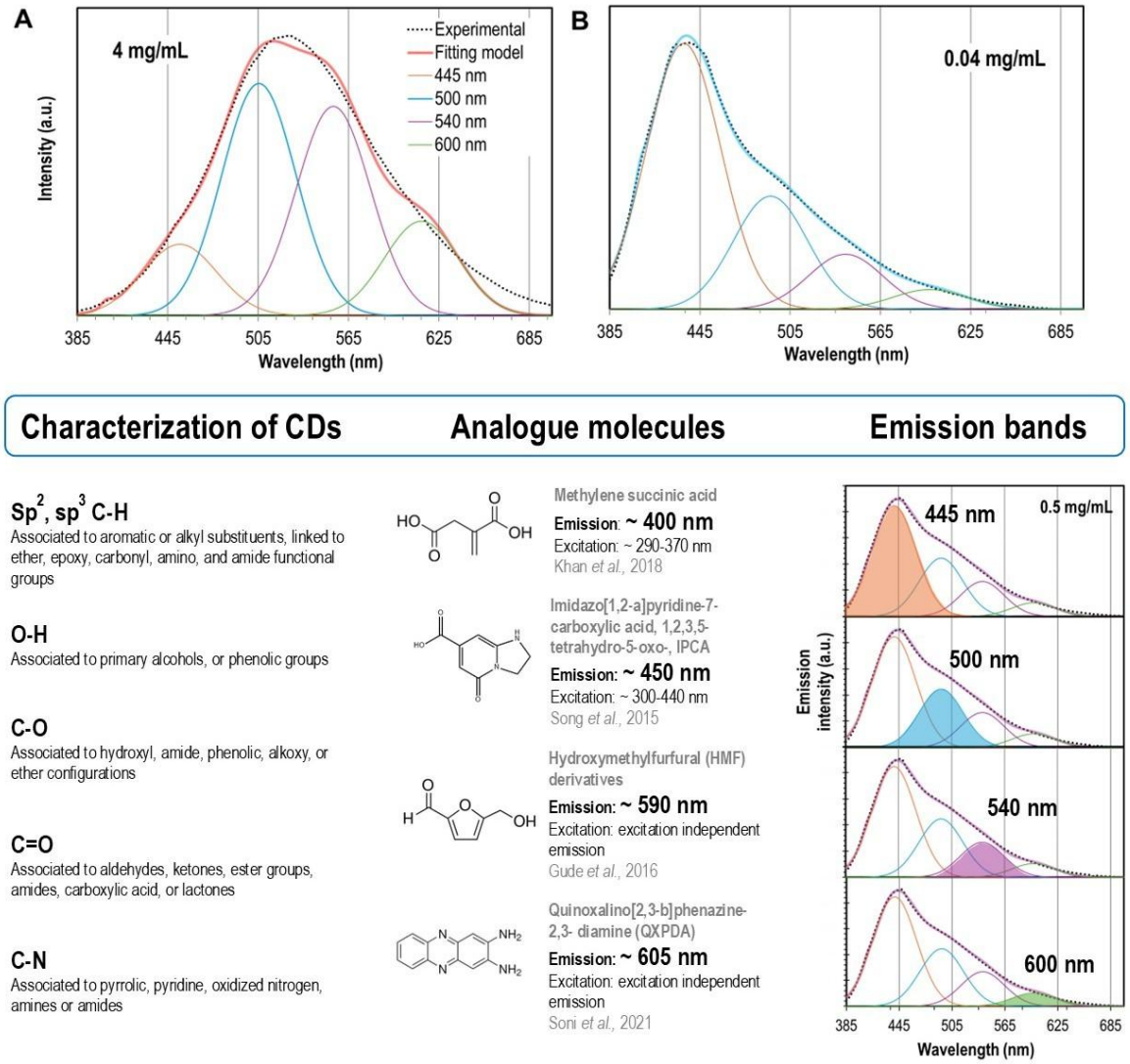

Figure 38. (A,B) Example of spectral emission of carbon dots at 4 and 0.5 mg/ml; (C) Relationship between the functional groups identified during the characterization of purified CDs and their respective contributions to photoluminescence, interpreted through analogous fluorescent organic molecules.

As an approach to analyze the different photoluminescence centers of the CDs in suspensions with different concentrations were analyzed. It is worth mentioning that in diluted suspensions, particles are mostly dispersed, therefore, there is less proximity between them and fewer re-absorption of light between the particles. Therefore, the exposure of different photoluminescence centers to light is higher than in highly concentrated suspensions, as can be observed at Figure 39.

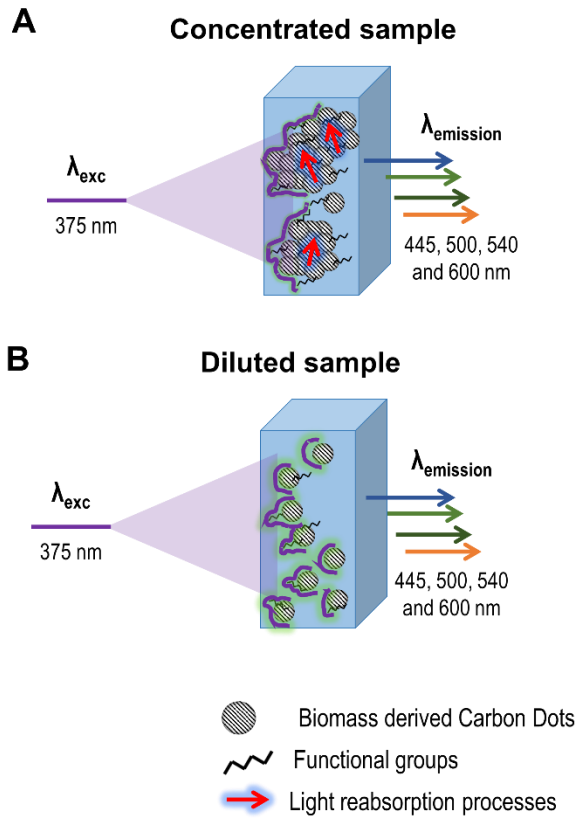

Figure 39. Exposition of Carbon Dots in concentrated and diluted aqueous suspensions

Figure 40 summarize the relationship between the concentration of material in suspension and the deconvoluted photoluminescence emission spectra. In the case of a concentrated suspension (4 mg/mL), the main contribution to the overall photoluminescence spectrum corresponds to the peak at 500 nm. The emission intensity at 500 nm was 3.3 times higher than the one at 445 nm. Nevertheless, this spectrum showed a much lower overall emission compared to the less concentrated sample at 1 mg/mL, as can be observed in Figure 32. The low emission intensity of the concentrated sample is attributed to the limited exposure of the photoluminescent centers of CDs and molecular states to light, caused by the saturation of the suspension, and energy loss resulting from the re-absorption of light events.

The suspension with a solid loading of 1 mg/mL showed the highest emission intensity in comparison to the 4 and 0.18 mg/mL suspensions. In this case, the major contribution to the overall photoluminescence spectrum corresponds to the peak at 445 nm. Also, the overall spectrum showed a broad shape due to the high intensity of the peaks at 500, 540 and 600 nm.

The emissions at 500 and 445 nm are related to core or surface oxo-functionalized polyaromatic hydrocarbons and molecular fluorophores, respectively. The ratio between the peaks at 500 and 445 nm (500nm/445nm) is 0.7, which indicates that a higher quantity of photoluminescent centers that emit at 445 nm are exposed to light in comparison with the concentrated sample. In this case, the emission peak at 500 nm also shows a high intensity. The high intensity of the emission at 500 nm is

attributed to reabsorbing of light phenomena occurring simultaneously in the suspension. Part of the emission generated at 445 nm could be re-absorbed by other photoluminescence centers in the CDs. Consecutively, the CDs emit light at 500, 540 and 600 nm, causing the broad shape of the spectrum.

The most diluted suspension (0.018 mg/mL) exhibited a low overall emission due to the low quantity of photoactive material in suspension, as can be observed in Figure 32. In this case the highest contribution to the overall photoluminescent emission spectrum comes from the 445 nm emission. The 500nm/445nm ratio is 0.5, indicating that at these conditions there are even less re-absorption of light events compared to the 4 and 1 mg/mL suspensions.

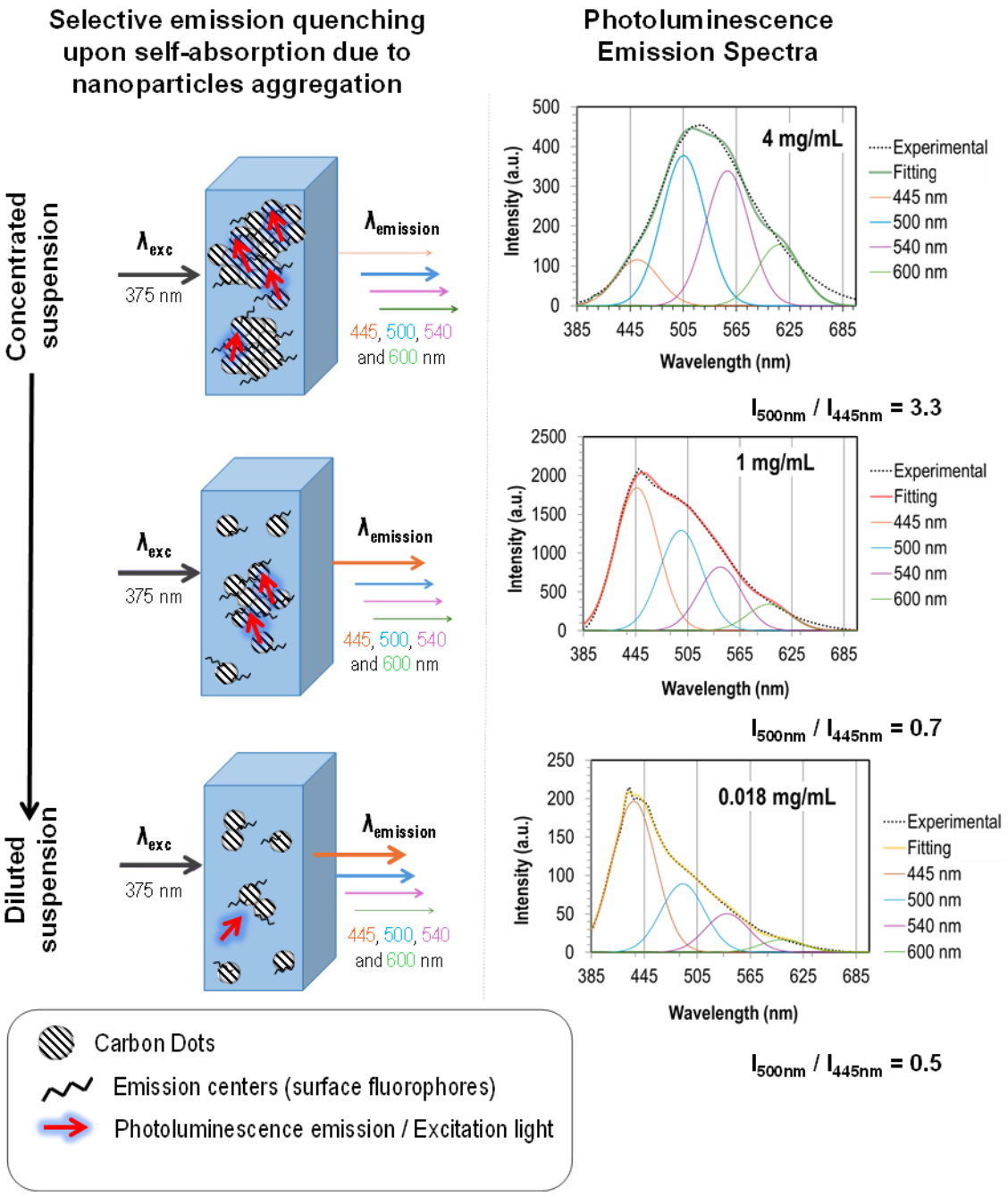

Figure 40. Schematic representation of the different contributions of emission in the prepared carbon dots, and the re-absorption effects of those emission contributions upon the concentration of carbon dot in the suspensions. Thick lines represent predominant emission contributions.

3.4. Summary

- Analysis of saturated orange peel-derived CDs suspensions generate low-intensity red-shifted emissions, while diluted suspensions generate intense emissions around 450 nm when excited with a 375 nm light. The photoluminescence analyses helped to infer the reabsorption of light processes occurring in suspensions due to the agglomeration of particles. For instance, photoluminescence emission around 445 nm reaches maximum intensity at a concentration of 0.5 mg/mL, when CDs nanoparticles are isolated. The observations derived from this study emphasize the importance of material concentration as a critical parameter in CDs applications.
- UV-vis analysis showed that the highest absorption of light occurs in the ultraviolet region (~375 nm).
- The excitation spectra of the suspension at 0.05 mg/mL under different excitation or emission wavelengths, in general, showed two main spectral groups attributed to different photoluminescence centers. Based on this, the deconvolution of some photoluminescence spectra at different conditions was elaborated.
- The deconvolution of emission spectra at different concentrations revealed four contributions to the full emission at 445, 500, 520, and 600 nm, which have been associated mainly with functional groups at the surface of CDs and core and surface oxygenated polyaromatic molecules. All this helped to explain the origin of the wide range of photoluminescence absorption and emission of CDs.

— When CDs suspensions are excited at 375 nm, the blue emission (~445 nm) is the most significant, but if the same suspension is excited with wavelengths longer than 400 nm, the green emission (~520 nm) becomes the most intense. When the suspension was excited with wavelengths longer than 500 nm, the resulting emission was of low intensity. The red shifting observed in the photoluminescence of CDs suspensions is attributed to the presence of different photoluminescence centers with different bandgaps and the occurrence of simultaneous reabsorption of light processes between them.

Chapter 4

Carbon Dots applied in Third Generation Solar Cells

Chapter 4: Carbon Dots applied in Third Generation Solar Cells

4.1. Introduction

The CDs characterized in the first chapter of this document were used to sensitize FTO-TiO_2 photoanodes for third-generation solar cells via dip-coating. The suspensions used for sensitization were prepared from materials purified in steps 1: 0.22 µm, 4: 50 kDa, and 5: 5 kDa: a concentration of 0.25 mg/mL was used with the aim of evaluating the effect of purification of the material in its performance as sensitizer. Additionally, the most purified material (Step 5: 5kDa) was evaluated at concentrations of 0.05, 0.25 and 0.5 mg/mL to evaluate the effect of the concentration of material on the photoanode surface.

4.2. Materials and methods

4.2.1. Synthesis and purification of CDs

Orange peel was collected from a local market in San Luis Potosi, Mexico, dried, and pulverized. The orange peel powder was washed with 1 M HCl solution for 24 hours and rinsed with deionized water until reaching a pH of four and left to dry at

90°C to obtain a powder. 100 mg of this powder was suspended in 15 mL of deionized water and placed in a microwave oven (Nanowave 400 Anton Paar GmbH) at 220 °C for 30 minutes for a microwave-assisted hydrothermal synthesis. The as-obtained suspension was sequentially filtrated with a Sterile Millex filter of 0.22 µm, a Durapore membrane of 0.1 µm, and with Spectrum MicroKros TC Hollow Fiber Filters with molecular weight cut-offs of 100, 50, and 5 kDa to remove synthesis by-products.

4.2.2. Assembling of third generation solar cells

Figure 41 shows the components used to construct the solar cell. The semiconductor film of the photoanodes was elaborated with 0.5 g of TiO_2 Degussa (Evonik) P25 powder, which was mixed with 4 g of α-terpineol, and 0.15 g of ethyl-cellulose as binders in 4 ml of ethanol and 4 ml of acetone, under constant stirring at 73 °C for 2 hours to form a paste (Matos et al., 2013). Nine layers of TiO_2 paste were deposited onto the conducting glass sheet of FTO by the Doctor Blade method. Then the FTO-TiO_2 substrates were calcined at 450 °C for 3 hours. The active area of photoanode was 0.5 cm^2.

The FTO–TiO_2 electrodes were dip-coated with CD suspensions of fixed concentration (0.25 mg/mL) at different purification degrees (purification steps 1:0.22 µm, 4:50 kDa, and 5:5 kDa), as well as with purified CDs at different concentrations (0.05, 0.25 and 0.5 mg/mL). All suspensions were adjusted to a pH around 7 because based on potentiometric titration data, this pH value facilitates electrostatic interactions between the TiO_2 surface and CDs.

The dip-coating procedure was conducted at room temperature for 24 hours. After that, the electrodes were dried at room temperature and assembled into the cell.

To assemble the solar cell, an FTO substrate coated with a platinum film was placed above the photoanode. The two glasses were clipped together with cyanoacrylate adhesive. The electrolyte employed was Iodolyte HI-30 from Solaronix, based on the I^-/I_3 redox pair, which was injected into the assembled cell and sealed to prevent leaking. A colloidal silver spot was applied to the upper surface of the conductor side of the FTO glass to enhance conductivity between the solar cell electrodes and the connections of the solar simulator (Figure 41).

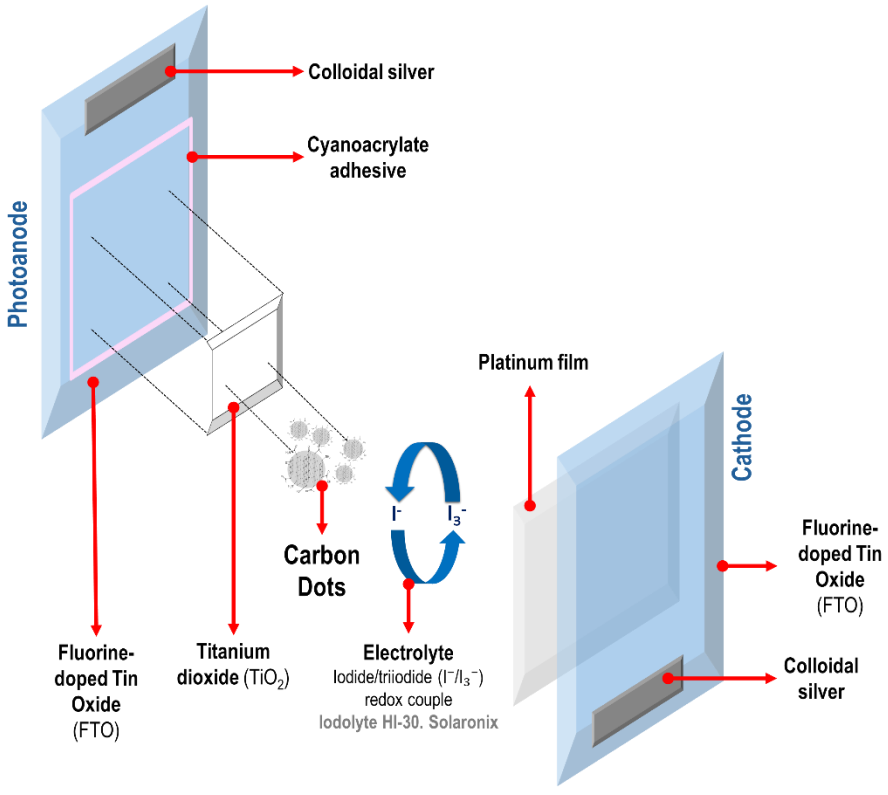

Figure 41. Diagram of the components assembled to construct the CD-sensitized solar cell

4.2.3. Determination of solar cell parameters

I–V curves were obtained by using a solar simulator under an irradiation intensity of 1000 $W \cdot m^{-2}$. The values of open-circuit voltage (V_{OC}) and short-circuit current (I_{SC}) were obtained directly from the I-V curves. The fill factor (FF) of the solar cells was calculated using the following equation:

$$FF = \frac{P_{max}}{P_T} = \frac{I_{max}V_{max}}{I_{SC}V_{OC}}$$

Where P_{max} is the maximum potential observed in the experimental curves and is obtained multiplying the maximum recorded current (I_{max}) by the maximum recorded potential (V_{max}). P_T is the theoretical maximum potential in the cell, which can be obtained by multiplying V_{OC} by I_{SC}. The cell efficiency (η) was calculated using the following equation:

$$\eta = \frac{I_{SC}V_{OC}FF}{P_{in}} = \frac{P_{max}}{P_{in}}$$

Where P_{in} is the incident input potential in the solar simulator, which conventionally corresponds to a value of 1000 W/m^2.

4.3. Results and discussions

4.3.1. Sensitization of solar cells

The electron transfer mechanisms involved in the photogeneration of charge in CDs-Sensitized Solar Cells can be described as the interaction between the conduction band of TiO_2 and the Lowest Unoccupied Molecular Orbital (LUMO) of CDs.

According to the literature, TiO_2 possesses energy levels of approximately −4.0 eV and −7.2 eV for the conduction and valence bands, respectively (Amancio et al., 2025). Therefore, the LUMO of the CDs should be positioned above the conduction band edge of TiO_2, that is, above −4.0 eV.

The current generation starts with the photoexcitation of an electron of the CDs from the Highest Occupied Molecular Orbital (HOMO) to the LUMO level. The alignment of the bands or molecular orbitals of the components in direct contact during the charge transfer process generates a favorable driving force for efficient charge injection, for example, an efficient injection from the LUMO of CDs into the conduction band of TiO_2. Once injected, the electrons migrate toward the counter electrode, while the positive holes generated during this process are subsequently neutralized by electrons from the redox pair in the electrolyte (Amancio et al., 2025).

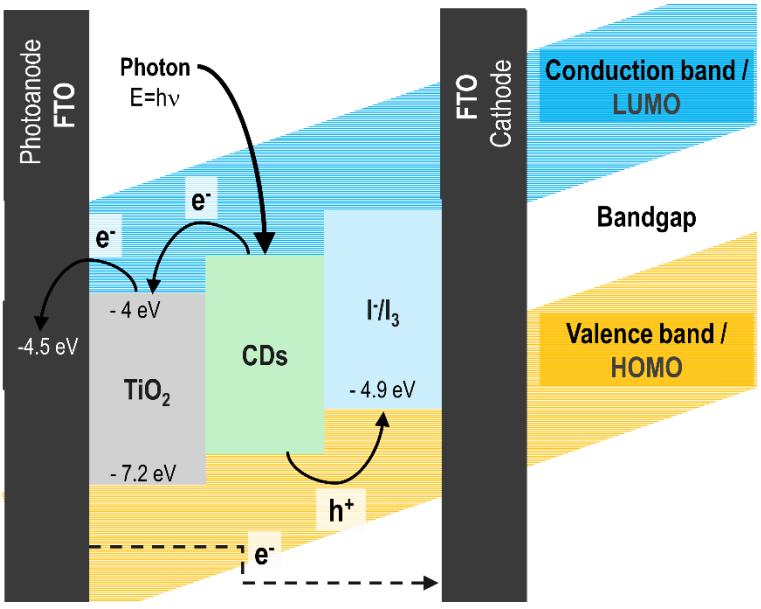

Figure 42. Electron Transfer Mechanisms in CDs-Sensitized Solar Cells

The capability of the materials to act as a sensitizer for solar cells was confirmed, since the CDs-sensitized solar cells showed higher efficiency values in comparison with the solar cell without sensitization (Figure 43, Table 14). The solar cell parameters from experiments conducted with materials at different purification degrees showed that as the purification degree of the samples increases, the efficiency of the solar cell also increases. On average, the step 1: 0.22 μm material showed a decrease of approximately 19% compared to the pristine cell, while the materials from step 4: 50 kDa and Step 5: 5 kDa showed an efficiency increase of 6%. The highest value recorded in this group of experiments, corresponding to the step 5: 5kDa material, which showed an efficiency increase of 26% compared to the pristine cell.

The increase of the efficiency of the solar cells correlates with the remotion of synthesis-derived byproducts in the sensitizer material, which emphasizes the importance of adequate material purification to ensure an optimal functionality of CDs in their applications.

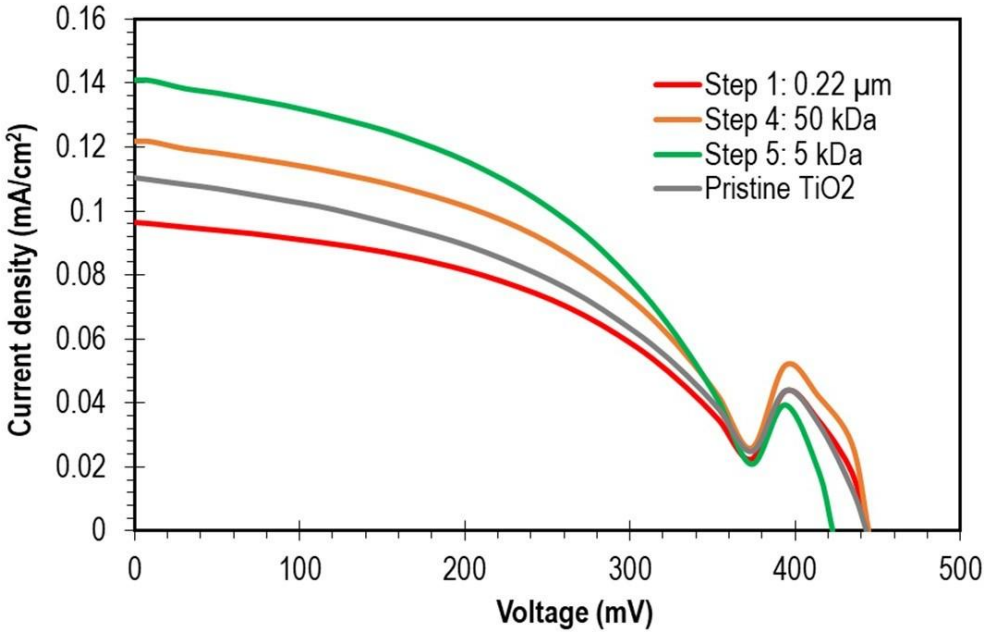

Figure 43. I-V curves of solar cells sensitized with the materials from step 1:0.22 µm, step 4:50 kDa and step 5:5 kDa (ca. 0.25 mg/mL)

Table 14. Parameters of solar cells sensitized with the materials from step 1:0.22 µm, step 4:50 kDa and step 5:5 kDa. The concentration of the suspensions for dip-coating was 0.25 mg/mL.

Electrode conditions	Open Circuit Voltage (mV)	Short Circuit Current (mA/cm^2)	Fill Factor	Solar Cell Efficiency (%)
Pristine TiO_2	452	0.111	39	0.020
Step 1: 0.22µm	417 ± 35	0.093 ± 0.006	41 ± 1	0.016 ± 0.002
Step 4: 50 kDa	433 ± 30	0.12 ± 0.01	42 ± 2	0.021 ± 0.001
Step 5: 5kDa	407 ± 27	0.13 ± 0.02	40 ± 1	0.21 ± 0.004

Analysis of each solar cell parameter in relation to the number of membranes used during the purification of CDs showed that the efficiency of the solar cell exhibited

an increase at the final two purification steps. Notably, a decrease in efficiency was observed when CDs purified with only one membrane were incorporated into the photoanode (Figure 44A). On the other hand, the open-circuit voltage decreases in all cases compared to the pristine FTO–TiO_2 photoanode (Figure 44B). The fill factor increases with the addition of CDs regardless of the number of purification steps applied (Figure 44C). Additionally, the analysis revealed a linear correlation between the short-circuit current and the number of membranes, with a coefficient of determination (R^2) of 0.9994 (Figure 44D).

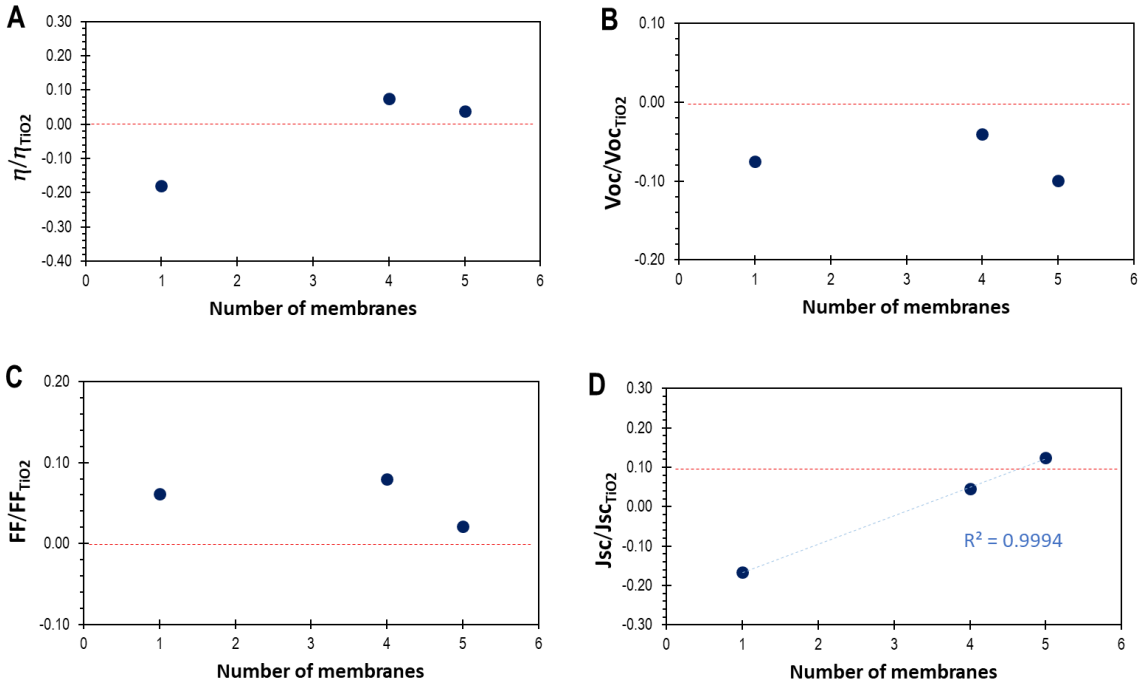

Figure 44. Solar cell parameters normalized with respect to the reference device using a photoanode composed of FTO–TiO_2 without CDs: (A) solar cell efficiency, (B) open circuit voltage, (C) fill factor, and (D) short circuit current. The average data are presented as a function of the number of membranes used during the purification of the CDs

On the other hand, solar cells sensitized with the material at the purification step 5: 5 kDa and different concentrations (Figure 45, Table 15), showed that increasing the concentration of material in suspension during the dip-coating of the photoanode, leads to an increase in the efficiency achieved by the solar cell. The highest concentration measured (0.5 mg/mL) yielded the highest efficiency value in comparison with the rest of the experiments (0.03%), showing an increase of 15% compared to pristine FTO-TiO_2 electrodes. The highest value recorded in this group of experiments, corresponding to the 0.5 mg/mL step 5: 5kDa suspension, showed an efficiency increase of 42% compared to the pristine cell, nevertheless, further studies are required to enhance the performance of solar cells sensitized with CDs to facilitate their implementation on a larger scale.

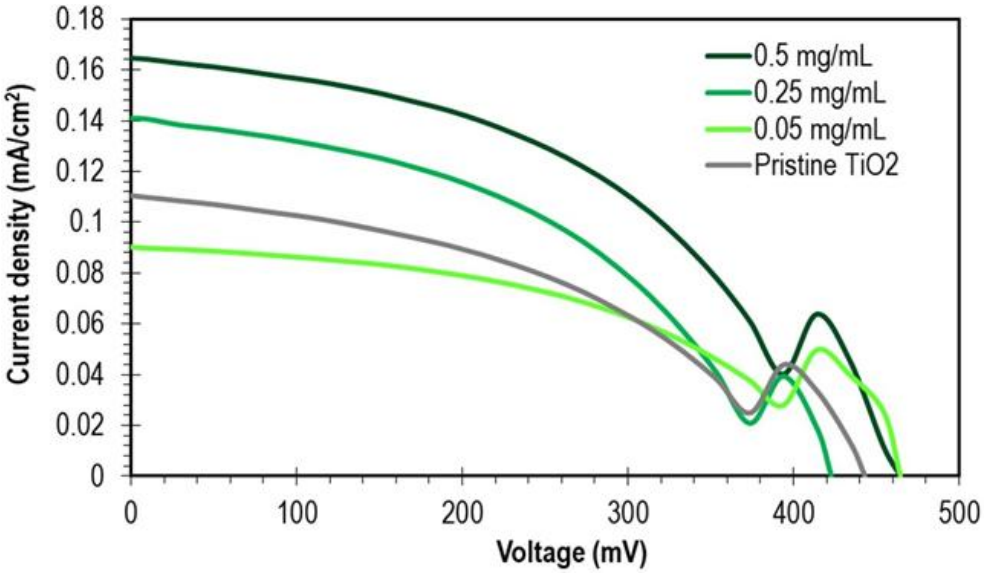

Figure 45. I-V curves of solar cells sensitized with the sample obtained from the purification step 5:5 kDa at different concentrations.

Table 15. Parameters of solar cells sensitized with the sample obtained from the purification step 5:5 kDa at different concentrations during the dip-coating.

Electrode conditions	Open Circuit Voltage (mV)	Short Circuit Current (mA/cm^2)	Fill Factor	Solar Cell Efficiency (%)
Pristine TiO_2	452	0.111	39	0.020
TiO_2 + CDs 0.05 mg/mL	456 ± 17	0.08 ± 0.01	42 ± 3	0.017 ± 0.003
TiO_2 + CDs 0.25 mg/mL	407 ± 27	0.12 ± 0.02	40 ± 1	0.021 ± 0.004
TiO_2 +CDs 0.5 mg/mL	436 ± 23	0.13 ± 0.02	40 ± 2	0.023 ± 0.005

In this case, the analysis of each solar cell parameter in relation to the concentration of the CD suspensions used for dip-coating during photoanode preparation revealed a linear correlation with the cell efficiency, with a R^2 of 0.976 (Figure 46A).

The open-circuit voltage showed a slight improvement at this lowest concentration but decreased at higher concentrations compared to the pristine FTO–TiO_2 photoanode (Figure 46B). Also, as observed previously, the fill factor of the solar cells increased with the addition of CDs, with a slightly greater enhancement at 0.05 mg/mL, the lowest concentration analyzed (Figure 46C). Conversely, the short-circuit current showed a slight increase as the concentration of the CD suspension increased (Figure 46D).

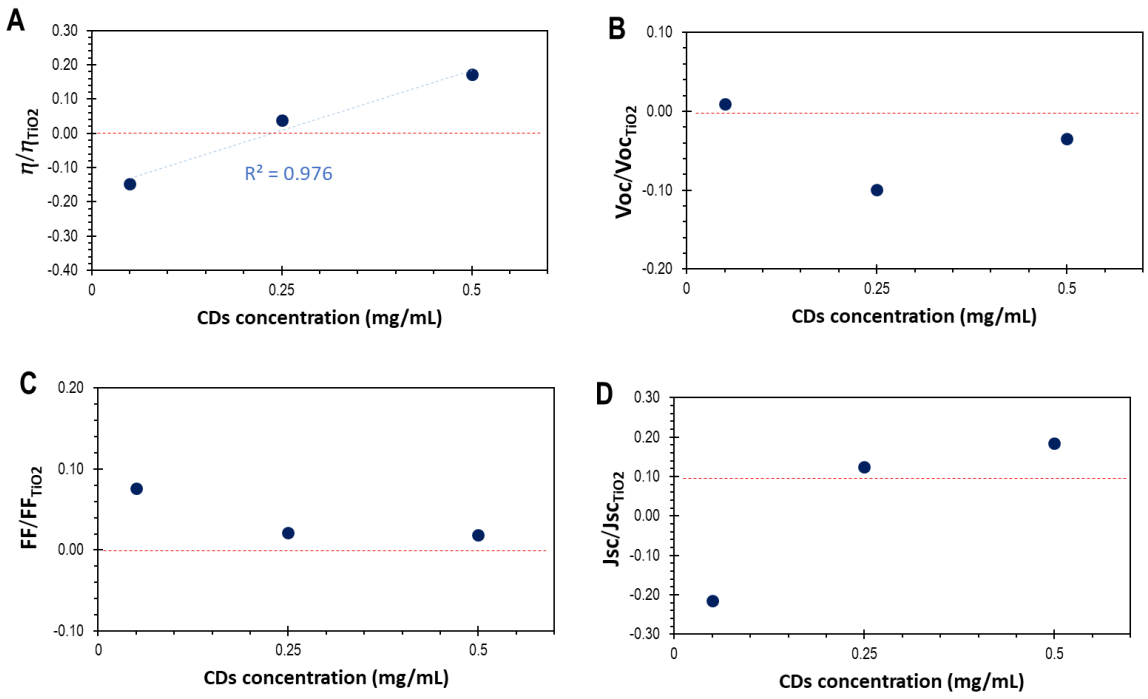

Figure 46. Solar cell parameters normalized with respect to the reference device using a photoanode composed of FTO–TiO_2 without CDs: (A) solar cell efficiency, (B) open circuit voltage, (C) fill factor, and (D) short circuit current. The average data are presented as a function of the concentration of the suspension of CDs used to sensibilize the photoanode through dip-coating (mg/mL)

Table 16 compares the best results obtained in this work with those reported in similar studies in which TiO_2-CDs were employed as photoanodes.

It can be noted that, although efficiency values of up to 11.9% have been reported in the literature for third generation sensitized solar cells (as shown in Table 2), the use of biomass derived CDs as sensitizers or co-sensitizers of solar cells remains a promising alternative for the development of such devices. Furthermore, adding additional elements to the cell, for example a natural dye as reported by Amancio *et al.*, could further enhance the effect produced by CDs.

Table 16. Comparison between the best parameters obtained and those reported in similar studies (TiO2 +CDs photoanodes)

Electrode conditions	Open Circuit Voltage (mV)	Short Circuit Current (mA/cm^2)	Fill Factor	Solar Cell Efficiency (%)	Reference
Orange peel derived CDs, 0.5 mg/mL	474.74	0.16	42.56	0.03	This work
Strawberry powder + $NH_3 \cdot H_2O$ derived CDs	380	0.226	44	0.04	(Zhao et al., 2018)
Sodium citrate and urea derived CDs	490	0.089	22	0.1	(Ghann et al., 2019)
Pixirica fruit (*L. australis*) derived dye and CDs	343 ± 13	0.373 ± 0.01	60 ± 2	0.10 ± 0.02	(Amancio et al., 2025)

4.4. Summary

- The performance of solar cells sensitized with orange peel derived CDs was analyzed. The evaluated variables were the effect of the purification of the CDs and the effect of the concentration of the suspension used for dip-coating the FTO-TiO_2 photoanodes.
- The short circuit current of the solar cell showed a linear correlation with respect to the number of membranes employed during the purification of the CDs. On the other hand, the efficiency of the cell showed a linear correlation with respect to the concentration of the suspension used for dip-coating the photoanodes
- In all the cases, the fill factor of the cells increased with the addition of CDs to the FTO–TiO_2 photoanode.
- The highest concentration (0.5 mg/mL) and the most purified material yielded the highest efficiency value in comparison with the rest of the experiments.

The highest value recorded showed an efficiency increase of 42% compared to the pristine cell.

- Further studies are required to enhance the performance of solar cells sensitized with CDs to facilitate their implementation on a larger scale.

Chapter 5

Conclusions, perspectives, and scientific products

Chapter 5: Conclusions, perspectives, and scientific products

5.1. Conclusions

The generation of biomass-derived CDs was deeply studied on this thesis. Initially, the degradation of biomass was analyzed through a literature review and by characterizing the orange peel and the orange peel fraction used in the synthesis, which was mainly composed of lignin and cellulose. This aimed to infer the negative effects of the presence of synthesis by-products. The membranes used in the sequential purification of CDs were selected based on the expected synthesis by-products.

Carbonous materials with different purifications levels, but obtained following the same synthesis protocol, were characterized to analyze the chemical structure of the photoluminescent nanoparticles and the influence of by-products and molecular fluorophores present in suspension with them. TPD-MS analyses confirmed the presence of organic molecular fragments and demonstrated the effectiveness of

membrane separation as a purification method. The most purified samples exhibited lower quantity of molecular fragments in some m/z profiles, such as m/z=110 and m/z=53, associated to 1,2-bencenediol and fragments of the decomposition of 2-hydroxyphenol, respectively. The most purified sample (step 5:5 kDa) showed less biomass derived by-products according to the m/z profiles. DLS analyses highlighted the impact of purification in the eventual formation of large particle aggregates.

UV-vis and photoluminescence spectroscopy showed that only a small fraction of light absorbing species was removed during the purification steps, pointing out that the CDs matrix were the main species responsible for the observed optical features. Differences in absorbance and photoluminescence emission intensity among samples with similar solid loadings but different purification levels showed that the presence of by-products in suspension affects the optical response of the samples. These observations highlight the importance of a proper and well-designed purification process to avoid biases in interpreting optical responses and to prevent misinterpretations in photoluminescent-based applications of biomass derived CDs.

For the most purified sample (Step 5:5 kDa), transmission electron microscopy allowed the visualization of nanoparticles with a spherical shape with a diameter of 3.4 ± 0.9 nm and an interplanar distance of 0.22 nm, attributed to the (1 0 0) plane of graphite carbon. In general, HR-TEM, FTIR, XPS, Raman spectroscopy, potentiometric titration and NMR suggested that the material was composed by sp^2 and sp^3-hybridized carbon, decorated with carboxylic acids, aldehydes, ketones, ether, epoxy, alkoxy, amino, and amide functional groups. The functional groups detected during characterization were attributed to those located on the core or

surface of the spherical CDs nanoparticles, which contribute to its photoluminescence emission.

To thoroughly analyze the photoluminescent behavior of the most purified material (Step 5:5kDa), photoluminescence emission and absorption of suspensions with varying material loadings were measured under different excitation wavelengths. These observations were further examined through deconvolution analysis. Deconvolutions of photoluminescence emission spectra under different conditions helped infer reabsorption of light processes among particles in suspensions influenced by interparticle interactions. Interparticle electrostatic, non-covalent, and steric interactions between molecular states and CDs in aqueous suspensions, such as dipole-dipole, π- π stacking and van del Waals forces, may be promoted by the presence of various functional groups on the particles, increased solid loading, and agglomeration of particles in suspension. Additionally, the deconvolution results revealed photoluminescent contributions at 445, 500, 540, and 600 nm, which are consistent with previous theoretical studies that analyzed the photoluminescence of CDs model structures. This study enabled the assignment of emission contributions to functional groups and carbon structures, clearly demonstrating the role of different photoluminescence centers in the material. The systematic analytical approach used to identify relationships between the molecular structure of the material and its photoluminescent response helped to elucidate the complex mechanisms involved in CDs photoluminescence.

Finally, the analysis of the generated materials as sensitizers of TiO_2-FTO photoanodes used in third-generation solar cells demonstrated that the performance

of the cells is affected by the purification level and quantity of material used; the short circuit current of the solar cell showed a linear correlation with respect to the number of membranes employed during the purification of the CDs, and the efficiency of the cell showed a linear correlation with respect to the concentration of the suspension used for dip-coating the photoanode.

5.2. Perspectives

The analysis presented in this thesis showed that the product of the synthesis of CDs from biomass waste resulted in a complex colloidal system with multiple interaction occurring simultaneously. Considering that CDs are highly functionalized nanoparticles, it is suggested to analyze the packing and agglomeration tendencies of the particles when they are decorated with different functionalities. The functionalization of CDs with different functional groups could help to develop and enhance different applications of these nanoparticles, like photocatalysis and drug delivery.

Additionally, enhancing the performance of solar cells synthetized with CDs is necessary to facilitate their larger scale implementation. To achieve this, it is essential to study the cell parameters, and certain aspects of photoanode preparation, like (i) porosity and crystallization degree of the TiO_2, (ii) thickness of TiO_2 layers on the FTO surface of the photoanode, and (iii) concentration of the CDs suspension to sensitize the photoanode via dip coating.

The results presented in chapter 4 indicate a trend of increasing efficiency with the concentration of CDs in the suspension used to sensitize the photoanode via dip-coating, with the highest efficiency value that could be achieved with a more concentrated CDs suspension, which was not reached in these experiments. Moreover, it is recommended to explore alternative methods, beyond dip-coating, for preparing the CDs-TiO_2 photoanodes, for instance, synthesizing a CDs-TiO_2

composite via thermal methods prior to the deposition of the semiconductor on the FTO or FTO substrate.

Further research is needed to explore the potential of chemical reduction CDs to modify their properties. From a future perspective, the impact of the reduction of CDs on solar cell performance will be investigated. The reduction of the materials has already been completed, as demonstrated in Appendix 1 of this document, providing a foundation for subsequent device fabrication and performance evaluation. Moreover, considering that the thermal process volatilizes functional groups responsible for fluorescence, analyzing both photoluminescence emission and colloidal behavior of reduced CDs could further enrich the understanding of their photoluminescence properties in suspension.

5.3. Scientific publications

1. Gonzalez-Vera, A. S., Pineda-Arellano, C. A., Ramírez-Monroy, A., Matos, J., Chazaro-Ruiz, L. F., Rangel-Mendez, J. R., & Ania, C. O. (2025). *Influence of the sequential purification of biomass-derived carbon dots on their colloidal and optical properties.* Carbon Trends, 19, 100460. https://doi.org/10.1016/j.cartre.2025.100460
2. Gonzalez-Vera, A.S., Perrin, G., Botsoa, J., Ntsoenzok, E., Chazaro-Ruiz L.F., Rangel-Mendez, & R., Ania, C. (2025) *Analyzing photoluminescence emission quenching effects in colloidal suspensions of carbon dots.* Colloids and Surfaces A: Physicochemical and Engineering Aspects. ***Submitted.***

5.4. Conferences and symposia

1. Gonzalez-Vera, A.S., Ania, C., Pineda-Arellano, C.A., Ramírez-Monroy, A., Matos, J., Chazaro-Ruiz, L.F., Rangel-Mendez, R. *Effect of precursor composition and purification process in the properties of Carbon Quantum Dots synthetized from orange peel.* Oral presentation. The World Conference on Carbon 2023. Cancún, México.
2. Gonzalez-Vera, A.S., Ania, C., Amaterz, H., Botsoa, J., Ntsoezok, E., Chazaro-Ruiz, L.F., Rangel-Mendez, R. *Effect of Carbon Quantum Dots concentration on their photoluminescence properties.* Poster presentation. The World Conference on Carbon 2023. Cancún, México.
3. Gonzalez-Vera, A.S., Ania, C., Pineda-Arellano, C.A., Ramírez-Monroy, A., Matos, J., Chazaro-Ruiz, L.F., Rangel-Mendez, R. *Carbon quantum dots produced from orange peel, their reduction degree, and the feasibility of their application on photovoltaic devices.* Poster presentation. Carbon 2022. London.
4. Gonzalez-Vera, A.S., Olmos-Moya, P.M., J., Chazaro-Ruiz, L.F., Rangel-Mendez, R. *Generación de puntos cuánticos de carbono para aumentar la eficiencia de dispositivos fotovoltaicos.* Poster presentation (online). Cuarto Taller Latinoamericano de Materiales de Carbono. 2021.

References

Acharya, B., Behera, A., Behera, S., & Moharana, S. (2024). Carbon quantum dots: A systematic overview of recent developments in synthesis, properties, and novel therapeutic applications. In *Inorganic Chemistry Communications* (Vol. 165). Elsevier B.V. https://doi.org/10.1016/j.inoche.2024.112492

Ai, L., Yang, Y., Wang, B., Chang, J., Tang, Z., Yang, B., & Lu, S. (2021). Insights into photoluminescence mechanisms of carbon dots: advances and perspectives. In *Science Bulletin* (Vol. 66, Issue 8, pp. 839–856). Elsevier B.V. https://doi.org/10.1016/j.scib.2020.12.015

Amancio, M. do A., Barcelay, Y. R., Gandarilla, A., Sales, R. R., de Souza, T. M., Nobre, F. X., Raphael, E., & Brito, W. R. (2025). Enhanced Grätzel Solar Cells Using Carbon Nanodots and Natural Dye. *ACS Physical Chemistry Au*, *5*(2), 151–161. https://doi.org/10.1021/acsphyschemau.4c00080

Andrade-Arias, A. S., Kabir, G., Mirmohammadsadeghi, M., Gunasekaran, A., & Elizondo-Noriega, A. (2025). Exploring public perspectives on solar energy adoption in Mexico. *Renewable and Sustainable Energy Reviews*, *212*, 115410. https://doi.org/10.1016/j.rser.2025.115410

Ania, C. O., Armstrong, P. A., Bandosz, T. J., Beguin, F., Carvalho, A. P., Celzard, A., Frackowiak, E., Gilarranz, M. A., László, K., Matos, J., & Pereira, M. F. R. (2020). Engaging nanoporous carbons in “beyond adsorption” applications:

Characterization, challenges and performance. *Carbon*, *164*, 69–84. https://doi.org/10.1016/j.carbon.2020.03.056

Araújo, M. P., Soares, O. S. G. P., Fernandes, A. J. S., Pereira, M. F. R., & Freire, C. (2017). Tuning the surface chemistry of graphene flakes: new strategies for selective oxidation. *RSC Advances*, *7*(23), 14290–14301. https://doi.org/10.1039/c6ra28868e

Balanta, M. A. G., da Silva Filho, W. J. F., Souza, M. C. G., de Assunção, R. M. N., Champi, A., & Cuevas, R. F. (2023). Deconvolution of photoluminescence spectra and electronic transition in carbon dots nanoparticles from microcrystalline cellulose. *Journal of Luminescence*, *255*, 119607. https://doi.org/10.1016/j.jlumin.2022.119607

Bandosz, T. J., Jagiello, J., Contescu, C., & Schwarz, J. A. (1993). Characterization of the surfaces of activated carbons in terms of their acidity constant distributions. In *Carbon* (Vol. 31, Issue 7).

Basem, A., Opakhai, S., Elbarbary, Z. M. S., Atamurotov, F., & Benti, N. E. (2025). A comprehensive analysis of advanced solar panel productivity and efficiency through numerical models and emotional neural networks. *Scientific Reports*, *15*(1), 259. https://doi.org/10.1038/s41598-024-70682-2

Baytar, O., Şahin, Ö., Horoz, S., & Kutluay, S. (2024). Solar Cell Efficiency Enhancement Via Mulberry Molasses-Based Carbon Quantum Dot-Supported CdS and CdS-Mn Nanomaterials. *Waste and Biomass Valorization*, *15*(7), 4395–4404. https://doi.org/10.1007/s12649-024-02484-6

Beiraghi, A., & Najibi-Gehraz, S. A. (2020). Purification and fractionation of carbon dots using phcontrolled cloud point extraction technique. *Journal of Nanostructures*, *10*(1), 107–118. https://doi.org/10.22052/JNS.2020.01.012

Boehm, H. P. (1994). Some aspects of the surface chemistry of carbon blacks and other carbons. In *Carbon* (Vol. 32, Issue 5).

Boruah, A., Saikia, M., Das, T., Goswamee, R. L., & Saikia, B. K. (2020). Blue-emitting fluorescent carbon quantum dots from waste biomass sources and their application in fluoride ion detection in water. *Journal of Photochemistry and Photobiology B: Biology*, *209*. https://doi.org/10.1016/j.jphotobiol.2020.111940

Castilla, C., Rüger, C. P., Lavanant, H., & Afonso, C. (2021). Ion mobility mass spectrometry of in situ generated biomass pyrolysis products. *Journal of Analytical and Applied Pyrolysis*, *156*. https://doi.org/10.1016/j.jaap.2021.105164

Cayuela Marín, A. (2016). *Contributions to developments of Carbon (Quantum) Dots as fluorescent sensors* [Universidad de Córdoba, Campus de Rabanales]. www.uco.es/publicacionespublicaciones@uco.es

Chapin, D. M., Fuller, C. S., & Pearson, G. L. (1954). A New Silicon *p-n* Junction Photocell for Converting Solar Radiation into Electrical Power. *Journal of Applied Physics*, *25*(5), 676–677. https://doi.org/10.1063/1.1721711

Chatzimitakos, T., Kasouni, A., Sygellou, L., Avgeropoulos, A., Troganis, A., & Stalikas, C. (2017). Two of a kind but different: Luminescent carbon quantum dots from Citrus peels for iron and tartrazine sensing and cell imaging. *Talanta*, *175*. https://doi.org/10.1016/j.talanta.2017.07.053

Chen, W., Zhu, Y., Xiu, J., Chen, G., Liang, H., Liu, S., Xue, H., Birgersson, E., Ho, J. W., Qin, X., Lin, J., Ma, R., Liu, T., He, Y., Ng, A. M.-C., Guo, X., He, Z., Yan, H., Djurišić, A. B., & Hou, Y. (2022). Monolithic perovskite/organic tandem solar cells with 23.6% efficiency enabled by reduced voltage losses and optimized interconnecting layer. *Nature Energy*, *7*(3), 229–237. https://doi.org/10.1038/s41560-021-00966-8

Chen, Y., Lian, H., Wei, Y., He, X., Chen, Y., Wang, B., Zeng, Q., & Lin, J. (2018). Concentration-induced multi-colored emissions in carbon dots: Origination from triple fluorescent centers. *Nanoscale*, *10*(14), 6734–6743. https://doi.org/10.1039/c8nr00204e

Choubey, P. C., Oudhia, A., & Dewangan, R. (2012). A review: Solar cell current scenario and future trends. *Recent Research in Science and Technology*, *4*(8). https://updatepublishing.com/journal/index.php/rrst/article/view/942

Christensen, E., Evans, R. J., & Carpenter, D. (2017). High-resolution mass spectrometric analysis of biomass pyrolysis vapors. *Journal of Analytical and Applied Pyrolysis*, *124*, 327–334. https://doi.org/10.1016/j.jaap.2017.01.015

Concina, I., & Vomiero, A. (2015). Metal Oxide Semiconductors for Dye- and Quantum-Dot-Sensitized Solar Cells. *Small*, *11*(15), 1744–1774. https://doi.org/10.1002/smll.201402334

Crittenden, J. C., Trussell, R. R., Hand, D. W., Howe, K. J., & Tchobanoglous, G. (2012). *MWH's water treatment: principles and design*. John Wiley & Sons.

D. Leon y Leon, A. C., & Radovic, L. (1993). Interfacial Chemistry and Electrochemistry of Carbon Surfaces. In *Chemistry & Physics of Carbon* (Thrower, P. A., Vol. 24). CRC Press.

Das, S. K., Chakrabarty, S., Gawas, R., & Jasuja, K. (2022). Serendipitous formation of photoluminescent carbon quantum dots by mere immersion of a polymer in an organic solvent. *Carbon Trends*, *8*. https://doi.org/10.1016/j.cartre.2022.100183

De, B., & Karak, N. (2013). A green and facile approach for the synthesis of water soluble fluorescent carbon dots from banana juice. *RSC Advances*, *3*(22), 8286–8290. https://doi.org/10.1039/c3ra00088e

Devi, M. S., Thangadurai, T. D., Manjubaashini, N., & Nataraj, D. (2023). Walnut shell biomass waste derived excitation-dependent CQDs for toxic insecticide sensing and protein denaturation inhibition – An ecofriendly and sustainable approach. *Diamond and Related Materials*, *136*. https://doi.org/10.1016/j.diamond.2023.110021

Ding, H., Wei, J. S., & Xiong, H. M. (2014). Nitrogen and sulfur co-doped carbon dots with strong blue luminescence. *Nanoscale*, *6*(22), 13817–13823. https://doi.org/10.1039/c4nr04267k

Energy Institute. (2025). *Statistical Review of World Energy 2025*. Energy Institute, London. https://www.energyinst.org/statistical-review/home

Essner, J. B., Kist, J. A., Polo-Parada, L., & Baker, G. A. (2018). Artifacts and Errors Associated with the Ubiquitous Presence of Fluorescent Impurities in Carbon Nanodots. *Chemistry of Materials*, *30*(6), 1878–1887. https://doi.org/10.1021/acs.chemmater.7b04446

Fahmey, M. A., Zayed, M. A., & Keshk, Y. H. (2001). *Comparative study on the fragmentation of some simple phenolic compounds using mass spectrometry and thermal analyses*.

Faisst, J., Jiang, E., Bogati, S., Pap, L., Zimmermann, B., Kroyer, T., Würfel, U., & List, M. (2023). Organic Solar Cell with an Active Area > 1 cm ^{2} Achieving 15.8% Certified Efficiency using Optimized VIS-NIR Antireflection Coating. *Solar RRL*, *7*(24). https://doi.org/10.1002/solr.202300663

Ganesan, S., Kalimuthu, R., Kanagaraj, T., Kulandaivelu, R., Nagappan, R., Pragasan, L. A., & Ponnusamy, V. K. (2022). Microwave-assisted green synthesis of multi-functional carbon quantum dots as efficient fluorescence sensor for ultra-trace level monitoring of ammonia in environmental water. *Environmental Research*, *206*. https://doi.org/10.1016/j.envres.2021.112589

Gao, N., Huang, L., Li, T., Song, J., Hu, H., Liu, Y., & Ramakrishna, S. (2020). Application of carbon dots in dye-sensitized solar cells: A review. In *Journal of Applied Polymer Science* (Vol. 137, Issue 10). John Wiley and Sons Inc. https://doi.org/10.1002/app.48443

Ghann, W., Sharma, V., Kang, H., Karim, F., Richards, B., Mobin, S. M., Uddin, J., Rahman, M. M., Hossain, F., Kabir, H., & Uddin, N. (2019). The synthesis and characterization of carbon dots and their application in dye sensitized solar cell.

International Journal of Hydrogen Energy, *44*(29), 14580–14587. https://doi.org/10.1016/j.ijhydene.2019.04.072

Gong, X., Chin Paau, M., Hu, Q., Shuang, S., Dong, C., & Choi, M. M. F. (2016). UHPLC combined with mass spectrometric study of as-synthesized carbon dots samples. *Talanta*, *146*, 340–350. https://doi.org/10.1016/j.talanta.2015.08.051

Green, M. A., Dunlop, E. D., Yoshita, M., Kopidakis, N., Bothe, K., Siefer, G., Hinken, D., Rauer, M., Hohl-Ebinger, J., & Hao, X. (2024). Solar cell efficiency tables (Version 64). *Progress in Photovoltaics: Research and Applications*, *32*(7), 425–441. https://doi.org/10.1002/pip.3831

Gude, V., Das, A., Chatterjee, T., & Mandal, P. K. (2016). Molecular origin of photoluminescence of carbon dots: Aggregation-induced orange-red emission. *Physical Chemistry Chemical Physics*, *18*(40), 28274–28280. https://doi.org/10.1039/c6cp05321a

Gudimella, K. K., Appidi, T., Wu, H. F., Battula, V., Jogdand, A., Rengan, A. K., & Gedda, G. (2021). Sand bath assisted green synthesis of carbon dots from citrus fruit peels for free radical scavenging and cell imaging. *Colloids and Surfaces B: Biointerfaces*, *197*. https://doi.org/10.1016/j.colsurfb.2020.111362

Hames, B., Ruiz, R., Scarlata, C., Sluiter, A., Sluiter, J., & Templeton, D. (2008). *Preparation of Samples for Compositional Analysis: Laboratory Analytical Procedure (LAP); Issue Date 08/08/2008*. www.nrel.gov

Han, L., Fukui, A., Chiba, Y., Islam, A., Komiya, R., Fuke, N., Koide, N., Yamanaka, R., & Shimizu, M. (2009). Integrated dye-sensitized solar cell module with conversion efficiency of 8.2%. *Applied Physics Letters*, *94*(1). https://doi.org/10.1063/1.3054160

Harding, S. E., Berth, G., Ball, A., Mitchell, J. R., & de la Torre, J. G. (1991). The molecular weight distribution and conformation of citrus pectins in solution studied by hydrodynamics. *Carbohydrate Polymers*, *16*(1), 1–15. https://doi.org/10.1016/0144-8617(91)90069-O

Hassanzadeh, S., Adolfsson, K. H., & Hakkarainen, M. (2015). Controlling the cooperative self-assembly of graphene oxide quantum dots in aqueous solutions. *RSC Advances*, *5*(71), 57425–57432. https://doi.org/10.1039/c5ra09704e

Hu, Q., Paau, M. C., Zhang, Y., Gong, X., Zhang, L., Lu, D., Liu, Y., Liu, Q., Yao, J., & Choi, M. M. F. (2014). Green synthesis of fluorescent nitrogen/sulfur-doped carbon dots and investigation of their properties by HPLC coupled with mass spectrometry. *RSC Advances*, *4*(35), 18065–18073. https://doi.org/10.1039/c4ra02170c

Hu, X., Li, Y., Xu, Y., Gan, Z., Zou, X., Shi, J., Huang, X., Li, Z., & Li, Y. (2021). Green one-step synthesis of carbon quantum dots from orange peel for fluorescent detection of Escherichia coli in milk. *Food Chemistry*, *339*. https://doi.org/10.1016/j.foodchem.2020.127775

IEA. (2023). *CO2 Emissions in 2022, IEA, Paris*.

Jagiellot, J. (1994). Stable Numerical Solution of the Adsorption Integral Equation Using Splines. In *Langmuir* (Vol. 10).

Jia, X., Li, J., & Wang, E. (2012). One-pot green synthesis of optically pH-sensitive carbon dots with upconversion luminescence. *Nanoscale*, *4*(18), 5572–5575. https://doi.org/10.1039/c2nr31319g

Jing, S., Zhao, Y., Sun, R. C., Zhong, L., & Peng, X. (2019). Facile and High-Yield Synthesis of Carbon Quantum Dots from Biomass-Derived Carbons at Mild Condition. *ACS Sustainable Chemistry and Engineering*, *7*(8), 7833–7843. https://doi.org/10.1021/acssuschemeng.9b00027

Jo, I. R., Lee, Y. H., Kim, H., & Ahn, K. S. (2021). Multifunctional nitrogen-doped graphene quantum dots incorporated into mesoporous TiO2 films for quantum dot-sensitized solar cells. *Journal of Alloys and Compounds*, *870*. https://doi.org/10.1016/j.jallcom.2021.159527

Kambhampati, P. (2011). Unraveling the Structure and Dynamics of Excitons in Semiconductor Quantum Dots. *Accounts of Chemical Research*, *44*(1), 1–13. https://doi.org/10.1021/ar1000428

Kansay, V., Sharma, V. D., Chandan, G., Sharma, I., Chakrabarti, S., & Bera, M. K. (2023). Sustainable synthesis of nitrogen-doped fluorescent carbon quantum dots derived from Cissus quadrangularis for biomarker applications. *Materials Chemistry and Physics*, *296*. https://doi.org/10.1016/j.matchemphys.2022.127237

Kayes, B. M., Nie, H., Twist, R., Spruytte, S. G., Reinhardt, F., Kizilyalli, I. C., & Higashi, G. S. (2011). 27.6% conversion efficiency, a new record for single-junction solar cells under 1 sun illumination. *2011 37th IEEE Photovoltaic Specialists Conference*, 4–8.

Komiya, R., Fukui, A., Murofushi, N., Koide, N., Yamanaka, R., & Katayama, H. (2011). Improvement of the conversion efficiency of a monolithic type dye sensitized solar cell module. In *21st International Photovoltaic Science and Engineering Conference, Fukuoka*.

Kraemer, E. O. (1938). Molecular Weights of Celluloses and Cellulose Derivates. *Industrial & Engineering Chemistry*, *30*(10), 1200–1203. https://doi.org/10.1021/ie50346a023

Krysmann, M. J., Kelarakis, A., Dallas, P., & Giannelis, E. P. (2012). Formation mechanism of carbogenic nanoparticles with dual photoluminescence emission. *Journal of the American Chemical Society*, *134*(2), 747–750. https://doi.org/10.1021/ja204661r

Kumar, P., Dua, S., Kaur, R., Kumar, M., & Bhatt, G. (2022). A review on advancements in carbon quantum dots and their application in photovoltaics. In *RSC Advances* (Vol. 12, Issue 8, pp. 4714–4759). Royal Society of Chemistry. https://doi.org/10.1039/d1ra08452f

Langer, M., Zdražil, L., Medveď, M., & Otyepka, M. (2023). Communication of molecular fluorophores with other photoluminescence centres in carbon dots. *Nanoscale*, *15*(8), 4022–4032. https://doi.org/10.1039/d2nr05114a

Le Brech, Y., Jia, L., Cissé, S., Mauviel, G., Brosse, N., & Dufour, A. (2016). Mechanisms of biomass pyrolysis studied by combining a fixed bed reactor with advanced gas analysis. *Journal of Analytical and Applied Pyrolysis*, *117*, 334–346. https://doi.org/10.1016/j.jaap.2015.10.013

Leon, C. A., Leon, Y., Solar, J. M., Calemma, V., & Radovic, L. R. (1992). Evidence for the protonation of basal plane sites on carbon. In *Carbon* (Vol. 30, Issue 5).

Li, C., Yao, D., Dong, P., Tang, Z., Li, Y., Chen, B., Tian, N., Zheng, G., Peng, Y., & Long, F. (2024). Synergetic modification on buried and upper surfaces of perovskites with nitrogen-doped carbon quantum dots for efficient and stable solar cells. *Applied Surface Science*, *658*, 159848. https://doi.org/10.1016/j.apsusc.2024.159848

Li, L., Lu, C., Li, S., Liu, S., Wang, L., Cai, W., Xu, W., Yang, X., Liu, Y., & Zhang, R. (2017). A high-yield and versatile method for the synthesis of carbon dots for bioimaging applications. *Journal of Materials Chemistry B*, *5*(10), 1935–1942. https://doi.org/10.1039/C6TB03003C

Li, P., Xue, S., Sun, L., Zong, X., An, L., Qu, D., Wang, X., & Sun, Z. (2022). Formation and fluorescent mechanism of red emissive carbon dots from o-phenylenediamine and catechol system. *Light: Science and Applications*, *11*(1). https://doi.org/10.1038/s41377-022-00984-5

Liang, J., Jiao, Y., Jaroniec, M., & Qiao, S. Z. (2012). Sulfur and Nitrogen Dual-Doped Mesoporous Graphene Electrocatalyst for Oxygen Reduction with Synergistically Enhanced Performance. *Angewandte Chemie*, *124*(46), 11664–11668. https://doi.org/10.1002/ange.201206720

Liang, W. Y. (1970). Excitons. *Physics Education*, *5*(4), 003. https://doi.org/10.1088/0031-9120/5/4/003

Lim, J., Yeap, S. P., Che, H. X., & Low, S. C. (2013). Characterization of magnetic nanoparticle by dynamic light scattering. *Nanoscale Research Letters*, *8*(1). https://doi.org/10.1186/1556-276X-8-381

Liu, M. (2020). Optical Properties of Carbon Dots: A Review. *Nanoarchitectonics*, *1*(1), 1–12. https://doi.org/10.37256/nat.112020124.1-12

Liu, M. L., Chen, B. Bin, Li, C. M., & Huang, C. Z. (2019). Carbon dots: Synthesis, formation mechanism, fluorescence origin and sensing applications. In *Green Chemistry* (Vol. 21, Issue 3, pp. 449–471). Royal Society of Chemistry. https://doi.org/10.1039/c8gc02736f

Liu, W., Li, C., Sun, X., Pan, W., Yu, G., & Wang, J. (2017). Highly crystalline carbon dots from fresh tomato: UV emission and quantum confinement. *Nanotechnology*, *28*(48). https://doi.org/10.1088/1361-6528/aa900b

Liu, Y., Huang, H., Cao, W., Mao, B., Liu, Y., & Kang, Z. (2020). Advances in carbon dots: From the perspective of traditional quantum dots. In *Materials Chemistry Frontiers* (Vol. 4, Issue 6, pp. 1586–1613). Royal Society of Chemistry. https://doi.org/10.1039/d0qm00090f

LONGi. (2024, May 7). *LONGi Sets New World-Record for Silicon Solar Cell Efficiency, Launching 2nd Generation Ultra-Efficient BC-Based Module*. Https://Www.Longi.Com/En/News/Longi-Hi-Mo9-Bc-World-Record/.

Lu, W., Qin, X., Liu, S., Chang, G., Zhang, Y., Luo, Y., Asiri, A. M., Al-Youbi, A. O., & Sun, X. (2012). Economical, green synthesis of fluorescent carbon nanoparticles and their use as probes for sensitive and selective detection of mercury(II) ions. *Analytical Chemistry*, *84*(12). https://doi.org/10.1021/ac3007939

Lu, Y., Wang, J., Yuan, H., & Xiao, D. (2014). Separation of carbon quantum dots on a C18 column by binary gradient elution via HPLC. *Analytical Methods*, *6*(20), 8124–8128. https://doi.org/10.1039/c4ay01052c

M. Abdoon, F., & M. Atawy, H. (2021). Prospective of microwave-assisted and hydrothermal synthesis of carbon quantum dots/silver nanoparticles for spectrophotometric determination of losartan potassium in pure form and pharmaceutical formulations. *Materials Today: Proceedings*, *42*, 2141–2149. https://doi.org/10.1016/j.matpr.2020.12.298

Malavika, J. P., Shobana, C., Ragupathi, M., Kumar, P., Lee, Y. S., Govarthanan, M., & Selvan, R. K. (2021). A sustainable green synthesis of functionalized biocompatible carbon quantum dots from Aloe barbadensis Miller and its multifunctional applications. *Environmental Research*, *200*. https://doi.org/10.1016/j.envres.2021.111414

Matos, J., Atienzar, P., García, H., & Hernández-Garrido, J. C. (2013). Nanocrystalline carbon-TiO2 hybrid hollow spheres as possible electrodes for solar cells. *Carbon*, *53*, 169–181. https://doi.org/10.1016/j.carbon.2012.10.044

Matsui, T., Bidiville, A., Maejima, K., Sai, H., Koida, T., Suezaki, T., Matsumoto, M., Saito, K., Yoshida, I., & Kondo, M. (2015). High-efficiency amorphous silicon solar cells: Impact of deposition rate on metastability. *Applied Physics Letters*, *106*(5). https://doi.org/10.1063/1.4907001

Mintz, K. J., Bartoli, M., Rovere, M., Zhou, Y., Hettiarachchi, S. D., Paudyal, S., Chen, J., Domena, J. B., Liyanage, P. Y., Sampson, R., Khadka, D., Pandey, R. R., Huang, S., Chusuei, C. C., Tagliaferro, A., & Leblanc, R. M. (2021). A deep investigation into the structure of carbon dots. *Carbon*, *173*, 433–447. https://doi.org/10.1016/j.carbon.2020.11.017

Mintz, K. J., Zhou, Y., & Leblanc, R. M. (2019). Recent development of carbon quantum dots regarding their optical properties, photoluminescence mechanism, and core structure. In *Nanoscale* (Vol. 11, Issue 11, pp. 4634–4652). Royal Society of Chemistry. https://doi.org/10.1039/c8nr10059d

Miranda, R., Bustos-Martinez, D., Blanco, C. S., Villarreal, M. H. G., & Cantú, M. E. R. (2009). Pyrolysis of sweet orange (Citrus sinensis) dry peel. *Journal of*

Analytical and Applied Pyrolysis, *86*(2), 245–251. https://doi.org/10.1016/j.jaap.2009.06.001

Mishra, K., Barai, M., & Ghosh, S. (2022). Roles of Impurity and Sample Heterogeneity in Intriguing Photoluminescence Properties of Zero-Dimensional (0D) Carbonaceous Materials. In *Journal of Physical Chemistry C*. American Chemical Society. https://doi.org/10.1021/acs.jpcc.2c05477

Mohammed, M. K. A., Al-Mousoi, A. K., Singh, S., Kumar, A., Hossain, M. K., Salih, S. Q., Sasikumar, P., Pandey, R., A. Yadav, A., & Yaseen, Z. M. (2023). Improving the performance of perovskite solar cells with carbon nanotubes as a hole transport layer. *Optical Materials*, *138*, 113702. https://doi.org/10.1016/j.optmat.2023.113702

Nakamura, M., Yamaguchi, K., Kimoto, Y., Yasaki, Y., Kato, T., & Sugimoto, H. (2019). Cd-Free Cu(In,Ga)(Se,S)2 Thin-Film Solar Cell With Record Efficiency of 23.35%. *IEEE Journal of Photovoltaics*, *9*(6), 1863–1867. https://doi.org/10.1109/JPHOTOV.2019.2937218

Nallayagari, A. R., Sgreccia, E., Pizzoferrato, R., Cabibbo, M., Kaciulis, S., Bolli, E., Pasquini, L., Knauth, P., & Di Vona, M. L. (2022). Tuneable properties of carbon quantum dots by different synthetic methods. *Journal of Nanostructure in Chemistry*, *12*(4), 565–580. https://doi.org/10.1007/s40097-021-00431-8

Nawab, F., Abd Hamid, A. S., Ibrahim, A., Sopian, K., Fazlizan, A., & Fauzan, M. F. (2023). Solar irradiation prediction using empirical and artificial intelligence methods: A comparative review. *Heliyon*, *9*(6), e17038. https://doi.org/10.1016/j.heliyon.2023.e17038

Nguyen, K. G., Baragau, I. A., Gromicova, R., Nicolaev, A., Thomson, S. A. J., Rennie, A., Power, N. P., Sajjad, M. T., & Kellici, S. (2022). Investigating the effect of N-doping on carbon quantum dots structure, optical properties and metal ion screening. *Scientific Reports*, *12*(1). https://doi.org/10.1038/s41598-022-16893-x

Nguyen-Le, M. T., Nguyen, C. K., Nam, P. H., Thoa, D. T., Phong, N. Van, Tri, N. H., Viet, N. M., Viet Ha, T. T., & Nguyen, L. H. (2022). Facile development of carbon quantum dot deposited titanate-based materials for environmental application. *Materials Chemistry and Physics*, *287*. https://doi.org/10.1016/j.matchemphys.2022.126319

NOAA National Centers for Environmental Information. (2024). *Monthly Global Climate Report for Annual 2023*. https://www.ncei.noaa.gov/access/metadata/landing-page/bin/iso?id=gov.noaa.ncdc:C00672

Nxele, S. R., & Nyokong, T. (2022). Time-dependent characterization of graphene quantum dots and graphitic carbon nitride quantum dots synthesized by hydrothermal methods. *Diamond and Related Materials*, *121*. https://doi.org/10.1016/j.diamond.2021.108751

Olmos-Moya, P. M., Velazquez-Martinez, S., Pineda-Arellano, C., Rangel-Mendez, J. R., & Chazaro-Ruiz, L. F. (2022). High added value functionalized carbon quantum dots synthetized from orange peels by assisted microwave solvothermal method and their performance as photosensitizer of mesoporous TiO2 photoelectrodes. *Carbon*, *187*, 216–229. https://doi.org/10.1016/j.carbon.2021.11.003

Otyepka, M., Langer, M., Paloncýová, M., & Medved', M. (2020). Molecular fluorophores self-organize into c-dot seeds and incorporate into c-dot structures. *Journal of Physical Chemistry Letters*, *11*(19), 8252–8258. https://doi.org/10.1021/acs.jpclett.0c01873

Pan, Y., Qiao, L., Zhu, Z., Ran, X., Kuang, Y., Chi, Z., He, Y., Liu, R., & Guo, L. (2023). Highly enhanced photoluminescence and suppressed blinking of N-doped carbon dots by targeted passivation of amine group for mechanistic insights and Vis-NIR excitation bioimaging application. *Carbon*, *213*, 118212. https://doi.org/10.1016/j.carbon.2023.118212

Pande, P. M., Pandey, S. P., Shirsat, S. P., & Wagh, S. M. (2024). Zero-, one-, two-, and three-dimensional carbon nanostructures derived from bio-based material. In *Bio-derived Carbon Nanostructures* (pp. 83–107). Elsevier. https://doi.org/10.1016/B978-0-443-13579-8.00017-6

Paul, A., & Kurian, M. (2021). Facile synthesis of nitrogen doped carbon dots from waste biomass: Potential optical and biomedical applications. *Cleaner Engineering and Technology*, *3*. https://doi.org/10.1016/j.clet.2021.100103

Perumal, S., Atchudan, R., Edison, T. N. J. I., & Lee, Y. R. (2021). Sustainable synthesis of multifunctional carbon dots using biomass and their applications: A mini-review. In *Journal of Environmental Chemical Engineering* (Vol. 9, Issue 4). Elsevier Ltd. https://doi.org/10.1016/j.jece.2021.105802

Pons, T., Uyeda, H. T., Medintz, I. L., & Mattoussi, H. (2006). Hydrodynamic dimensions, electrophoretic mobility, and stability of hydrophilic quantum dots. *Journal of Physical Chemistry B*, *110*(41), 20308–20316. https://doi.org/10.1021/jp065041h

Prasannan, A., & Imae, T. (2013). One-pot synthesis of fluorescent carbon dots from orange waste peels. *Industrial and Engineering Chemistry Research*, *52*(44), 15673–15678. https://doi.org/10.1021/ie402421s

Rangel-Mendez, J. R., Matos, J., Cházaro-Ruiz, L. F., González-Castillo, A. C., & Barrios-Yáñez, G. (2018). Microwave-assisted synthesis of C-doped TiO 2 and ZnO hybrid nanostructured materials as quantum-dots sensitized solar cells. *Applied Surface Science*, *434*, 744–755. https://doi.org/10.1016/j.apsusc.2017.10.236

Rasal, A. S., Subrahmanya, T. M., Kizhepat, S., Getachew, G., Ghule, A. V., Devan, R. S., Hung, W.-S., Fahmi, M. Z., Wibrianto, A., & Chang, J.-Y. (2025). Carbon quantum dots: Classification-structure-property-application relationship for biomedical and environment remediation. *Coordination Chemistry Reviews*, *533*, 216510. https://doi.org/10.1016/j.ccr.2025.216510

Riaz, S., & Park, S. J. (2022a). Carbon quantum dots-embedded graphitic carbon nitride nanotubes for enhancing the power conversion efficiency of sensitized solar cells. *Materials Today Chemistry*, *24*, 100763. https://doi.org/10.1016/J.MTCHEM.2021.100763

Riaz, S., & Park, S. J. (2022b). Thioacetamide-derived nitrogen and sulfur co-doped carbon quantum dots for “green” quantum dot solar cells. *Journal of Industrial and Engineering Chemistry*, *105*, 111–120. https://doi.org/10.1016/J.JIEC.2021.09.009

Rocha, R. P., Pereira, M. F. R., & Figueiredo, J. L. (2023). Characterisation of the surface chemistry of carbon materials by temperature-programmed desorption: An assessment. *Catalysis Today*, *418*. https://doi.org/10.1016/j.cattod.2023.114136

Roy, S., Preeyanka, N., Majhi, D., Seth, S., & Sarkar, M. (2018). Striking Similarities in the Fluorescence Behavior between Carbon Dots and Ionic Liquids: Toward Understanding the Fluorescence Behavior of Carbon Dots. *Journal of Physical Chemistry C*, *122*(23), 12384–12394. https://doi.org/10.1021/acs.jpcc.8b03859

Sadezky, A., Muckenhuber, H., Grothe, H., Niessner, R., & Pöschl, U. (2005). Raman microspectroscopy of soot and related carbonaceous materials: Spectral analysis and structural information. *Carbon*, *43*(8), 1731–1742. https://doi.org/10.1016/j.carbon.2005.02.018

Sai, H., Matsui, T., Kumagai, H., & Matsubara, K. (2018). Thin-film microcrystalline silicon solar cells: 11.9% efficiency and beyond. *Applied Physics Express*, *11*(2), 022301. https://doi.org/10.7567/APEX.11.022301

Sawalha, S. M. S., Arráez-Román, D., Segura-Carretero, A., & Fernández-Gutiérrez, A. (2009). Quantification of main phenolic compounds in sweet and bitter orange peel using CE-MS/MS. *Food Chemistry*, *116*(2), 567–574. https://doi.org/10.1016/j.foodchem.2009.03.003

Secretaría de Desarrollo Agropecuario y Recursos Hidráulicos. (2022). *SLP tercer productor nacional de naranja*. https://slp.gob.mx/sedarh/Paginas/SLP-TERCER-PRODUCTOR-NACIONAL-DE-NARANJA.aspx

Shan, F., Zhang, J., Liao, C., Wang, Z., & Wang, L. (2023). Mechanisms of photoluminescence in the molecular state of carbon dots prepared from o-phenylenediamine. *Chinese Chemical Letters*, *34*(7), 108107. https://doi.org/10.1016/j.cclet.2022.108107

Sharma, V. D., Kansay, V., Bhatia, A., & Bera, M. K. (2023). Influence of intentional phosphorus doping on Brassica juncea-derived unintentionally N, Ca-doped carbon quantum dots@bioplastic composites for applications in LED and UV-tube down-conversion. *Materials Chemistry and Physics*, *303*. https://doi.org/10.1016/j.matchemphys.2023.127834

Shejale, K. P., Jaiswal, A., Kumar, A., Saxena, S., & Shukla, S. (2021). Nitrogen doped carbon quantum dots as Co-active materials for highly efficient dye sensitized solar cells. *Carbon*, *183*, 169–175. https://doi.org/10.1016/j.carbon.2021.06.090

Sikiru, S., Oladosu, T. L., Kolawole, S. Y., Mubarak, L. A., Soleimani, H., Afolabi, L. O., & Oluwafunke Toyin, A. O. (2023). Advance and prospect of carbon quantum dots synthesis for energy conversion and storage application: A comprehensive review. In *Journal of Energy Storage* (Vol. 60). Elsevier Ltd. https://doi.org/10.1016/j.est.2022.106556

Sk, M. A., Ananthanarayanan, A., Huang, L., Lim, K. H., & Chen, P. (2014). Revealing the tunable photoluminescence properties of graphene quantum dots. *Journal of Materials Chemistry C*, *2*(34), 6954–6960. https://doi.org/10.1039/c4tc01191k

Sluiter, A., Hames, B., Ruiz, R., Scarlata, C., Sluiter, J., Templeton, D., & Crocker, D. (2008). *Determination of Structural Carbohydrates and Lignin in Biomass: Laboratory Analytical Procedure (LAP) (Revised July 2011)*. http://www.nrel.gov/biomass/analytical_procedures.html

Spectrum Labs. (2012). *Laboratory Product Catalog*. https://www.laboplus.pl/wp-content/uploads/2019/12/2012-Katalog-Spectrum.pdf

Sunitha, A. P., Sandeep, K., Rose, J., Hajara, P., & Saji, K. J. (2021). Carbon quantum dots synthesized from Plectranthus Amboinicus: An eco-friendly material with excellent non-linear optical properties. *Materials Today: Proceedings*, *47*, 1601–1604. https://doi.org/10.1016/j.matpr.2021.04.288

Surendran, P., Lakshmanan, A., Priya, S. S., Geetha, P., Rameshkumar, P., Kannan, K., Hegde, T. A., & Vinitha, G. (2021). Fluorescent carbon quantum dots from Ananas comosus waste peels: A promising material for NLO behaviour, antibacterial, and antioxidant activities. *Inorganic Chemistry Communications*, *124*. https://doi.org/10.1016/j.inoche.2020.108397

Tao, S., Feng, T., Zheng, C., Zhu, S., & Yang, B. (2019). Carbonized Polymer Dots: A Brand New Perspective to Recognize Luminescent Carbon-Based Nanomaterials. In *Journal of Physical Chemistry Letters* (pp. 5182–5188). American Chemical Society. https://doi.org/10.1021/acs.jpclett.9b01384

Tao, S., Zhou, C., Kang, C., Zhu, S., Feng, T., Zhang, S.-T., Ding, Z., Zheng, C., Xia, C., & Yang, B. (2022). Confined-domain crosslink-enhanced emission effect in carbonized polymer dots. *Light: Science & Applications*, *11*(1), 56. https://doi.org/10.1038/s41377-022-00745-4

Tao, S., Zhu, S., Feng, T., Zheng, C., & Yang, B. (2020). Crosslink-Enhanced Emission Effect on Luminescence in Polymers: Advances and Perspectives. In *Angewandte Chemie - International Edition* (Vol. 59, Issue 25, pp. 9826–9840). Wiley-VCH Verlag. https://doi.org/10.1002/anie.201916591

Thangaraj, B., Solomon, P. R., Chuangchote, S., Wongyao, N., & Surareungchai, W. (2021). Biomass-derived Carbon Quantum Dots – A Review. Part 1: Preparation and Characterization. *ChemBioEng Reviews*, *8*(4), 265–301. https://doi.org/10.1002/cben.202000029

Tiong, A. N. L., Wong, N. K. H., Fong, J. F. Y., Tan, X. W., & Ng, S. M. (2015). A sustainable alternative to synthesis optical sensing receptor for the detection of metal ions. *Optical Materials*, *40*, 132–138. https://doi.org/10.1016/j.optmat.2014.12.021

Titirici, M.-M., White, R. J., Brun, N., Budarin, V. L., Su, D. S., del Monte, F., Clark, J. H., & MacLachlan, M. J. (2015). Sustainable carbon materials. *Chemical Society Reviews*, *44*(1), 250–290. https://doi.org/10.1039/C4CS00232F

Venkateswara Raju, C., Kalaiyarasan, G., Paramasivam, S., Joseph, J., & Senthil Kumar, S. (2020). Phosphorous doped carbon quantum dots as an efficient solid state electrochemiluminescence platform for highly sensitive turn-on detection of Cu2+ ions. *Electrochimica Acta*, *331*. https://doi.org/10.1016/j.electacta.2019.135391

Vercelli, B., Donnini, R., Ghezzi, F., Sansonetti, A., Giovanella, U., & La Ferla, B. (2021). Nitrogen-doped carbon quantum dots obtained hydrothermally from citric acid and urea: The role of the specific nitrogen centers in their electrochemical and optical responses. *Electrochimica Acta*, *387*. https://doi.org/10.1016/j.electacta.2021.138557

Wang, C., Shi, H., Yang, M., Yan, Y., Liu, E., Ji, Z., & Fan, J. (2020). Facile synthesis of novel carbon quantum dots from biomass waste for highly sensitive detection of iron ions. *Materials Research Bulletin*, *124*. https://doi.org/10.1016/j.materresbull.2019.110730

Wang, M., Shi, R., Gao, M., Zhang, K., Deng, L., Fu, Q., Wang, L., & Gao, D. (2020a). Sensitivity fluorescent switching sensor for Cr (VI) and ascorbic acid detection based on orange peels-derived carbon dots modified with EDTA. *Food Chemistry*, *318*. https://doi.org/10.1016/j.foodchem.2020.126506

Wang, M., Shi, R., Gao, M., Zhang, K., Deng, L., Fu, Q., Wang, L., & Gao, D. (2020b). Sensitivity fluorescent switching sensor for Cr (VI) and ascorbic acid detection based on orange peels-derived carbon dots modified with EDTA. *Food Chemistry*, *318*. https://doi.org/10.1016/j.foodchem.2020.126506

Wang, X., Xu, L., Ge, S., Foong, S. Y., Liew, R. K., Fong Chong, W. W., Verma, M., Naushad, Mu., Park, Y.-K., Lam, S. S., Li, Q., & Huang, R. (2023). Biomass-based carbon quantum dots for polycrystalline silicon solar cells with enhanced photovoltaic performance. *Energy*, *274*, 127354. https://doi.org/10.1016/j.energy.2023.127354

Wang, X., Zhang, X., Zhou, G., Qian, J., Li, Z., & Li, W. (2024). Feasibility study on the separation and purification of sinomenine hydrochloride from Caulis sinomenii solution based on membrane ultrafiltration technology. *Sustainable Chemistry and Pharmacy*, *39*, 101549. https://doi.org/10.1016/j.scp.2024.101549

Wang, Z., Rong, X., Wang, L., Wang, W., Lin, H., & Li, X. (2020). Dual Role of Amino-Functionalized Graphene Quantum Dots in NiOx Films for Efficient Inverted Flexible Perovskite Solar Cells. *ACS Applied Materials & Interfaces*, *12*(7), 8342–8350. https://doi.org/10.1021/acsami.9b22471

Wu, P., Li, W., Wu, Q., Liu, Y., & Liu, S. (2017). Hydrothermal synthesis of nitrogen-doped carbon quantum dots from microcrystalline cellulose for the detection of Fe3+ ions in an acidic environment. *RSC Advances*, *7*(70), 44144–44153. https://doi.org/10.1039/c7ra08400e

Wypych, A. (2023). Lignin. In *Databook of Adhesion Promoters* (p. 149). Elsevier. https://doi.org/10.1016/B978-1-77467-012-5.50019-6

Xie, J., Cao, Q., Wang, W. jun, Zhang, H. yan, & Deng, B. (2023). Understanding changes in volatile compounds and fatty acids of Jincheng orange peel oil at different growth stages using GC–MS. *Journal of Integrative Agriculture*, *22*(7), 2282–2294. https://doi.org/10.1016/j.jia.2023.05.015

Xu, J., Zhou, P., Yuan, L., Liu, X., Ma, J., & Zhang, C. (2021). Dual lignin valorization enabled by carbon quantum dots and lithium-sulfur cathode. *Industrial Crops and Products*, *170*. https://doi.org/10.1016/j.indcrop.2021.113801

Xu, T., Wan, Z., Tang, H., Zhao, C., Lv, S., Chen, Y., Chen, L., Qiao, Q., & Huang, W. (2021). Carbon quantum dot additive engineering for efficient and stable carbon-based perovskite solar cells. *Journal of Alloys and Compounds*, *859*. https://doi.org/10.1016/j.jallcom.2020.157784

Xu, X., Ray, R., Gu, Y., Ploehn, H. J., Gearheart, L., Raker, K., & Scrivens, W. A. (2004). Electrophoretic analysis and purification of fluorescent single-walled carbon nanotube fragments. *Journal of the American Chemical Society*, *126*(40), 12736–12737. https://doi.org/10.1021/ja040082h

Yan, F., Sun, Z., Zhang, H., Sun, X., Jiang, Y., & Bai, Z. (2019). The fluorescence mechanism of carbon dots, and methods for tuning their emission color: a review. In *Microchimica Acta* (Vol. 186, Issue 8). Springer-Verlag Wien. https://doi.org/10.1007/s00604-019-3688-y

Yang, G., Wan, X., Su, Y., Zeng, X., & Tang, J. (2016). Acidophilic S-doped carbon quantum dots derived from cellulose fibers and their fluorescence sensing performance for metal ions in an extremely strong acid environment. *Journal of Materials Chemistry A*, *4*(33), 12841–12849. https://doi.org/10.1039/c6ta05943k

Yang, Q., Duan, J., Yang, W., Li, X., Mo, J., Yang, P., & Tang, Q. (2018). Nitrogen-doped carbon quantum dots from biomass via simple one-pot method and exploration of their application. *Applied Surface Science*, *434*, 1079–1085. https://doi.org/10.1016/j.apsusc.2017.11.040

Zdražil, L., Kalytchuk, S., Holá, K., Petr, M., Zmeškal, O., Kment, Š., Rogach, A. L., & Zbořil, R. (2020). A carbon dot-based tandem luminescent solar concentrator. *Nanoscale*, *12*(12), 6664–6672. https://doi.org/10.1039/C9NR10029F

Zhang, C., Liang, S., Liu, W., Eickemeyer, F. T., Cai, X., Zhou, K., Bian, J., Zhu, H., Zhu, C., Wang, N., Wang, Z., Zhang, J., Wang, Y., Hu, J., Ma, H., Xin, C., Zakeeruddin, S. M., Grätzel, M., & Shi, Y. (2021). Ti1–graphene single-atom material for improved energy level alignment in perovskite solar cells. *Nature Energy*, *6*(12), 1154–1163. https://doi.org/10.1038/s41560-021-00944-0

Zhang, J., Liu, Q., Wang, J., He, H., Shi, F., Xing, B., Jia, J., Huang, G., & Zhang, C. (2021). Facile preparation of carbon quantum dots/TiO2 composites at room temperature with improved visible-light photocatalytic activity. *Journal of Alloys and Compounds*, *869*. https://doi.org/10.1016/j.jallcom.2021.159389

Zhang, W., Shi, L., Liu, Y., Meng, X., Xu, H., Xu, Y., Liu, B., Fang, X., Li, H.-B., & Ding, T. (2017). Supramolecular interactions via hydrogen bonding contributing to citric-acid derived carbon dots with high quantum yield and sensitive photoluminescence. *RSC Advances*, *7*(33), 20345–20353. https://doi.org/10.1039/C7RA02160G

Zhang, Y. Q., Ma, D. K., Zhang, Y. G., Chen, W., & Huang, S. M. (2013). N-doped carbon quantum dots for TiO2-based photocatalysts and dye-sensitized solar cells. *Nano Energy*, *2*(5), 545–552. https://doi.org/10.1016/j.nanoen.2013.07.010

Zhao, Y., Duan, J., He, B., Jiao, Z., & Tang, Q. (2018). Improved charge extraction with N-doped carbon quantum dots in dye-sensitized solar cells. *Electrochimica Acta*, *282*, 255–262. https://doi.org/10.1016/j.electacta.2018.06.060

Zhu, J., Wu, C., Cui, Y., Li, D., Zhang, Y., Xu, J., Li, C., Iqbal, S., & Cao, M. (2021). Blue-emitting carbon quantum dots: Ultrafast microwave synthesis, purification and strong fluorescence in organic solvents. *Colloids and Surfaces A: Physicochemical and Engineering Aspects*, *623*. https://doi.org/10.1016/j.colsurfa.2021.126673

Zhu, S., Song, Y., Zhao, X., Shao, J., Zhang, J., & Yang, B. (2015). The photoluminescence mechanism in carbon dots (graphene quantum dots, carbon nanodots, and polymer dots): current state and future perspective. *Nano Research*, *8*(2), 355–381. https://doi.org/10.1007/s12274-014-0644-3

Zhu, X., Sun, J., Yuan, S., Li, N., Qiu, Z., Jia, J., Liu, Y., Dong, J., Lv, P., & Cao, B. (2019). Efficient and stable planar perovskite solar cells with carbon quantum dots-doped PCBM electron transport layer. *New Journal of Chemistry*, *43*(18), 7130–7135. https://doi.org/10.1039/c8nj06146g

Zioga, M., Tsouko, E., Maina, S., Koutinas, A., Mandala, I., & Evageliou, V. (2022). Physicochemical and rheological characteristics of pectin extracted from renewable orange peel employing conventional and green technologies. *Food Hydrocolloids*, *132*. https://doi.org/10.1016/j.foodhyd.2022.107887

Appendix 1

Reduced biomass-derived Carbon Dots

Appendix 1: Reduced biomass-derived Carbon Dots

1.1. Introduction

The selective remotion of oxygenated groups modifies the electrical and mechanical properties of certain carbon materials. In the case of CDs, is expected that a removal of oxygenated groups though reduction of the material, will increase the conductivity and modify the optical properties of the reduced-CDs in comparison to the pristine material.

This appendix presents the results of an experimental approach aimed at applying a reduction treatment to CDs. The CDs utilized were synthetized from orange peel and purified though the methods described at Chapter 2 of this document. The CDs powder was evaluated through Thermogravimetric analysis (TGA) and Temperature Programmed Desorption coupled with Mass Spectrometry (TPD-MS) at different m/z values (Section 2.3.4.2). According to the results from these analyses, a thermal reduction strategy was implemented to modify the pristine material. At Figure 47 is observed that around 185 and 330°C there are local maximums in the DTG curves, which indicates that at this temperature most of the functional groups susceptible to

be eliminated at these temperatures, will be liberated. For this reason, these temperatures were selected to design the thermal reduction treatment.

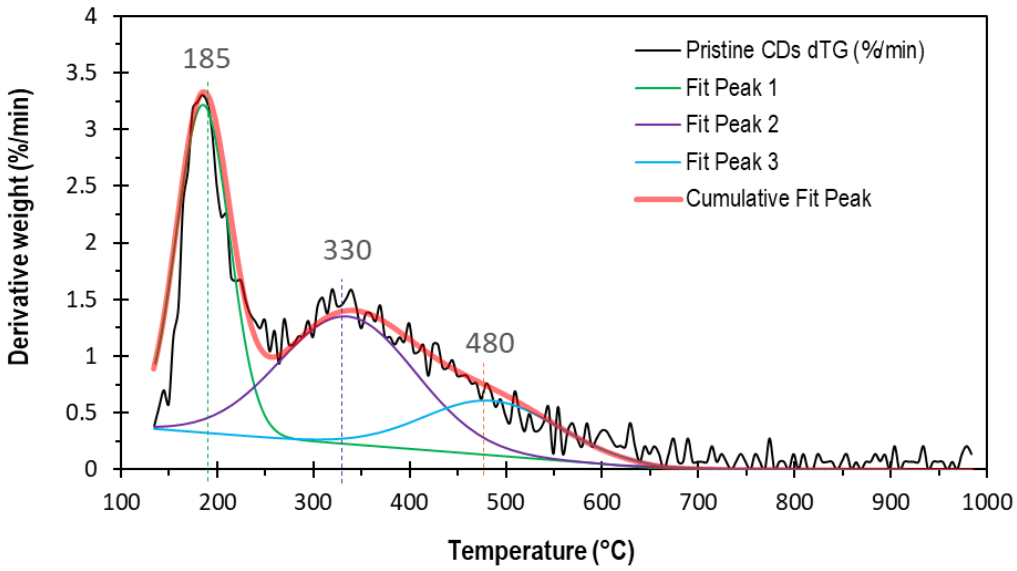

Figure 47. TG-DTG thermal curves of the pristine material (CDs-5kDa)

1.2. Thermal reduction of CDs

The pristine material underwent thermal treatment processes under an inert atmosphere at 185 and 330 °C. The reduced-CDs (CDs-185 and CDs-330, respectively) were analyzed by TGA and TPD-MS to corroborate the remotion of oxygenated groups. The thermal treatment was realized at long time of heating to ensure that all the groups susceptible to decomposition at these temperatures will be liberated. The reduction of the material was corroborated through TGA.

From the thermograms showed at Figure 48, the mass loss at 25-100 °C was attributed to the evaporation of water. The pristine material shows a mass loss of

59% at 100-900 °C, whereas the reduced CDs show a mass loss of 48% for the sample CDs-185 and 26% for the sample CDs-330. These values are consistent with the mass lost during the thermal reduction treatment. The DTG curves clearly show the effectiveness of the thermal treatment to remove certain functional groups.

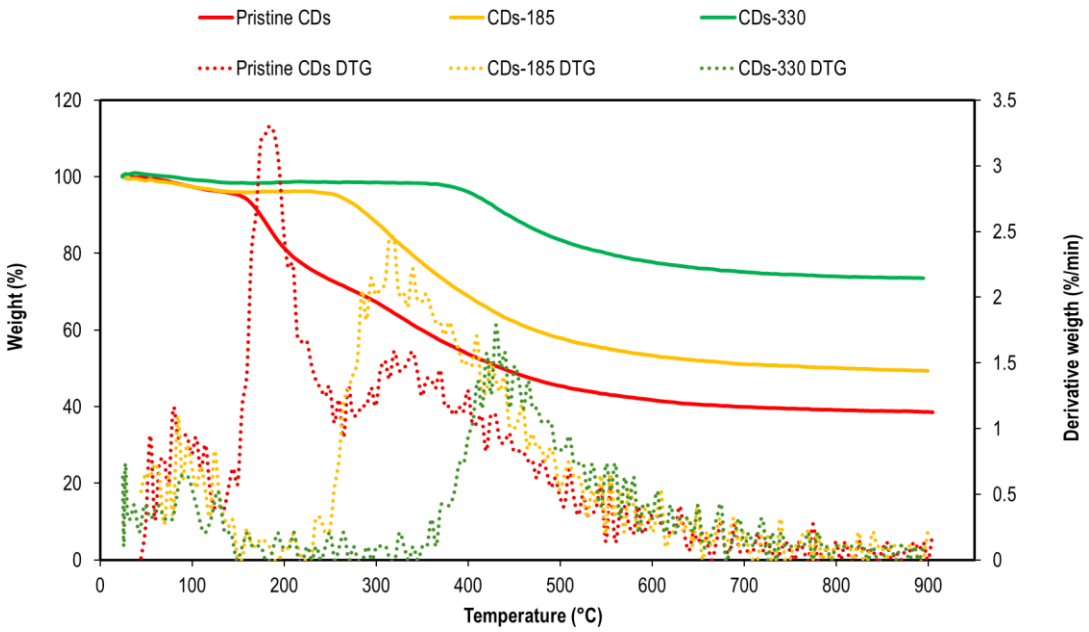

Figure 48. TG-DTG thermal curves of the prístine material (red line) and the the material after the thermal reduction (yellow and green line)

Figure 49 shows the decreasing of the amount of CO and CO_2 liberated by the reduced-CDs samples, which indicates a decreasing in the amount of oxygenated functional groups in the samples.

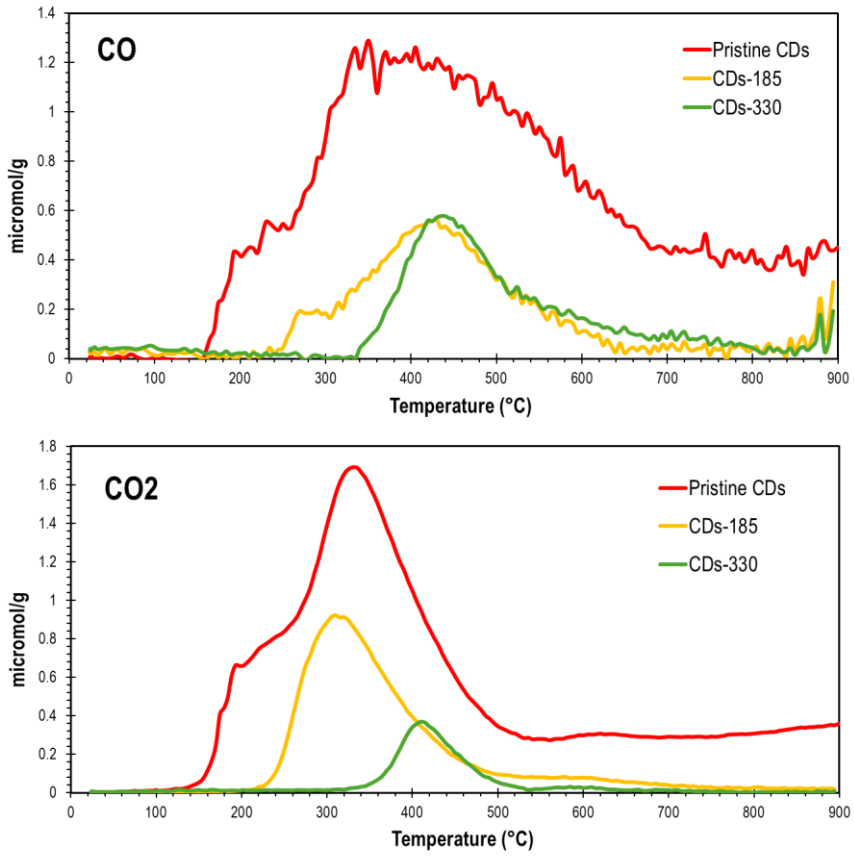

Figure 49. CO an CO_2 profiles of the pristine (red line) and reduced-CDs (yellow and green line)

1.3. UV-vis and photoluminescence spectroscopy

The powders of pristine and reduced CDs were resuspended in deionized water at a concentration of 0.5 mg/mL. The suspensions were sonicated to achieve the dispersibility of the pristine and reduced CDs. It is worth to mention that the reduced CDs samples show less capacity to be suspended in water in comparison with the pristine material. The as-obtained suspensions were diluted to obtain 0.25 and 0.125

mg/mL suspensions. The suspensions were analyzed by UV-Vis and photoluminescence spectroscopy.

As can be seen at Figure 50, the reduction treatment causes a decrease in the absorbance at 280 nm but an increase in the visible region, above 360 nm. As well, the reduced samples showed a concentration-dependent absorbance at the wavelength of 380 nm, as was observed for the pristine material in the Figure 51.

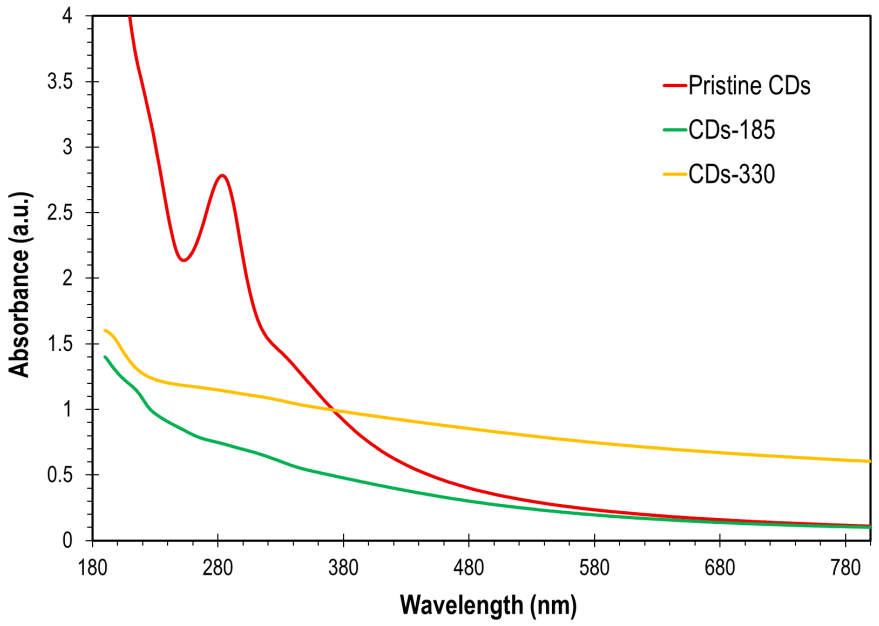

Figure 50. UV-vis spectra of 0.25 mg/mL aqueous suspensions of pristine and reduced-CDs.

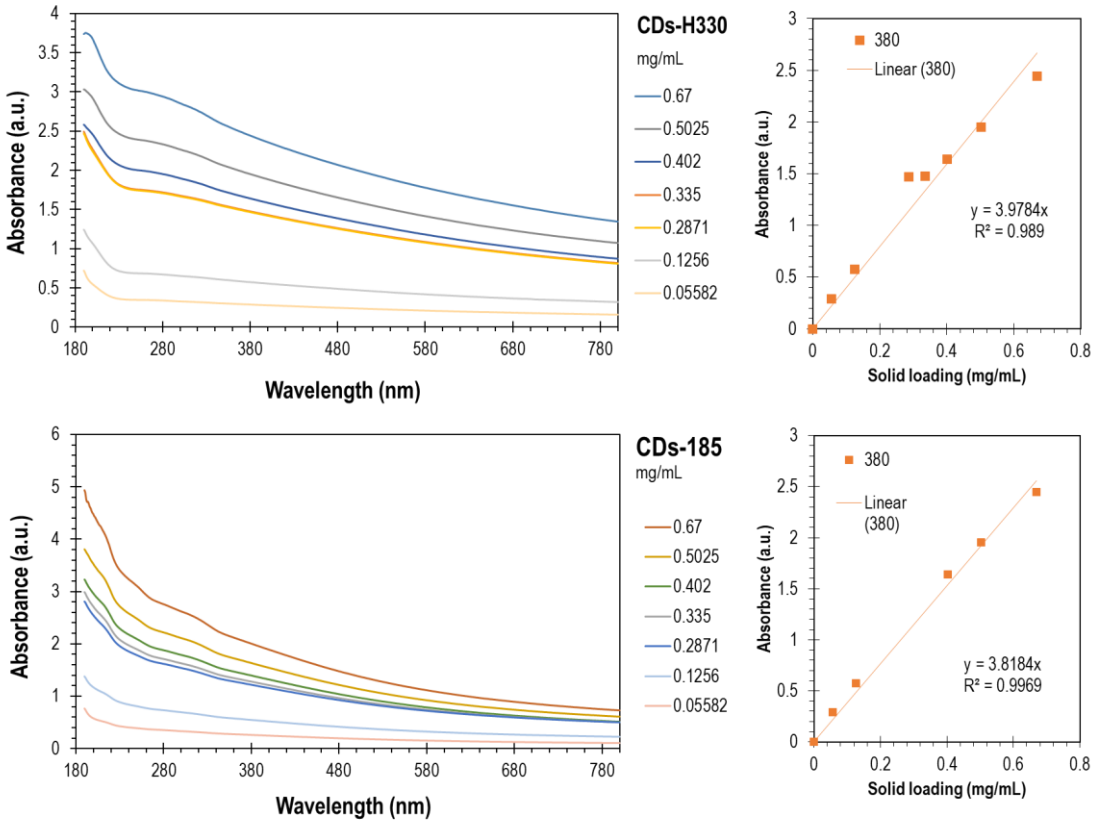

Figure 51. UV-vis spectra of suspensions of reduced-CDs at different concentrations and relation between the absorbance at 380 nm and the solid loading of the suspensions

Figure 52 shows the photoluminescence spectra of pristine and reduced CDs with an excitation laser of 375 nm at different concentrations. All the samples showed photoluminescence emission. In the case of the pristine CDs, the 0.25 mg/mL suspension shows higher emission intensity in comparison with the 1 mg/mL suspension. This is attributed to an increase in the proximity of the particles and re-absorption of light processes caused by the increase in the concentration of the suspension, as was discussed in the Chapter 3 of this document. In contrast, the reduced CDs, a lower emission intensity is observed in 0.25 mg/mL suspensions compared to 1 mg/mL suspension. This effect is attributed to the surface chemistry

of the reduced material. With fewer oxygenated groups, particle agglomeration is minimized, preventing the re-absorption processes observed in pristine particles.

It should be noted that at wavelengths close to the excitation wavelength, around 375 nm, the 1 mg/mL CDs-330 suspension shows the highest emission in comparison with the samples pristine and CDs-185. As the emission response at 375 nm is very close to the excitation laser of the spectra showed in Figure 52, measurements were performed in wavelength ranges below 375 nm and using different wavelengths excitation sources with the aim of observe better the emission response. These experiments prove the presence of emission of the nanoparticles which appear close to 375 nm.

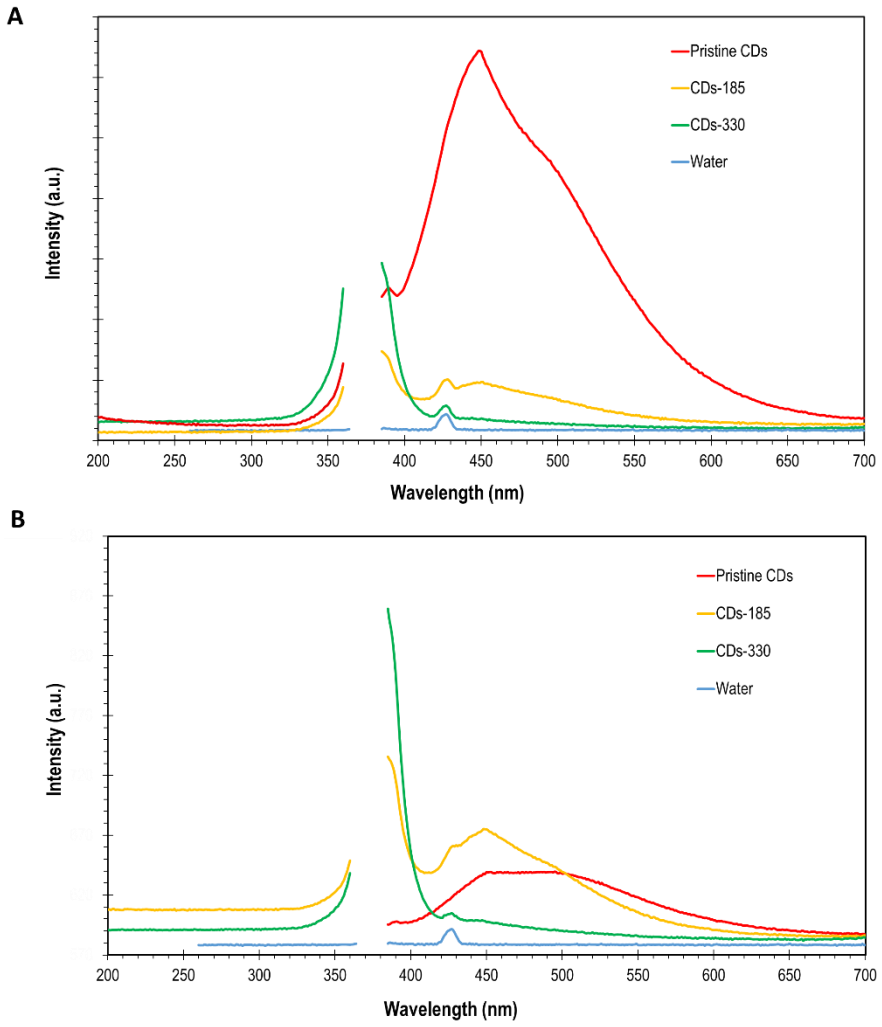

Figure 52. Photoluminescence spectra of (A) 0.25 mg/mL and (B) 1 mg/mL suspensions of pristine and reduced CDs under and excitation light of 375 nm.

1.4. Photoelectrochemistry measurements

The pristine and reduced CDs were deposited by dropping aqueous suspensions with material onto ITO-TiO_2 electrodes. Afterwards the electrodes were evaluated by photoelectrochemical techniques. Photoelectrochemical characterization of the CDs was performed in a conventional three-electrode cell configuration using ITO-TiO_2

as working electrode, graphite as counter electrode and a Standard Calomel Electrode as reference electrode. The electrolyte employed for the experiments was 0.5 M Na_2SO_4 aqueous solution without pH adjustment. The working electrode was stabilized overnight before making the electrochemical measurements.

With the aim of obtaining comparable results, the set of experiments with different solid loadings of each material (Pristine CDs, CDs-185 and CDs-330) were conducted using the same ITO-TiO_2 electrode. Each electrode was measured without and with material. The CDs suspensions were systematically added on the electroactive surface. This ensured the same amount of TiO_2 with the same structural composition on the electrode, enabling a comparison of the performance of the same electrode with and without CDs. The electrodes were evaluated with the techniques listed in the Table 17.

Table 17. Photoelectrochemical evaluation treatment

Technique	Conditions	Illumination	Time	Number of cycles
OCP	Open circuit	Dark	2 minutes	1 (dark/light/dark)
		Solar simulator light	2 minutes	
		dark	2 minutes	
CV	50 mV/s	dark	--	4
CV	50 mV/s	Solar simulator light	--	4
CV	50 mV/s	dark	--	4
CA	0.6 V	dark	2 minutes	~ 10 (dark/light/dark)
		Solar simulator light	2 minutes	
		dark	2 minutes	
CV	50 mV/s	dark	--	4

Figure 53 shows the responses of the photoelectrochemical characterization for the pristine electrode. According to these results, the potential of 0.6 V was selected to perform further chronoamperometry experiments for electrodes impregnated with CDs. This potential showed a plane response at dark conditions. These experiments have the objective to evaluate the photocurrent generation of the electrode.

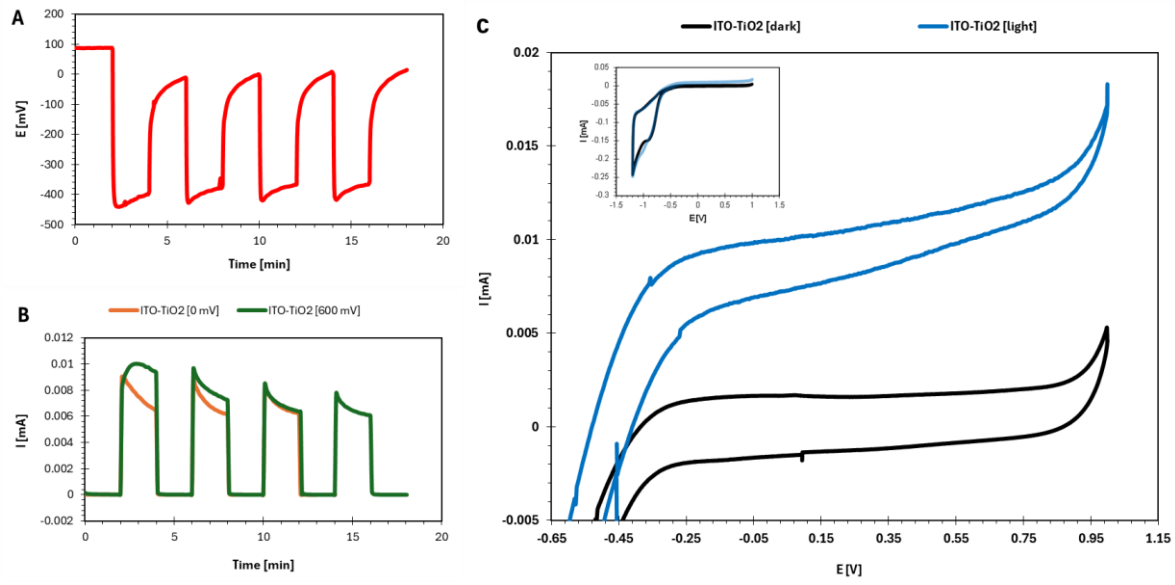

Figure 53. (A) Open circuit potential (Voc) and (B) Chronoamperometric response of the film electrodes upon on/off illumination cycles. (C) Cyclic voltammetry under dark and solar simulator light of TiO_2

Chronoamperometry experiments conducted on ITO–TiO_2 electrodes impregnated with CDs, under both illuminated and dark conditions, revealed variations in photocurrent generation compared to pristine ITO–TiO_2 electrodes. These variations, either enhancement or suppression, depended on the degree of reduction and the amount of material deposited on the electrode (Figure 54). In each case, a total of ten cycles were carried out to achieve system stabilization.

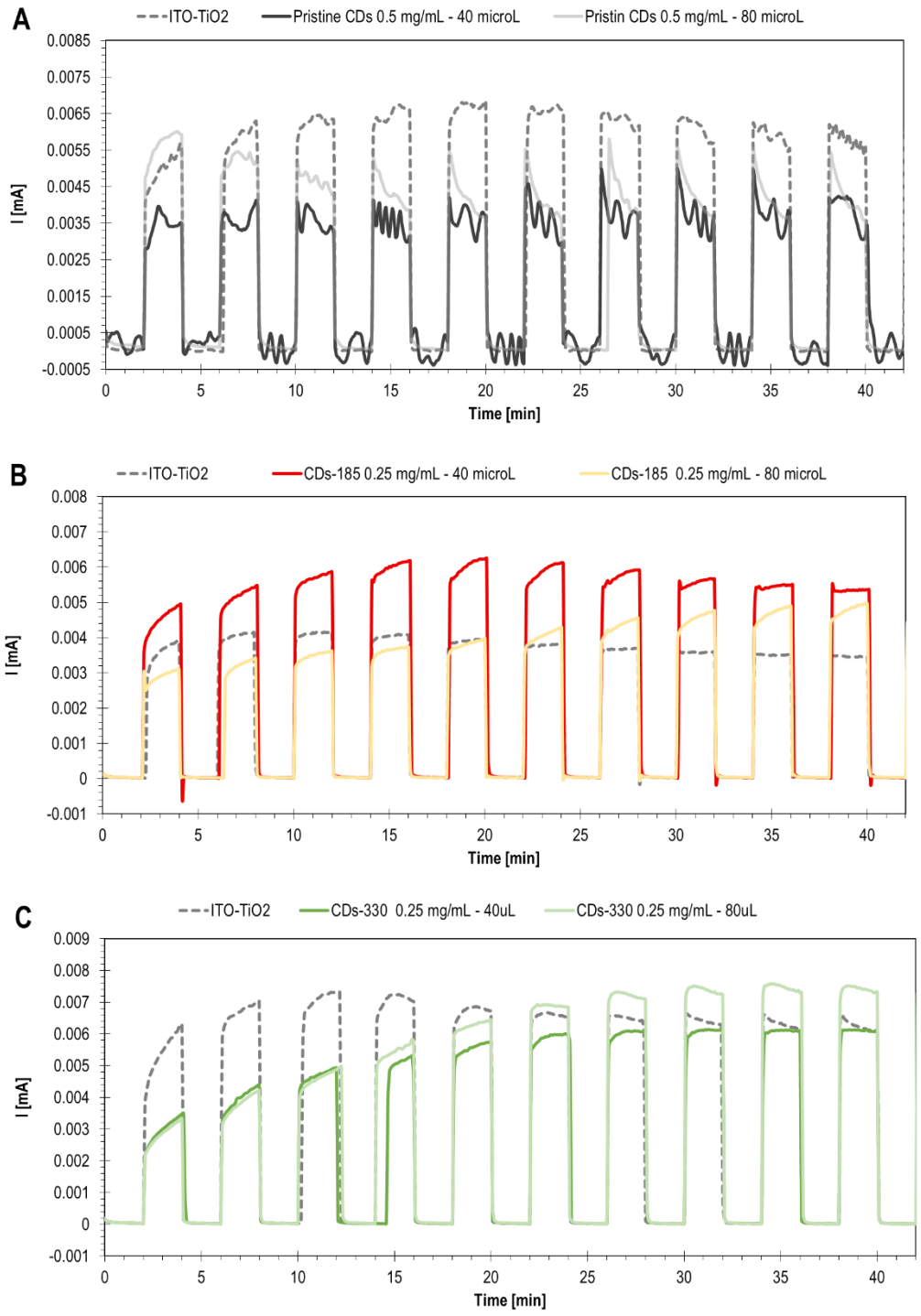

Figure 54. Chronoamperometric response at 0.6 V of the pristine ITO–TiO_2 electrode (dotted gray line) and electrodes sensitized with CDs suspensions under alternating dark and simulated solar light conditions. (A) Electrode sensitized with 0.5 mg/mL pristine CDs; (B) with 0.25 mg/mL CDs-185; and (C) with 0.25 mg/mL CDs-330

It is noteworthy that the reduced carbon dot material, CDs-185, enhanced the photocurrent generation capacity of the electrode. Specifically, the addition of 40 µL of a 0.25 mg/mL CDs-185 suspension led to an increase in photocurrent of up to 58% compared to the pristine ITO–TiO_2 electrode (Figure 55). This improvement correlates with the enhanced light absorbance of the reduced CDs in the visible region of the electromagnetic spectrum.

Electrodes sensitized with 80 and 160 µL of the 0.25 mg/mL CDs-185 suspension exhibited a suppression in photocurrent generation during the first five cycles. However, after this initial phase, their performance gradually improved, surpassing that of the pristine ITO–TiO_2 electrode. By the tenth cycle, the electrodes demonstrated photocurrent increases of 38% and 55%, respectively, compared to the pristine reference.

In contrast, electrodes sensitized with pristine CDs and reduced CDs-330 suspensions predominantly exhibited a suppression in photocurrent generation. In these cases, the maximum increases in photocurrent were limited to 7% and 20%, observed at the tenth cycle for the electrodes sensitized with 40 µL of a 0.5 mg/mL pristine CD suspension and 80 µL of a 0.25 mg/mL CDs-330 suspension, respectively (Figure 55).

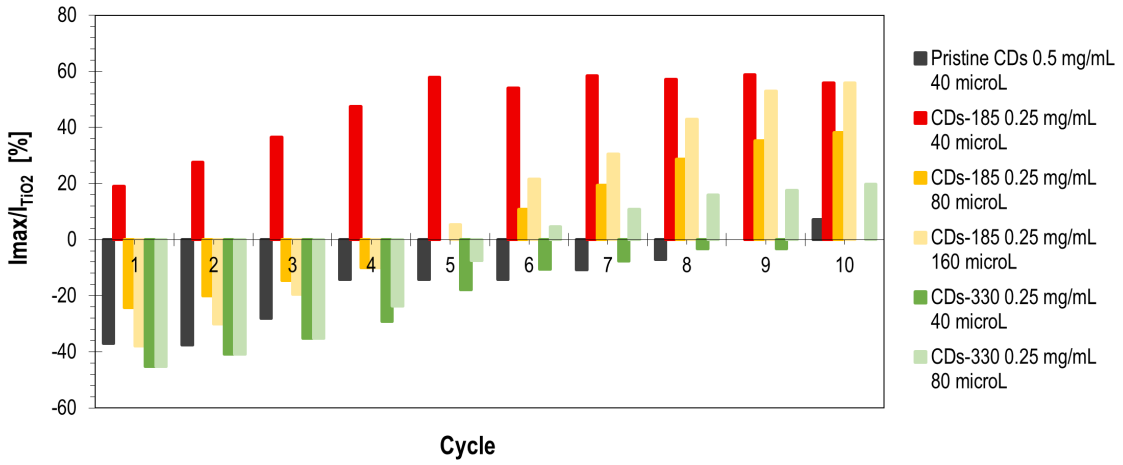

Figure 55. Photocurrent response of electrodes sensitized with pristine and reduced CDs under light/dark cycles. Values are normalized to the photocurrent of the corresponding pristine electrode ITO–TiO_2.

1.5. Conclusions

TGA and TPD-MS analyses confirmed the partial removal of oxygenated functional groups from the carbon dots (CDs) derived from orange peel. Photoluminescence measurements of the reduced CD samples revealed a notable decrease in emission around 450 nm, indicating that the main emissive groups at this wavelength were eliminated during the thermal treatments. Additionally, photoelectrochemical measurements provided insight into changes in conductivity and photoactivity induced by the deposition of pristine and reduced CDs onto ITO–TiO_2 electrodes. Among all samples, electrodes sensitized with the reduced CDs, CDs-185, exhibited the highest performance, with a photocurrent generation increase of up to 58% compared to the pristine ITO–TiO_2 electrode.